

# **Applications of** <sup>1</sup>**Positron Depth Profiling**

INIS-mf--15146

**Rudi Hakvoort**

27 MAR 1986



# **Applications of Positron Depth Profiling**

NEXT PAGE(S) left BLANK.



\*DE008355324\*



KS001970009

I: FI

DE008355324

# Applications of Positron Depth Profiling

(TOEPASSINGEN VAN POSITRON DIEPTE-PROFILERING)

**R.A. Hakvoort**



INTERFACULTAIR REACTOR INSTITUUT  
TECHNISCHE UNIVERSITEIT DELFT  
DECEMBER 1993

CIP-GEGEVENS KONINKLIJKE BIBLIOTHEEK, DEN HAAG

Hakvoort, Rudi Albert

Applications of Positron Depth Profiling / R.A. Hakvoort

Delft: Interfacultair Reactor Instituut, Technische Universiteit  
Delft – Ill.

Proefschrift Technische Universiteit Delft – Met lit. opg. –  
Met samenvatting in het Nederlands.

ISBN 90-73861-15-2

NUGI 812

Trefw.: positronen/materiaalonderzoek; edelgassen; silicium.

© 1993 R.A. Hakvoort

# Applications of Positron Depth Profiling

PROEFSCHRIFT

TER VERKRIJGING VAN DE GRAAD VAN  
DOCTOR AAN DE TECHNISCHE UNIVERSI-  
TEIT DELFT, OP GEZAG VAN DE RECTOR  
MAGNIFICUS PROF. IR. K.F. WAKKER, IN  
HET OPENBAAR TE VERDEDIGEN TEN  
OVERSTAAN VAN EEN COMMISSIE AANGE-  
WEZEN DOOR HET COLLEGE VAN DEKANEN  
OP 23 DECEMBER 1993 TE 14.00 UUR

door

RUDI ALBERT HAKVOORT

geboren te Delft,  
natuurkundig ingenieur

Dit proefschrift is goedgekeurd door de promotoren  
prof. dr A. van Veen en prof. dr ir H. van Dam.

*aan Anja,  
aan mijn ouders.*



The research described in this thesis has been carried out at the Reactor Physics Department of the Interfaculty Reactor Institute, Delft University of Technology, Mekelweg 15, NL-2629 JB Delft, The Netherlands.

NEXT PAGE(S) left BLANK.

# Table of contents

<b>Table of contents</b>	<b>9</b>
<b>List of symbols</b>	<b>15</b>
<b>1. Introduction</b>	<b>21</b>
1.1 General . . . . .	21
1.2 Positrons . . . . .	23
1.2.1 History . . . . .	23
1.2.2 Annihilation of positrons . . . . .	24
1.2.3 Positronium formation and annihilation . . . . .	27
<b>2. Principles of positron depth-profiling</b>	<b>29</b>
2.1 Introduction . . . . .	29
2.2 Interaction of positrons with solids . . . . .	30
2.2.1 Introduction . . . . .	30
2.2.2 Stopping . . . . .	32
2.2.3 Diffusion and trapping . . . . .	35
2.2.4 Surface and interface processes . . . . .	38
2.2.5 Annihilation . . . . .	40
2.2.6 Epithermal positrons . . . . .	45
2.3 Positron beam experiments . . . . .	46
<b>3. The positron beam and auxiliary techniques</b>	<b>51</b>
3.1 Introduction . . . . .	51
3.2 The Delft Variable Energy Positron Beam . . . . .	52
3.2.1 Design of the VEP . . . . .	52
3.2.2 The sample holder . . . . .	54
3.2.3 The ion source . . . . .	57
3.2.4 The photon-detection system . . . . .	58
3.2.5 Beam performance . . . . .	59

3.3	Complementary techniques . . . . .	63
3.3.1	Free Carrier Lifetime Measurements . . . . .	63
3.3.2	Raman spectroscopy . . . . .	64
3.3.3	Small Angle X-ray Scattering . . . . .	65
3.3.4	Nuclear Reaction Analysis . . . . .	67
<b>4.</b>	<b>Neon-implanted and laser-irradiated steel</b>	<b>69</b>
4.1	Introduction . . . . .	69
4.2	Sample preparation . . . . .	71
4.3	Channelling . . . . .	74
4.4	Results . . . . .	75
4.5	Discussion . . . . .	80
4.5.1	Interpretation of the data . . . . .	80
4.5.2	Estimates for the defect concentrations . . . . .	83
4.6	Conclusions . . . . .	87
<b>5.</b>	<b>Helium and hydrogen-implanted silicon</b>	<b>89</b>
5.1	Introduction . . . . .	89
5.2	Sample preparation . . . . .	90
5.3	Results . . . . .	93
5.4	Discussion . . . . .	95
5.4.1	Low-dose helium implantation . . . . .	95
5.4.2	High-dose helium implantation . . . . .	97
5.4.3	Helium refilling of the voids . . . . .	99
5.4.4	Hydrogen refilling of the voids . . . . .	101
5.5	Conclusions . . . . .	104
<b>6.</b>	<b>Ion-beam amorphized silicon</b>	<b>107</b>
6.1	Introduction . . . . .	107
6.2	Sample preparation . . . . .	109
6.3	Results . . . . .	111
6.3.1	Ion-implantation amorphized silicon and thermal annealing . . . . .	111
6.3.2	Hydrogen implantation and annealing . . . . .	112
6.3.3	Radiation damage in crystalline silicon and annealed amorphous silicon . . . . .	114
6.3.4	Carrier-lifetime measurements . . . . .	118
6.4	Discussion . . . . .	120
6.4.1	Positron trapping at defects – qualitative . . . . .	120

---

6.4.2	Positron trapping at defects – quantitative . . . .	122
6.4.3	Structural and electrical defects . . . . .	123
6.5	Conclusions . . . . .	124
<b>7.</b>	<b>Amorphous silicon</b>	<b>127</b>
7.1	Introduction . . . . .	127
7.2	Sample preparation . . . . .	129
7.3	Results . . . . .	132
7.3.1	Krypton-sputtered and MBE-system grown amorphous silicon . . . . .	132
7.3.2	Hydrogenated amorphous silicon . . . . .	135
7.4	Discussion . . . . .	139
7.4.1	Krypton-sputtered amorphous silicon . . . . .	139
7.4.2	MBE-system grown amorphous silicon . . . . .	141
7.4.3	Hydrogenated amorphous silicon . . . . .	142
7.4.4	A simple model for positronium in empty and gas-filled cavities . . . . .	148
7.5	Conclusions . . . . .	151
<b>8.</b>	<b>Epitaxial cobalt disilicide on silicon</b>	<b>153</b>
8.1	Introduction . . . . .	153
8.2	Sample preparation . . . . .	155
8.3	Results . . . . .	156
8.4	Discussion . . . . .	158
8.5	Conclusions . . . . .	160
<b>9.</b>	<b>Chemical-vapour deposited silicon-nitride films</b>	<b>161</b>
9.1	Introduction . . . . .	161
9.2	Sample preparation . . . . .	162
9.3	Results . . . . .	163
9.4	Discussion . . . . .	164
9.5	Conclusions . . . . .	166
	<b>Summary</b>	<b>167</b>
	<b>Samenvatting</b>	<b>169</b>
	<b>Bibliography</b>	<b>171</b>
	<b>Acknowledgements</b>	<b>187</b>
	<b>Curriculum vitae</b>	<b>191</b>

**List of publications related to this thesis:***Chapter 4:*

R.A. Hakvoort, A. van Veen, J. Noordhuis, and J.Th.M. de Hosson, *Defect Profiling of Neon-implanted and Laser-melted Steel by Positron Annihilation*, to be published in: *Proc. 8th Int. Conf. on Surface Modification of Metals by Ion Beams*, September 13–17, 1993, Kanazawa, Japan.

*Chapter 6:*

S. Roorda, P.A. Stolk, R.A. Hakvoort, and A. van Veen, *Vacancy-type and electrical Defects in Amorphous Si probed by Positrons and Electrons*, *Mater. Res. Soc. Symp. Proc.*, **235**, 1992, 39.

S. Roorda, R.A. Hakvoort, A. van Veen, P.A. Stolk, and F.W. Saris, *Structural and Electrical Defects in Amorphous Silicon probed by Positrons and Electrons*, *J. Appl. Phys.*, **72**, 1992, 5145.

*Chapter 7:*

R.A. Hakvoort, S. Roorda, A. van Veen, M.J. van den Boogaard, F.J.M. Buters, and H. Schut, *Positron Beam Analysis of Amorphous Silicon*, *Mater. Sci. Forum*, **105–110**, 1992, 1391.

R.A. Hakvoort, A. van Veen, H. Schut, M.J. van den Boogaard, A.J.M. Berntsen, S. Roorda, P.A. Stolk, and A.H. Reader, *Characterization of Amorphous Silicon*, to be published in: *Proc. SLOPOS5*, August 6–10, 1992, Jackson WY.

M.J. van den Boogaard, S.J. Jones, Y. Chen, D.L. Williamson, R.A. Hakvoort, A. van Veen, A.C. van der Steege, W.M. Arnold Bik, W.G.J.H.M. van Sark, and W.F. van der Weg, *The Influence of the Void Structure on Deuterium Diffusion in  $\alpha$ -Si:H*, *Mater. Res. Soc. Symp. Proc.*, **258**, 1992, 407.

M.J.W. Greuter, L. Niesen, R.A. Hakvoort, J. de Roode, A. van Veen, A.J.M. Berntsen, and W.G. Sloof, *Krypton Incorporation in Sputtered Silicon Films*, to be published in: *Proc. 9th Int. Conf. on Hyperfine Interactions*, August 17–21, 1992, Osaka, Japan.

*Chapter 8:*

F. La Via, C. Spinella, A.H. Reader, J.P.W.B. Duchateau, R.A. Hakvoort, and A. van Veen, *Defects in Epitaxial CoSi<sub>2</sub> on Si(001)*, to be published in: *J. Vac. Sci. Technol. B*.

F. La Via, C. Spinella, A.H. Reader, J.P.W.B. Duchateau, R.A. Hakvoort, and A. van Veen, *Formation and Characterization of Epitaxial CoSi<sub>2</sub> on Si(001)*, to be published in: *Appl. Surf. Sci.*.

*Chapter 9:*

R.A. Hakvoort, H. Schut, A. van Veen, W.M. Arnold Bik, and F.H. P.M. Habraken, *Positron Annihilation Study of Low-Pressure Chemical-Vapour Deposited Silicon-Nitride Films*, *Appl. Phys. Lett.*, **59**, 1991, 1687.

*Other publications:*

A. van Veen, H. Schut, J. de Vries, R.A. Hakvoort, and M.R. Ijpma, *Analysis of Positron Profiling Data by means of "VEPFIT"*, in: P.J. Schultz, G.R. Massoumi, and P.J. Simpson, *Positron Beams for Solids and Surfaces*, *AIP Conference Proc.*, **218**, AIP, New York, 1990.

H. Schut, A. van Veen, R.A. Hakvoort, M.J.W. Greuter, and L. Niesen, *The Effect of Channelling on the Defect Depth Distribution in 110 keV Rb-Implanted poly-W*, to be published in: *Proc. SLOPOS5*, August 6–10, 1992, Jackson WY.

NEXT PAGE(S) left BLANK.

# List of symbols

$a$	Firsov screening length [nm]
$b$	magnitude of the Burgers vector [nm]
$\vec{B}$	magnetic field (section 3.2.1) [T]
$c$	velocity of light [ $2.9979 \times 10^8$ m/s]
$c(E)$	measured detector signal [-]
$c(l)$	steady-state positron distribution as a function of depth [ $\text{cm}^{-3}$ ]
$c_t$	longitudinal sound velocity in matter [m/s]
$C(\omega)$	Fourier transform of $c(E)$ [-]
$d$	atomic spacing along the lattice row [nm]
$D$	surface dipole barrier [eV]
$D$	particle size (section 4.2) [nm]
$D_+$	positron diffusivity in defect-free material [ $\text{m}^2/\text{s}$ ]
$e$	elementary charge [ $1.6022 \times 10^{-19}$ C]
$E$	(initial) energy of implanted positron [keV]
$E$	photon energy (section 2.2.5) [eV]
$E$	initial energy of implanted ion (section 4.3) [MeV]
$\mathcal{E}$	electric field [V/cm]
$\vec{E}$	electric field (section 3.2.1) [V/cm]
$E_n$	energy of particle in state $n$ [eV]
$E_{Ps}$	positronium binding energy in vacuum [eV]
$E'_{Ps}$	positronium binding energy in a material [eV]
$f_b$	fraction of annihilations in defect-free material [-]
$f_{Ps}$	fraction of annihilations from a positronium bound state [-]
$f_s$	fraction of annihilations from a surface state [-]
$f_{t,i}$	fraction of annihilations from a trapped state localized

	at a defect of type $i$ [-]
$\hbar$	scattering vector [ $\text{nm}^{-1}$ ]
$h$	absolute value of $\hbar$ [ $\text{nm}^{-1}$ ]
$h$	Planck's constant divided by $2\pi$ [ $1.0546 \times 10^{-34}$ Js]
$I(E, z)$	implantation rate of positrons that are thermalized at depth $z$ [ $\text{cm}^{-3}\text{s}^{-1}$ ]
$j(h)$	scattering function of a single particle [-]
$J(h)$	normalized intensity of scattered radiation [-]
$k_B$	Boltzmann's constant [ $1.3807 \times 10^{-23}$ J/K]
$K$	constant [-]
$\ell$	quantum number (section 7.4.4) [-]
$L_i$	positron diffusion length in layer $i$ [nm]
$L_+$	positron diffusion length in defect-free material [nm]
$L_{+,eff}$	effective positron diffusion length in materials with a uniform defect distribution [nm]
$m$	shape parameter of a Makhovian profile [-]
$m$	mass of particle (section 7.4.4) [kg]
$m_e$	rest mass of the electron [ $9.1095 \times 10^{-31}$ kg]
$m_p$	effective mass of positron [kg]
$M$	ion mass [kg]
$n$	constant [-]
$n$	quantum number (section 7.4.4) [-]
$n(E)$	noise component of measured detector signal [-]
$n_e$	electron density in medium [ $\text{cm}^{-3}$ ]
$n_i$	defect concentration [ $\text{cm}^{-3}$ ]
$N$	total number of counts accumulated in the 511 keV peak (section 3.2.1) [-]
$N$	planar atomic density (section 4.3) [ $\text{nm}^{-2}$ ]
$N(\omega)$	Fourier transform of $n(E)$ [-]
$N_i$	volume density of defects of type $i$ [ $\text{cm}^{-3}$ ]
$\mathbf{p}$	total momentum of annihilating particles [ $\text{kg m/s}$ ]
$p$	absolute value of $\mathbf{p}$ [ $\text{kg m/s}$ ]
$p_l$	longitudinal component of $\mathbf{p}$ [ $\text{kg m/s}$ ]
$p_t$	transverse component of $\mathbf{p}$ [ $\text{kg m/s}$ ]
$P$	number of counts accumulated in the 511 keV peak region (section 2.3) [-]

---

$P$	hydrostatic pressure (section 7.4.4) [Pa]
$P_{eq}$	equilibrium pressure (section 7.4.4) [Pa]
$P(E, z)$	positron implantation profile [-]
$P_0$	$P$ for 0 % positronium formation [-]
$P_1$	$P$ for 100 % positronium formation [-]
$q$	wavevector [ $\text{m}^{-1}$ ]
$r$	void radius [nm]
$r(E)$	response function of the photon-detection system [-]
$r'_{Ps}$	interaction radius of a positronium atom with the wall of the cavity [nm]
$r_0$	classical radius of the electron or positron [nm]
$R$	ratio of counts accumulated in different regions of a positron-annihilation spectrum (section 2.3) [-]
$R$	radius of a sphere (section 3.3.3) [m]
$R(\omega)$	Fourier transform of $r(E)$ [-]
$R_g$	radius of gyration of a scattering particle [m]
$R_0$	$R$ for 0 % positronium formation [-]
$R_1$	$R$ for 100 % positronium formation [-]
$s(E)$	smeared-out detector response signal of photon distribution [-]
$S$	$S$ -parameter [-]
$\mathcal{S}$	normalized $S$ -parameter [-]
$S(\omega)$	Fourier transform of $s(E)$ [-]
$S_b$	$S$ -parameter related to annihilations in defect-free material [-]
$S_i$	$S$ -parameter related to layer $i$ [-]
$S_{Ps}$	$S$ -parameter related to annihilations from a positronium bound state [-]
$S_s$	$S$ -parameter related to annihilations from a surface state [-]
$S_{t,i}$	$S$ -parameter related to annihilations from a trapped state localized at a defect of type $i$ [-]
$T$	temperature [K]
$T'$	number of counts accumulated in the photon-energy region below 511 keV (section 2.3) [-]
$T'_s$	substrate temperature during deposition [K]

$T_0$	critical temperature above which positron-phonon scattering is elastic [K]
$u(E)$	uncorrupted photon-energy distribution [-]
$\tilde{u}(E)$	estimated signal for $u(E)$ [-]
$U(\omega)$	Fourier transform of $u(E)$ [-]
$\tilde{U}(\omega)$	Fourier transform of $\tilde{u}(E)$ [-]
$v$	average carrier velocity [m/s]
$v_d$	positron drift velocity due to electric field [m/s]
$v_e$	velocity of electron [m/s]
$v_f$	void fraction [-]
$V_p$	volume of scattering particle [nm <sup>3</sup> ]
$V_{p_s}$	volume of positronium atom (section 7.4.4) [nm <sup>3</sup> ]
$V_0$	depth of potential well [eV]
$x$	integration parameter [m]
$z$	depth below surface [nm]
$\bar{z}$	mean positron implantation depth [nm]
$z_0$	penetration parameter [nm]
$Z$	atomic number of material [-]
$Z_1$	nuclear charge of the channelling ion [-]
$Z_2$	nuclear charge of the target ion [-]
$\alpha$	fine-structure constant (section 1.2.2) [-]
$\alpha$	constant (chapter 2) [g.cm <sup>-2</sup> .(keV) <sup>-n</sup> ]
$\beta$	constant [-]
$\gamma$	surface tension [N m <sup>-1</sup> ]
$\gamma(n)$	enhancement factor accounting for electron-positron correlations [-]
$\Gamma$	width of the transverse-optic peak of a one-phonon Raman scattering process [cm <sup>-1</sup> ]
$\Gamma(x)$	Euler gamma function [-]
$\Delta E$	photon energy shift (Doppler shift) [eV]
$\Delta E$	energy difference between two levels (section 7.4.4) [eV]
$\Delta E_+$	potential step at interface for a positron [eV]
$\Delta M$	mass difference between two ions [kg]
$\Delta\theta_b$	rms bond-angle deviation [rad]
$\Delta\rho$	electron-density difference between voids and the

	surrounding material [ $\text{cm}^{-3}$ ]
$\epsilon$	integration parameter (section 2.2.5) [-]
$\epsilon$	microstrain (section 4.2) [-]
$\epsilon_d$	deformation potential constant for positrons [-]
$\eta$	substitution parameter (section 7.4.4) [-]
$\theta$	scattering angle [rad]
$\kappa_t$	positron trapping rate into defects [ $\text{cm}^{-3}\text{s}^{-1}$ ]
$\kappa_{t,i}$	positron trapping rate into defects of type $i$ [ $\text{cm}^{-3}\text{s}^{-1}$ ]
$\lambda$	positron annihilation rate [ $\text{s}^{-1}$ ]
$\lambda$	X-ray wavelength (section 3.3.3) [nm]
$\lambda_b$	positron annihilation rate in defect-free material [ $\text{s}^{-1}$ ]
$\lambda_{th}$	De Broglie wavelength of a thermalized free positron [nm]
$\lambda_{2\gamma}$	$2\gamma$ annihilation rate [ $\text{s}^{-1}$ ]
$\mu$	positron mobility [ $\text{cm}^2/\text{Vs}$ ]
$\mu_m$	mass absorption coefficient [ $\text{cm}^2\text{g}^{-1}$ ]
$\mu_+$	chemical potential for a positron [eV]
$\mu_-$	chemical potential for an electron [eV]
$\nu_t$	specific positron trapping rate for a defect [ $\text{s}^{-1}$ ]
$\xi$	substitution parameter (section 7.4.4) [-]
$\rho$	mass density of material [ $\text{g}/\text{cm}^3$ ]
$\rho$	dislocation density (section 4.2) [ $\text{m}^{-2}$ ]
$\bar{\rho}(\mathbf{x})$	electron density at $\mathbf{x}$ , averaged over several atoms near $\mathbf{x}$ [ $\text{cm}^{-3}$ ]
$\rho_i$	electron density in structural inhomogeneity [ $\text{cm}^{-3}$ ]
$\rho_m$	mass density of (void-free) material [ $\text{g}/\text{cm}^3$ ]
$\sigma_i$	cross section for carrier capture [ $\text{cm}^2$ ]
$\sigma_S$	statistical error in the measured $S$ -parameter [-]
$\sigma_{2\gamma}$	cross section for $2\gamma$ annihilation [ $\text{cm}^2$ ]
$\tau$	positron lifetime (chapter 1) [ps]
$\tau$	decay rate of plasma density (chapters 3 and 6) [ps]
$\tau_b$	positron lifetime in defect-free material [ps]
$\phi$	deviation from collinearity [rad]
$\phi(E)$	filter [-]
$\phi_+$	positron workfunction [eV]
$\phi_-$	electron workfunction [eV]

$\phi_{Ps}$	positronium workfunction [eV]
$\Phi(\omega)$	Fourier transform of $\phi(E)$ [-]
$\chi_+$	positron affinity [eV]
$\chi_-$	electron affinity [eV]
$\psi_{\text{axial}}$	critical angle for axial channelling [rad]
$\psi_{\text{planar}}$	critical angle for planar channelling [rad]
$\omega$	reciprocal energy (Fourier space) [eV <sup>-1</sup> ]

# Chapter 1

## Introduction

### 1.1 General

Materials research is a steady growing branch of solid-state physics. It has as its object the study of matter, principally solids, and aims at understanding the physical processes that underlie to their macroscopic characteristics and behaviour. Especially from an industrial point of view, materials research is of the utmost importance, since the design and construction of new products often requires materials of the highest quality. In many cases this means that there is a demand for detailed knowledge of, e.g., the atomic structure, defects in the crystal lattice, internal electric fields, and interface effects of the used materials. Analysis techniques that yield qualitative or quantitative information are therefore not only desirable but also necessary.

Positron physics is concerned with the interaction of low-energy positrons with matter. From the discovery of the positron sixty years ago, positron physics has developed into an important technique for providing unique information on a wide variety of problems in condensed-matter physics. The reason for this growth is that physicists have realized that the characteristics of the positron-electron annihilation process depend almost entirely on the state of the positron-electron system in the matter. The inexpensive experimental equipment for carrying out positron-lifetime measurements has also contributed extensively to the popularity of positron studies.

The positron technique has many advantages in materials research. It provides a nondestructive method because the information is carried out of the material by penetrating annihilation radiation. No special sample preparation is necessary and in some applications also *in-situ* studies, e.g., on dynamic phenomena at elevated temperatures are possible (Hautojärvi, 1979).

Especially the development of intense positron beams with variable energy has resulted in many new applications. Whereas conventional positron-annihilation studies only yield information on the bulk of the material, variable energy positron beams provide the opportunity of studying the properties of the near-surface region up to a depth of several  $\mu\text{m}$ . Sub-surface defect profiling is the fastest growing area of research with positron beams, principally since there are so many industrial applications of this sensitive positron depth-profiling technique.

The positron-annihilation experiments reported in this thesis were performed with the Delft Variable Energy Positron Beam (VEP). The VEP project was initiated in 1983 by the Radiation Damage group of the Reactor Physics department of the Interfaculty Reactor Institute (Delft, The Netherlands). At that time the group already had some expertise in positron physics, since a positron-lifetime spectrometer was already operational, while the construction of a high-resolution lifetime spectrometer was in progress. The VEP was built during the period 1984–1986. In March 1987 the positron source was installed. After a year of intensive testing, the facility was officially inaugurated in April 1988. An in-depth description of the beam in its former configuration is given by Schut (1990), of which the present thesis forms a continuation. The VEP facility has been used extensively for applied materials research. In the course of time some minor adjustments to the beamline have been made, some of which are described in this thesis.

The structure of this thesis is as follows. The present chapter gives the basics of positron physics and a concise review of experimental positron techniques. Chapter 2 proceeds with discussing the principles of positron depth profiling as applied in solid-state physics. The interaction of positrons with condensed matter (implantation, thermalization, diffusion, trapping, annihilation, etc.) is especially

described in some detail. It closes with some observations concerning positron beam experiments. In the first part of chapter 3 the Delft Variable Energy Positron Beam (VEP) is described, which was used for the experiments presented in this thesis. The emphasis lies on recent adjustments to the beam configuration, viz. the new sample holder, the ion source and the new electronics for photon detection and data processing. A few notes on the beam performance conclude this section. The second part of chapter 3 deals with some techniques commonly used in materials research that were applied for giving additional information on the samples examined. They include Free Carrier Lifetime measurements, Raman spectroscopy, Small Angle X-ray Scattering, and Nuclear Reaction Analysis.

From chapter 4 onwards positron depth-profiling experiments on specific samples are described. Chapter 4 deals with neon-implanted and laser-irradiated steel, chapter 5 with low-energy helium and hydrogen-implanted silicon, chapter 6 with ion-beam amorphized silicon, chapter 7 with other types of amorphous silicon, viz. hydrogenated silicon and silicon grown by Kr-sputtering and MBE-system deposition, chapter 8 with epitaxial cobalt disilicide on silicon, and, finally, chapter 9 with chemical-vapour deposited silicon-nitride films. Each chapter starts with a short review of current research in the respective field and closes with some conclusions.

## 1.2 Positrons

### 1.2.1 History

The positron was predicted in 1930 by Dirac as the ‘negative’ energy extension of his theory of electron energy levels (Dirac, 1930). Three years later it was discovered by Anderson (Anderson, 1932, 1933a, and 1933b). In 1951 Deutsch demonstrated the existence of positronium, the bound state of a positron with an electron (Deutsch, 1951a and 1951b).

During the fifties physicists studied the structure and properties of positrons and positronium atoms. From the early sixties they started to apply positrons for the study of condensed matter, followed in the

seventies by physical chemists who found chemical applications for positrons and positronium (Cheng *et al.*, 1989).

In the late seventies for the first time carefully prepared surfaces were used as positron moderators (Mills, 1978; Lynn, 1979), followed in the eighties by the development of slow-positron beams, i.e. beams with positrons in the keV domain. Reviews of positron physics include Hautojärvi (1979), Brandt and Dupasquier (1983), and more recently, Schultz and Lynn (1988), Seeger and Banhart (1990), and Lahtinen and Vehanen (1991).

Positrons have the same mass ( $9.1095 \times 10^{-31}$  kg) and spin ( $\frac{1}{2}$ ) as electrons, but opposite charge and magnetic moment. They are stable in vacuum (lifetime at least  $> 2 \times 10^{21}$  year; Belotti *et al.*, 1983), but rapidly thermalize and annihilate with electrons in materials, predominantly via  $2\gamma$  decay ( $\sim 511$  keV) with a mean lifetime of typically only a few hundred picoseconds.

## 1.2.2 Annihilation of positrons

### Cross section for annihilation

Annihilation is the process by which a particle and its antiparticle are transformed into photons. In dense materials the annihilation of a positron and an electron predominantly takes place via two-photon annihilation:

$$e^+(\uparrow) + e^-(\downarrow) \longrightarrow 2\gamma. \quad (1.1)$$

Energy conservation causes the energy of the  $\gamma$  photons to be  $m_e c^2$ , with  $m_e$  the rest mass of the electron and  $c$  the velocity of light ( $2.9979 \times 10^8$  m/s), i.e. 2  $\gamma$ 's of 510.99 keV.

The cross section for  $2\gamma$  annihilation  $\sigma_{2\gamma}$  of a non-relativistic free positron and electron is (Stevens, 1980):

$$\sigma_{2\gamma} = \pi r_0^2 c/v_e, \quad (1.2)$$

which is inversely proportional to the velocity of the electron ( $v_e$ ). The parameter  $r_0 = e^2/m_e c^2 = 2.8 \times 10^{-15}$  m is the classical radius of the electron or positron. The cross section for three-photon annihilation is a factor of the order of the fine-structure constant  $\alpha$  ( $\approx 1/137.036$ )

lower (Mills, 1992). Single quantum annihilation of an electron-positron pair is possible only in the presence of a third body such as a nucleus which can recoil, and has recently been observed by Palathingal *et al.* (1991).

The  $2\gamma$  cross section is found to be negligible for large  $v$  in comparison with the cross sections for ionization and excitation. In fact as long as these processes are energetically possible, they predominate over annihilation.

In a medium containing  $n_e$  electrons per  $\text{cm}^3$ , positron annihilation takes place in a first-order approximation, neglecting electron-electron interactions, with a rate:

$$\lambda_{2\gamma} = \sigma_{2\gamma} n_e v_e \gamma(n) = \pi r_0^2 c n_e \gamma(n), \quad (1.3)$$

where  $\gamma(n)$  is a so-called enhancement factor which accounts for electron-positron correlations (Boronski, 1992; Rubaszek, 1991; West, 1974).

### Non-zero momentum during annihilation

When both the positron and the electron are at rest at the moment of annihilation conservation of energy and momentum causes the two  $\gamma$  photons to be emitted collinearly in opposite directions, each with an exact energy of  $m_e c^2 = 511 \text{ keV}$ .

If the total momentum  $\mathbf{p}$  of the annihilating particles relative to the laboratory frame is non-zero, the  $\gamma$  photons are still emitted collinearly in the centre-of-mass frame of the electron-positron pair, but in the laboratory frame the  $\gamma$  momenta are no longer at a  $180^\circ$  angle if the transverse component  $\mathbf{p}_t$  of  $\mathbf{p}$  is not zero (see figure 1.1). The deviation  $\phi$  from collinearity depends on the magnitude of  $\mathbf{p}_t$ , while the size of the longitudinal component  $p_l$  determines the energy shift ('Doppler shift') of the photons. For nonrelativistic electrons ( $p \ll m_e c$ ) the photon energies observed in the laboratory frame are  $m_e c^2 - \Delta E$  and  $m_e c^2 + \Delta E$ , with

$$\Delta E = \frac{c p_l}{2}, \quad \text{and} \quad (1.4)$$

$$\phi = \frac{p_t}{m_e c}. \quad (1.5)$$

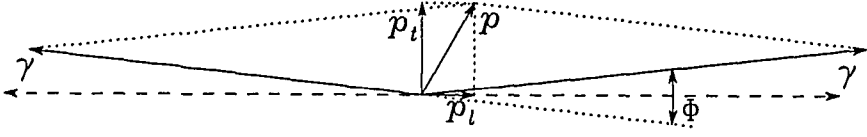


Figure 1.1: Conservation of momentum for the annihilation of an electron-positron pair with total momentum  $\mathbf{p}$ . The longitudinal and transverse component of  $\mathbf{p}$  are  $\mathbf{p}_l$  and  $\mathbf{p}_t$  respectively. The transverse component of the momentum causes a deviation  $\phi$  from exact collinearity of the two  $\gamma$ 's, whereas the longitudinal component causes small energy shifts of the photons. The magnitude of  $\mathbf{p}$  is not to scale.

A typical value of the momentum of electrons in metals based on the free electron model is  $1.5 \times 10^{-24} \text{ kg m s}^{-1}$ , which corresponds to an energy shift  $\Delta E$  of 1.4 keV. This shift lies within the detection limit of high resolution solid state detectors. The corresponding maximum angular deviation  $\phi$  is 5.6 mrad, also much higher than the resolution of current angular-correlation systems (Schut, 1990).

## Experimental techniques

Experimental techniques with positrons fall into two broad categories, depending on whether they give information on the *annihilation rate* of the positrons or on the *momentum distribution* of the annihilating positron-electron pairs.

1. *Annihilation rate*: The annihilation rate  $\lambda$  of positrons is determined by the overlap of the positron wave function with the electron wave functions and depends therefore on the electron density at the annihilation sites (compare Puska, 1991). In absence of electrons the positron is a stable particle, but in an environment of electrons the positron has a finite lifetime  $\tau$ , usually of the order of 100 ps. The positron lifetime is the inverse of the annihilation rate:

$$\tau = \lambda^{-1}. \quad (1.6)$$

Measurements of positron lifetime or distributions of lifetimes therefore give information on the sites at which positrons annihilate, which can be, e.g., in bulk material (short lifetimes) or from a localized state

due to trapping in some defect (in the case of open-volume defects this leads to longer lifetimes). Generally, the shorter a positron lifetime, the higher the electron density at the site of annihilation (see, e.g., De Vries, 1987; Schultz and Snead, 1990; Seeger and Banhart, 1990). Annihilation rates of the more common metals and semiconductors are tabulated in Seeger *et al.* (1989).

*2. Momentum distribution:* The momenta of thermalized positrons are small compared with the width of the momentum distribution of the electrons in condensed matter. Therefore, the annihilation photons carry information about the local momentum distribution of the electrons in the specimen. One can either measure the deviation  $\phi$  from collinearity and obtain information about the two transverse components of the electron momentum [see equation (1.5)] or one can determine the Doppler shift of the energies of the annihilation photons, which carries information about the longitudinal component of the electron momentum [see equation (1.4)]. The former is the basis of the so-called ACAR (Angular Correlation Angular Resolved) technique, while the latter forms the heart of Doppler-broadening experiments. Doppler-broadening experiments have been employed for the measurements described in this thesis.

Variations in both the momentum distribution of the positron-electron pairs and the annihilation rate pertain primarily to the *electrons* in the host material, which makes positrons excellent probe particles for electron behaviour in materials. On the other hand, information on *positron* behaviour has to be obtained in indirect ways, e.g., through studying diffusion and trapping characteristics.

### 1.2.3 Positronium formation and annihilation

Under some circumstances a positron can bond to an electron to form a positronium (Ps) atom with a vacuum binding energy of about 6.8 eV.

The ground states of positronium are the singlet  $^1S_0$  state (para-positronium, *p*-Ps) and the triplet  $^3S_1$  state (ortho-positronium, *o*-Ps). One quarter of the formed positronium is in the singlet state and three quarters in the triplet state. The vacuum lifetime of *p*-Ps is 125 ps, while the lifetime of *o*-Ps is 142 ns (Westbrook *et al.*, 1989).

due to its non-zero spin requiring  $3\gamma$  annihilation. In most materials with a high electron density the lifetime of *o*-Ps will be reduced to a few nanoseconds because the *o*-Ps annihilates via an electron *pickoff*-reaction, the parallel-spin electron being exchanged for an electron with anti-parallel spin, thus enabling  $2\gamma$  annihilation.

Positronium may be formed by the ionization of a valence electron by the energetic positron and subsequent bonding to this electron (*Ore mechanism*; Green and Lee, 1964; Goldanskii, 1986) or by the positron capturing a conduction electron created during slowing down (*spur mechanism*; Mogensen, 1974; Byakov *et al.*, 1974; for a comparison of these mechanisms, see Stevens, 1980, and Dupasquier, 1983). Recently, resonant positronium formation has been proposed as a third positronium-formation mechanism (Zhang and Ito, 1990). In the bulk of most materials with a high electron density, e.g., metals and semiconductors, the formation of positronium is not possible due to the size of the positronium atom (twice that of a hydrogen atom), but in molecular crystals, liquids and polymers positronium formation is possible, at least in small voids (see Eldrup, 1982 and 1983; Jean, 1990; Tao, 1972).

Nevertheless, even on the surface of metals and semiconductors (fast) positronium may be formed if the material is placed in vacuum, as in the experiments described in this thesis.

# Chapter 2

## Principles of positron depth profiling

### 2.1 Introduction

Positrons are a powerful tool for depth profiling of materials. During the last two decades positron annihilation has been developed to a technique that is able to detect small defect concentrations, especially of open-volume defects, in the surface region of a sample. Possible applications are the analysis of ion-beam modified materials, epitaxially deposited layers on semiconductors and more generally the deposition of thin films and coatings.

Electron microscopy and associated techniques still form one of the most basic tools for elemental and structural analysis. Since the seventies new techniques were developed, based on dynamic ion-solid interactions. Among these are the now full-grown Rutherford Backscattering (RBS), Nuclear Reaction Analysis (NRA) and Secondary Ion Mass Spectrometry (SIMS) techniques, which are capable of depth profiling of impurity atoms (Feldman, 1986). In general, the above techniques lack sensitivity to detection of open-volume defects. Other (nuclear) techniques but without depth sensitivity are Mössbauer spectroscopy, Perturbed Angular Correlation (PAC), Electron Spin Resonance (ESR) and Nuclear Magnetic Resonance (NMR).

Already in 1949 it was observed that the two  $\gamma$  rays arising from the annihilation of a thermalized positron with an electron were not exactly collinear (DeBenetti, 1949), which was correctly explained as an effect of the non-zero momentum of the electron. From this year on positrons were used for materials analysis, first only fast positrons, but from the mid-seventies also moderated positrons, i.e. slow positrons with kinetic energies in the keV domain. In the eighties, especially, positron annihilation has become a full-grown technique for materials research (Schultz and Lynn, 1988; Schultz and Sncad, 1990; Seeger and Banhart, 1990; Van Veen, 1990).

Positrons have a natural affinity with sites in a material where no ion cores are present and are therefore sensitive probes for open-volume defects. Apart from trapping in defects and subsequent annihilation other processes occur: trapping at surfaces, positronium formation at surfaces, positronium desorption and annihilation in the virgin material. In principle the contributions to these processes can be derived from the annihilation measurements so that not only information is obtained on the trapped probe but also on its diffusion behaviour and branching at the surface. Since the positron is a charged particle its diffusive motion will be influenced by the presence of internal electric fields, e.g., in semiconductors.

This chapter presents a brief summary of our present understanding of the interaction of positrons with solids (section 2.2), while section 2.3 shows how to extract information from positron-beam experiments.

## **2.2 Interaction of positrons with solids**

### **2.2.1 Introduction**

When energetic positrons enter a solid several processes may occur. Apart from a fraction that backscatters at the surface, the positrons undergo stopping processes related to several energy-loss mechanisms and are finally thermalized (see further section 2.2.2).

Now there are three main possibilities. Firstly, the thermalized positron may remain in a delocalized (Bloch) state and diffuse around

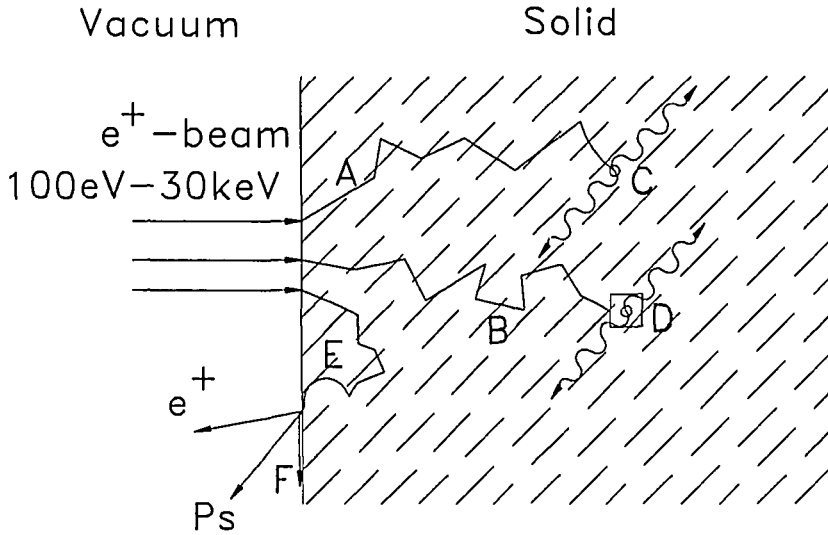


*Figure 2.1:* Possible interactions of energetic positrons entering a solid. A: stopping and thermalization of implanted positrons; B: diffusion of thermalized positrons; C: annihilation from a freely diffusing state; D: trapping in a bulk defect followed by annihilation from this state; E: back-diffusion to the vacuum-solid interface; F: trapping and annihilation in a surface-localized state. Besides free positron and positronium emission from the surface are indicated.

until it annihilates with an electron in the material due to the overlap of its wave function with an electron wave function. Secondly, the positron may trap in some defect, its wave function becoming strongly localized (see section 2.2.2), and annihilate in its trapped state. Obviously, there is also the possibility of de-trapping, which may occur in the case of shallow traps. And thirdly, the free positron may diffuse back to the surface, where it (apart from the possibility of reflection by the positron surface potential) either traps in a two-dimensional surface state or a near-surface defect (see, e.g., Steindl *et al.*, 1992; Walker *et al.*, 1990 and 1992), or is emitted as a free positron, or is emitted while forming a free positronium atom [see figure (2.1)].

By means of scattering processes positrons implanted close to the surface may return at the outer surface of the sample prior to

being completely thermalized (Coleman *et al.*, 1992a), leading to the emission of epithermal positrons and ‘hot’ positronium. This topic will be discussed in section 2.2.6.

In case of crystalline solids a part of the incident positrons may be diffracted at the surface or might channel along crystal axes or planes and penetrate deeper in the sample than with normal stopping (Logan *et al.*, 1988; Schultz *et al.*, 1988b).

## 2.2.2 Stopping

### Slowing down

In positron-annihilation studies positrons are implanted into the sample with kinetic energies that exceed the thermal energy  $k_B T$  considerably. After implantation the positron loses its energy due to a variety of interactions with the lattice (scattering, electron/phonon excitation, etc.).

The interaction of an incident beam of energetic positrons with a solid surface is different from that for electrons. The primary reason is the difference in charge, but the absence of a Fermi sea of positrons in the sample also plays a role. In addition, in most positron beam experiments there is at any time, on average, only one positron present in the solid, thus prohibiting the transfer of kinetic energy from the positron to others in the solid, so that these other particles account for subsequent scattering, as might be the case with electrons. These combined reasons account for the fact that, e.g., the cross section for scattering (and backscattering) is significantly larger for electrons than for positrons (Massoumi *et al.*, 1992; Schultz and Lynn, 1988; Valkealahti and Nieminen, 1984).

The stopping process of very energetic positrons (MeV domain) is like energetic electron stopping dominated by mass radiative stopping (*Bremsstrahlung*), in which the positron interacts with the screened Coulomb field of the nucleus or of one of the atomic orbital electrons, emitting a photon. Compared with electrons this energy-loss mechanism is less efficient for positrons (Schultz and Campbell, 1985; Schultz and Lynn, 1988).

The second stage in slowing down is primarily energy loss by

electron scattering. Below  $\sim 100$  keV most of the kinetic energy of a positron that enters a solid is lost through core and valence-electron excitations. Through these interactions the energy is reduced to a few tenths of an electronvolt within 1 ps (Perkins and Carbotte, 1970; Schultz and Lynn, 1988). At energies of a few keV even positron-induced Auger-electron emission has been observed, caused by *L*-shell electron ionization (Schultz and Lynn, 1988). From initial energy down to about 100 eV the positron energy loss  $dE/dt$  is roughly proportional to  $E^{-1/2}$ , where  $E$  is the energy of the positron (Nieminen and Oliva, 1980). In the medium energy range ( $\sim 50$  eV–10 keV) the stopping power (i.e. the mean energy loss per unit path length) of positrons is larger than that for electrons (Ashley, 1990).

### Thermalization

A positron that enters a metal is slowed down by electronic stopping until its energy is reduced to a few tenths of an electronvolt. Now the contribution of phonon scattering to the stopping process becomes more dominant and therefore accounts for the thermalization of the positron. Phonon excitations have a much lower energy transfer than electron interactions, so phonon stopping times are much longer than electron stopping times. While the time to slow down a positron to near-thermal energies amounts to less than a picosecond, phonon stopping times (for complete thermalization of the positron) are of the order of 10 ps (Carbotte and Arora, 1967; Schultz and Lynn, 1988).

In semiconductors and ionic solids positron stopping resembles stopping in metals, except that electron-hole creation ceases to be possible when the positron energy becomes less than the band gap. Thus, a wider region of energy must be lost to phonon modes in the absence of more efficient mechanisms, yielding longer thermalization times than in metals. In insulators this effect is even more pronounced. Positron energy loss in many insulators involves positronium formation in one way or another (Schultz and Lynn, 1988).

### The implantation profile

A mathematical description of the positron implantation profile, denoted as  $P(E, z)$ , has been obtained from Monte-Carlo calculations (Valkealahti and Nieminen, 1983 and 1984). It has been parameterized by a so-called Makhovian profile:

$$P(E, z) = \frac{m z^{m-1}}{z_0^m} \exp \left[ - \left( \frac{z}{z_0} \right)^m \right], \quad (2.1)$$

where  $P(E, z)dz$  is defined as the fraction of positrons entering the solid with initial energy  $E$  that will be stopped at a depth between  $z$  and  $z + dz$ . In equation (2.1) the shape parameter  $m$  is believed to be a function of both the atomic number  $Z$  of the material under investigation and the incident positron energy (Nielsen *et al.*, 1990; Asoka-Kumar and Lynn, 1990). The penetration parameter  $z_0$  is related to the mean implantation depth  $\bar{z}$  by

$$\bar{z} = z_0 \Gamma \left( 1 + \frac{1}{m} \right). \quad (2.2)$$

For  $m = 1$  equation (2.1) reduces to a simple exponential profile with  $\Gamma(2) = 1$  in equation (2.2), and for  $m = 2$  to the Gaussian derivative profile with  $\Gamma(\frac{3}{2}) = \sqrt{\pi}/2$ .

It is assumed that

$$\bar{z} = \frac{\alpha}{\rho} E^n. \quad (2.3)$$

In this expression  $\rho$  represents the density of the material ( $\text{g/cm}^3$ ) and  $\alpha$  ( $\text{g/cm}^2$ ) is usually treated as a constant (as a rule a factor  $(\text{keV})^{-n}$  is omitted from the units of  $\alpha$ , but it should be remembered that the energy has to be expressed in units of keV with the standard values of  $\alpha$ ).

Improved parameterizations of the positron implantation profile have been given by, e.g., Jensen and Walker (1990), Baker *et al.* (1991), and Ghosh *et al.* (1992). Monte-Carlo calculations have shown that the Makhov-profile of equation (2.1) underestimates the number of positrons near the surface (Ghosh *et al.*, 1992), but there is still no unanimity about a better parameterization which can be generally applied. However, detailed modifications of the implantation profile

mainly influence the analysis of experiments which use positrons returning to the surface as their basis. In that case the detailed shape of  $P(E, z)$  within a diffusion length of the surface is important. But for the analysis of, e.g., Doppler-broadening measurements, the model is concerned with the number of positrons annihilating in a slice of thickness  $\Delta z$  below the surface. In this case equation (2.1) yields good results as long as correct values for the parameters are employed (Coleman *et al.*, 1992b).

Today there is still no consensus about the proper values for the parameters of equations (2.1), (2.2), and (2.3) for most materials (e.g., Si). Therefore, for the analysis of the experiments in this thesis we have used the formerly generally accepted values for these parameters, which are  $m = 2.0(1)$ ,  $n = 1.62(5)$  and  $\alpha = 4.0(3) \mu\text{g}/\text{cm}^2$  (Vehanen *et al.*, 1987). Typical penetration depths of positrons lie in the order of a few  $\mu\text{m}$  for 25 keV positrons implanted in moderate density materials ( $\sim 2 \text{ g}/\text{cm}^3$ ).

### 2.2.3 Diffusion and trapping

#### The positron diffusivity

In analogy to holes in semiconductors the movement of the thermalized positron may be characterized by a *diffusivity*  $D_+$  and a *mobility*  $\mu$ . These two quantities are related by the Einstein equation

$$e D_+ = k_B T \mu, \quad (2.4)$$

with  $k_B$  denoting Boltzmann's constant ( $1.38 \times 10^{-23} \text{ J/K}$ ) and  $e$  the elementary charge ( $1.60 \times 10^{-19} \text{ C}$ ). The positron diffusivity determines how fast the thermalized positrons reach the traps.

Positron diffusion in solids is limited by phonon scattering. Under simple assumptions this yields the following expression for the positron diffusivity (Secger and Banhart, 1990):

$$D_+ = \frac{2\sqrt{2\pi} \rho c_\ell^2 h^4}{3 m_p^2 \epsilon_d^2 \sqrt{k_B T m_p}}. \quad (2.5)$$

Here  $\rho$  and  $c_\ell$  denote the density and longitudinal sound velocity of the material,  $\epsilon_d$  the deformation potential constant for positrons,  $m_p$  the

effective mass of the positrons, while  $\hbar$  represents Planck's constant divided by  $2\pi$  (i.e.  $1.05 \times 10^{-34}$  Js).

Equation (2.5) is valid only as long as the positron-phonon scattering is elastic, i.e. at temperatures higher than a critical temperature  $T_0 = 12m_p c_l^2 / k_B$ . Experiments have shown that the positron diffusivity for, e.g., silicon (from 30 K to 500 K) and Mo(111) indeed varies as  $T^{-1/2}$  (Huomo *et al.*, 1987; J. Mäkinen *et al.*, 1991; Soininen *et al.*, 1990 and 1992), although other materials show slight deviations (Schultz and Lynn, 1988). Typical room-temperature values of  $D_+$  are of the order of  $1 \times 10^{-4}$  m<sup>2</sup>s<sup>-1</sup>.

The positron diffusion length  $L_+$  during its bulk lifetime  $\tau_b$  in trap-free material is:

$$L_+ = \sqrt{D_+ \tau_b} = \sqrt{D_+ / \lambda_b}, \quad (2.6)$$

where  $\lambda_b$  is the positron annihilation rate. Note that diffusion lengths are of the order of 100 nm, i.e. small compared with the implantation depth. The measured values for the positron diffusivity in crystalline silicon at 300 K range from  $2.7 \times 10^{-4}$  m<sup>2</sup>s<sup>-1</sup> to  $3.1 \times 10^{-4}$  m<sup>2</sup>s<sup>-1</sup> (Nielsen *et al.*, 1985a; J. Mäkinen *et al.*, 1990b and 1991; Schultz *et al.*, 1988a), while the lifetime of free positrons in silicon is 217 ps (Würschum *et al.*, 1989; S. Mäkinen *et al.*, 1990). Equation (2.6) now yields  $L_+ = 250 \pm 10$  nm for positrons in silicon.

## Trapping

The wave function of a thermalized free positron is represented by a Bloch function with a De Broglie wavelength  $\lambda_{th}$  given by (Schultz and Snead, 1990):

$$\lambda_{th} = \frac{2\pi\hbar}{\sqrt{3m_p k_B T}} \sim (6.2 \text{ nm}) \sqrt{\frac{300}{T}}, \quad (2.7)$$

i.e. it is localized on a length scale of  $\sim 10$  nm, which is usually larger than the positron mean free path ( $\sim 1$  nm) or the extent of a trapped state ( $\sim 0.1$  nm) (see McMullen, 1985).

If there is an open-volume defect in a metal lattice, the positron wave function can condense into the potential minimum with high

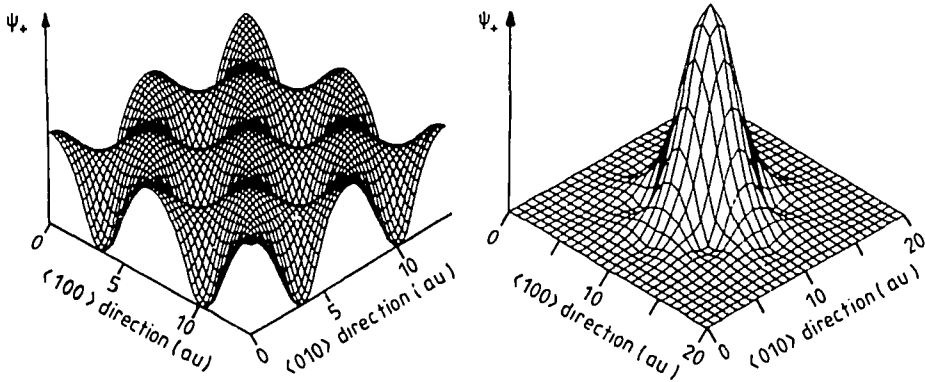


Figure 2.2: Wave function of a delocalized positron in a perfect *fcc* nickel lattice (*left*) and of a positron localized in a vacancy in *fcc* nickel (*right*). From Puska and Nieminen (1983).

efficiency (Hodges, 1970). Puska and Nieminen (1983) have calculated the change of the wave function of a positron that undergoes the transition from a freely-diffusing state into a vacancy-localized state, which appeared to be dramatic (see figure 2.2).

In case of materials with a uniform defect distribution, due to trapping in defects the positron diffusion length [see equation (2.6)] reduces to an effective diffusion length  $L_{+,eff}$ :

$$L_{+,eff} = \sqrt{\frac{D_+}{\lambda_b + \kappa_t}}, \quad (2.8)$$

with the positron trapping rate into defects,  $\kappa_t$ , defined as

$$\kappa_t = \nu_t n_t. \quad (2.9)$$

In this equation  $\nu_t$  represents the specific positron trapping rate for a certain defect and  $n_t$  the defect concentration. Generally, in some material every defect type has a different specific trapping rate associated with it (Nieminen and Manninen, 1979). Specific trapping rates for monovacancies in metals are typically of the order of  $10^{15} \text{ s}^{-1}$ , while trapping rates for dislocations are of the order of  $0.5 \text{ cm}^2 \text{ s}^{-1}$  (note that the unit for dislocation densities is  $\text{m}/\text{cm}^3$ ). Pure dislocation lines form only shallow traps (binding energies of about 0.1 eV), but they

can be precursor states (through thermal detrapping) for deeper traps, like vacancies and single jogs on the dislocation line (binding energies of about 1 eV, i.e. still smaller than the values for bulk vacancies which are of the order of 1.5–2 eV; Häkkinen *et al.*, 1990; Hashimoto and Kino, 1991; Jensen *et al.*, 1988b; Park *et al.*, 1986).

### The thermal positron diffusion equation

All processes to which thermal positrons are subjected, viz. implantation, diffusion, drift (due to an electric field) and trapping or annihilation of (free) positrons, can be combined in a single equation, the (one-dimensional) steady-state positron diffusion equation:

$$D_+ \frac{d^2 c(z)}{dz^2} - \frac{d[v_d(z)c(z)]}{dz} - [\nu_i n_i(z) + \lambda_b]c(z) + I(E, z) = 0. \quad (2.10)$$

In addition to earlier defined symbols,  $c(z)$  represents the steady-state positron distribution as a function of depth  $z$ , while the positron drift velocity  $v_d$  depends on the (local) electric field strength  $\mathcal{E}(z)$  according to  $v_d(z) = \mu \mathcal{E}(z)$ . Finally,  $I(E, z)$  represents the positron implantation rate that yields thermalized positrons at depth  $z$  and it depends on the energy of the incident positron beam. A further analysis of this differential equation can be found in Schut (1990), and Van Veen *et al.* (1990).

## 2.2.4 Surface and interface processes

### The positron and positronium workfunction

In order to leave the material through a surface a positron must gain an energy  $\phi_+$ , the so-called positron workfunction. This energy is defined as the minimum energy required to move a positron from a point inside to one just outside the surface and equals:

$$\phi_+ = -D - \mu_+, \quad (2.11)$$

where  $\mu_+$ , the (bulk) positron chemical potential, is defined as the difference between the bottom of the lowest positron band and the zero crystal level (at a temperature of 0 K) and  $D$  represents the

surface dipole barrier, which is primarily caused by the tailing of the electron distribution into the vacuum. Positron workfunctions of the more common metals are tabulated in Boev *et al.* (1987), Schultz and Lynn (1988), and Jibaly *et al.* (1992).

For positrons the force due to the dipole barrier is directed out of the solid [whence the minus sign before  $D$  in equation (2.11)]. This causes the positron workfunction to be nearly zero and, in some cases (e.g., in case of a clean tungsten surface), even negative, allowing the emission of (slow) positrons into the vacuum (Gullikson *et al.*, 1988a; Tong, 1972).

The positronium workfunction,  $\phi_{P_s}$ , equals (Schultz and Lynn, 1988):

$$\phi_{P_s} = \phi_+ + \phi_- + E'_{P_s} - E_{P_s}, \quad (2.12)$$

where  $E'_{P_s}$  represents the positronium binding energy while in the solid,  $E_{P_s} = 6.8$  eV the binding energy in vacuum and  $\phi_-$  the electron workfunction defined as:

$$\phi_- = +D - \mu_-, \quad (2.13)$$

with  $\mu_-$  the electron's chemical potential.

In metals  $E'_{P_s}$  vanishes. For, e.g., Al(100) at 300 K  $\phi_+ = -0.16$  eV and  $\phi_{P_s} = -2.6$  eV (Gullikson and Mills, 1987), but both  $\phi_+$  and  $\phi_{P_s}$  are positive for the alkali metals due to their small dipole potential. Now, the branching of the positron at the surface is roughly as follows: The probabilities for branching into positronium and a surface-state are about equal, while the slow positron emission rate is approximately proportional to  $\{-\phi_+\}^{1/2}$  (for  $\phi_+ < 0$ ). In insulators positronium may exist within the material. The positron workfunction of insulators is typically a few eV positive, but the positronium workfunction is generally negative, the positronium being emitted without energy loss into the vacuum (Mills, 1988).

### Potential steps at interfaces

At the interface between two materials, positrons experience an electrostatic potential. Due to the fact that both materials must have the same Fermi level, a potential step is induced equal to the difference

in the electron chemical potentials ( $\Delta\mu_-$ ). This so-called interfacial dipole is the same for positrons and electrons but the sign is opposite. The difference in the positron chemical potentials ( $\Delta\mu_+$ ) between the materials further modifies the height of the potential step.

At the interface between two metals  $A$  and  $B$  a positron experiences the following potential  $\Delta E_+$

$$\Delta E_+ = \Delta\mu_- + \Delta\mu_+ = (\mu_+^B - \mu_+^A) + (\mu_-^B - \mu_-^A) = \chi_+^B + \chi_+^A, \quad (2.14)$$

where the positron affinity  $\chi_+$  is defined as  $\chi_+ = \mu_- + \mu_+$ . In case of a junction between two metals, the positron prefers being in the material with the lowest affinity (Huttunen *et al.*, 1990a). Positron affinities for metals are tabulated in Puska *et al.* (1989).

The height of the interface potential step  $\Delta E_+$  is of the order of 1 eV, much larger than the thermal kinetic energy ( $\sim k_B T$ ). Therefore, it is highly probable that positrons coming to an interface from a material with a more negative positron affinity are reflected at the interface. Additionally, when positrons implanted in some material approach the outer surface, reflection from the surface potential may have a considerable influence on the positron motion, especially at low temperatures (Britton *et al.*, 1989; Huttunen *et al.*, 1990b).

## 2.2.5 Annihilation

### The $S$ -parameter

In case of  $2\gamma$  annihilation, due to the momentum of the positron-electron pair the energies of the two  $\gamma$  photons deviate from the exact value of 511 keV (see section 1.2.2). This Doppler broadening of the peak is typically a few hundred electronvolt, whereas the instrumental width of the detector resolution is typically 1.3 keV.

In general, instead of deconvolution, for convenience the 511 keV peak is characterized by a so-called  $S$  (*shape*) parameter, as introduced by MacKenzie *et al.* (1970). This  $S$ -parameter is defined as the ratio of the area  $B$ , a fixed central part of the peak, and the total area  $A + B + C$  of the 511 keV peak, as illustrated in figure 2.3. So:

$$S = \frac{B}{A + B + C}. \quad (2.15)$$

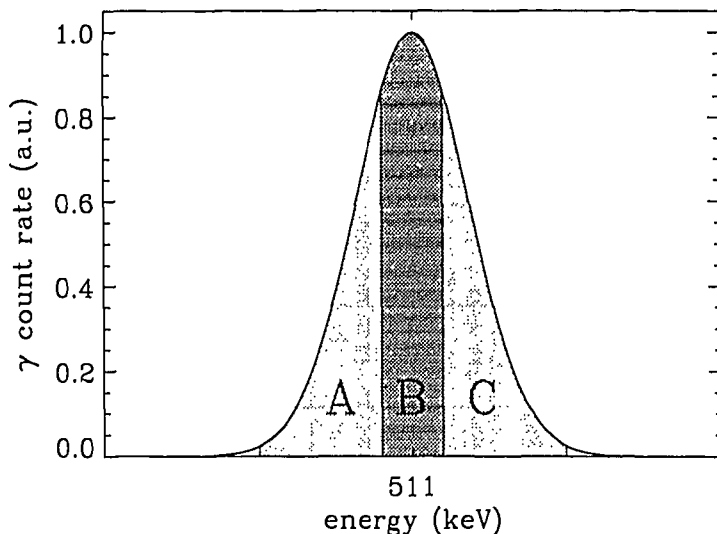


Figure 2.3: The areas  $A$ ,  $B$ , and  $C$  below portions of the 511 keV peak (after convolution with the instrumental resolution profile). The  $S$ -parameter is defined as  $B/(A + B + C)$ .

The energy intervals associated with  $A$ ,  $B$ , and  $C$  are chosen to obtain the maximum sensitivity of  $S$  to the Doppler broadening of the 511 keV peak, which in practice corresponds to  $S$ -parameters of about 0.5 (Leo, *et al.*, 1981).

It should be remembered that the absolute value of  $S$  carries no direct physical information, e.g., due to its dependence on the resolution of the photon-detection system. On the other hand, a normalized  $S$ -parameter, e.g., defined as

$$S = S/S_{c-si}, \quad (2.16)$$

where  $S_{c-si}$  represents the measured  $S$ -parameter for crystalline silicon, appears to show a reasonable independence of the measuring equipment and can be used for absolute quantification.

### Correlation between $S$ and material properties

Since  $S$  is an overall parameter of the 511 keV peak, it reflects the total momentum available in the positron-annihilation processes. Free

(unlocalized) positrons can annihilate with both core electrons and conduction electrons, whereas the wave function of a positron trapped in a vacancy has a relatively smaller overlap with core electrons due to the absence of the ion core in the defect. Therefore, trapped positrons, as opposed to free positrons, have a larger probability for annihilation with conduction electrons, which have energies lower than that of core electrons. As a result annihilation at vacant lattice sites reduces the high-momentum components in the positron-electron momentum distribution of trapped positrons as compared with annihilation of free positrons. With respect to a defect-free reference sample, more annihilation of positrons in vacancies results in the narrowing of the annihilation peak, i.e. an increase of  $S$ .

Therefore, generally speaking, a low  $S$  indicates that a large fraction of the total number of positrons annihilates in a free (delocalized) state, while a higher value of  $S$  indicates that the positrons mainly annihilate in traps. It should be noted that this is not an absolute rule, since annihilation in, e.g., oxygen-related defects also result in a lower  $S$  (see, e.g., Dannefaer and Kerr, 1986; Chilton *et al.*, 1990, and Tabuki *et al.*, 1992). In general, the characteristic value of  $S$  for dislocations is similar to or lower than that for monovacancies (Uedono *et al.*, 1992).

Care should be taken when trapping rates derived from positron-lifetime measurements are applied for the analysis of Doppler-broadening measurements, since the wave function of a trapped positron still has overlap with the wave functions of the electrons in the bulk of the sample. Therefore, trapped positrons annihilating with 'bulk' electrons also contribute to the  $S$ -parameter, but yield the 'normal' bulk lifetime (Roizing *et al.*, 1992; for the relation between lifetime and Doppler-broadening measurement, see also Schaffer *et al.*, 1992). This effect will be less pronounced for positrons that are more strongly localized in a trap.

At the outer surface of a specimen or in large voids in semiconducting or insulating materials, positronium may be formed. The annihilation of  $p$ -Ps is observed in the Doppler-broadened annihilation peak as an additional narrow component because of the low intrinsic momentum of the positronium atom.

Every non-reemitted positron entering some material annihilates

either from a surface state (yielding an  $S$ -parameter  $S_s$ ), a positronium bound state (yielding  $S_{Ps}$ ), a free state (yielding  $S_b$ ) or from a trapped state localized at a defect (yielding  $S_{t,i}$ , where  $i = 1 \dots n$  represents the trapping in  $n$  different types of defects). Denote the fractions annihilating from these states by respectively  $f_s$ ,  $f_{Ps}$ ,  $f_b$  and  $f_{t,i}$ , then the annihilation characteristics of the different annihilation sites will be combined in the overall  $S$ -parameter:

$$S = \frac{f_s S_s + \beta f_{Ps} S_{Ps} + f_b S_b + \sum_{i=0}^n f_{t,i} S_{t,i}}{f_s + \beta f_{Ps} + f_b + \sum_{i=0}^n f_{t,i}}, \quad (2.17)$$

while  $f_b$  and  $f_{t,i}$  are related to each other by:

$$\frac{f_b}{\sum_{i=1}^n f_{t,i}} = \frac{\lambda_b}{\sum_{i=1}^n \kappa_{t,i}}, \quad (2.18)$$

where  $\kappa_{t,i}$  is the positron trapping rate for defects of type  $i$ . The constant  $\beta$  in equation (2.17) accounts for the fact that only  $p$ -Ps annihilations contribute to the 511 keV peak (Nielsen *et al.*, 1985b).

Equation (2.17) shows that the  $S$ -parameter carries information of the defects at which the positrons annihilate. Especially defects with a high specific trapping rate or with a high concentration [compare equation (2.9)] may influence the annihilation-peak width significantly.

It should be noted that even in defect-free materials the positrons may preferentially annihilate at certain sites. E.g., for positrons in binary semiconductors like GaAs Independent Particle Method (IPM) and Empirical Pseudopotential Method (EPM) calculations have shown that positrons have a strong affinity for one sort of atom. Positrons may therefore preferentially annihilate with the electrons of that sort of atom in the compound semiconductor, e.g., in case of GaAs more positrons annihilate with electrons from arsenic atoms than with electrons from gallium atoms (Aourag *et al.*, 1990; Aourag and Khelifa, 1991).

### Deconvolution of the Doppler-broadened 511 keV peak

The broadening of the 511 keV peak is masked to a certain extent by the energy resolution of the photon-detection system. In order to remove this instrumental dependency the peak may be deconvoluted by the algorithm of Press *et al.* (1986), of which the mathematics is described below.

Say,  $r(E)$  represents the response function of the photon-detection system as a function of the photon energy  $E$ . Due to this instrumental resolution an uncorrupted photon-energy distribution  $u(E)$  will cause the system to release a smeared-out signal  $s(E)$ , which is the convolution of  $u(E)$  and  $r(E)$ :

$$s(E) = u(E) * r(E) = \int_{-\infty}^{\infty} r(\epsilon) u(E - \epsilon) d\epsilon, \quad (2.19)$$

which equals

$$S(\omega) = R(\omega) U(\omega) \quad (2.20)$$

in Fourier-space, where  $S$ ,  $R$  and  $U$  are the Fourier transforms of  $s$ ,  $r$  and  $u$  respectively.

In practice, the measured detector signal  $c(E)$  contains an additional component of noise  $n(E)$ :

$$c(E) = s(E) + n(E). \quad (2.21)$$

The contribution of the noise may be removed during deconvolution by adding a filter  $\phi(E)$  or  $\Phi(\omega)$ , so that deconvolution of the measured signal  $C(\omega)$  produces a signal  $\tilde{u}(E)$  or  $\tilde{U}(\omega)$  that is as close as possible to the uncorrupted signal  $U(\omega)$ :

$$\tilde{U}(\omega) = \frac{C(\omega) \Phi(\omega)}{R(\omega)} \quad (2.22)$$

Choosing  $\Phi(\omega)$  so that  $\tilde{u}(E)$  will be a least-square fit of  $u(E)$ , requires minimization of:

$$\int_{-\infty}^{\infty} |\tilde{u}(E) - u(E)|^2 dE = \int_{-\infty}^{\infty} |\tilde{U}(\omega) - U(\omega)|^2 d\omega. \quad (2.23)$$

which, after substitution of equations (2.20) and (2.22), requires the integrand of

$$\int_{-\infty}^{\infty} |R(\omega)|^{-2} \{ |S(\omega)|^2 |1 - \Phi(\omega)|^2 + |N(\omega)|^2 |\Phi(\omega)|^2 \} d\omega \quad (2.24)$$

to be minimized with respect to  $\Phi(\omega)$  at every value of  $\omega$ . On the assumption that  $\Phi(\omega)$  is a real function, differentiation with respect to  $\Phi$  and setting the result to zero gives the following expression for the optimal filter:

$$\Phi(\omega) = \frac{|S(\omega)|^2}{|S(\omega)|^2 + |N(\omega)|^2}. \quad (2.25)$$

From the measured spectrum  $C(\omega)$  the absolute values of the noise component  $N(\omega)$  and the signal component  $S(\omega)$  can be estimated. Equation (2.25) now yields the optimal filter, which can be substituted in equation (2.22) for obtaining a least-square fit of the uncorrupted signal  $\tilde{U}(\omega)$ . See further section 3.2.5.

## 2.2.6 Epithermal positrons

Until recently, positrons have always been considered to be thermalized immediately after their implantation. Therefore, the transport of positrons has been described by a single-velocity diffusion equation. However, the observed emission of fast positrons and positronium (Gullikson and Mills, 1986; Howell *et al.*, 1986) and trapping of non-thermalized positrons (Nielsen *et al.*, 1986) have led to a renewed interest in positron stopping and thermalization.

A simple transport model of thermal and epithermal positrons in solids has been proposed by Kong and Lynn (1990a and 1990b). They found that the thermal-positron diffusion equation is a good approximation at high positron incident energies when inelastic scattering is dominant over elastic scattering and bulk trapping. However, especially for solids with inefficient stopping mechanisms at near-thermal energies (insulators, semiconductors), the number of reemitted epithermal positrons at the surface is not negligible. On the other

hand, in metals the epithermal emission of positrons is dominated by elastic scattering of positrons (Britton *et al.*, 1988).

The other important effect of non-thermal positrons is epithermal positron trapping. This effect plays a significant role when the epithermal trapping rate is comparable to or becomes higher than the inelastic scattering rate (Lynn *et al.*, 1987). Jensen and Walker (1990) have performed detailed calculations of non-thermal positron trapping in metals and have concluded that, even if resonances are present in the momentum-dependent trapping rates, the differences between trapping from a non-thermal and a thermal distribution are exceedingly small. Only if the epithermal trapping rate and/or annihilation rate deviates from the thermal rate for a sufficient fraction of the thermalization time, the parameters measured in positron studies are influenced. Therefore, at least for positron studies of vacancies in metals, non-thermal trapping is not important.

However, in some cases epithermal trapping may play a role. Jensen and Walker (1990) mention the following cases: trapping in large voids at low temperatures, defect trapping in semiconductors (especially positively charged defects, since the positron has to tunnel through the potential barrier surrounding the defect) and trapping in the presence of a strong sink in the system, e.g., a surface when positrons implanted at a low energy return to the surface prior to complete thermalization. In the latter case a large fraction of the positron trapping may be accounted for by trapping of epithermal positrons.

## 2.3 Positron beam experiments

In experimental studies the positron is most frequently produced in the radioactive decay of a suitable isotope (see table 2.1). Either this positron source is adjacent to the specimen being studied (in which case the 'fast' positrons are used) or the positron source is separated from the sample by a moderator foil so that the positrons have to be guided to the sample by an electrostatic and/or magnetic beam.

In case of slow positron experiments the positrons are moderated by implantation in some negative positron workfunction mate-

Table 2.1: Decay data of positron emitters

Radionuclide	half-life	Maximum energy	Principal $\gamma$ rays energy	intensity
$^{22}\text{Na}$	2.6 years	545 keV	1275 keV	100 %
$^{58}\text{Co}$	71 days	470 keV	810 keV	99 %
$^{64}\text{Cu}$	12.8 hours	660 keV	1340 keV	0.5 %

rial. Of the metal moderators single-crystal tungsten gives the most favourable yield (0.003 slow positrons per fast positron from a  $^{58}\text{Co}$  source), but recently insulating moderators came into use, like rare gas solids and synthetic diamond (Mills, 1988; Massoumi *et al.*, 1991; Brandes *et al.*, 1992a and 1992b; Merrison *et al.*, 1992).

The positrons leave the moderator with a kinetic energy of a few eV (equalling the workfunction). Subsequently, they are electrostatically accelerated to energies ranging from say 100 eV to 50 keV and are guided to the sample, into which these monoenergetic slow positrons are implanted.

$S$ -parameter measurements consist of determining the overall  $S$ -parameter [see equation (2.17)] by measuring the 511 keV peak width [see figure 2.3 and equation (2.15)] as a function of the positron incident energy. From the measured contribution of surface-related annihilation processes [positronium formation and trapping in surface states; see equation (2.17)] the effective positron diffusion length in the top region of the sample may be estimated [compare equation (2.8)].

The statistical error  $\sigma_S$  in Doppler  $S$ -parameter measurements is estimated from a binomial distribution (Huomo *et al.*, 1989):

$$\sigma_S = \sqrt{\frac{S(1-S)}{N}}, \quad (2.26)$$

where  $S$  is the measured  $S$ -parameter and  $N$  represents the total number of counts in the 511 keV peak. In order to detect changes in  $S$  of the order of a fraction of a percent, the total number of counts in the 511 keV peak has to be about  $1 \times 10^6$ .

When electric fields are present in the sample, e.g., in semiconductor structures, these fields may be 'switched off' by measuring the

sample at elevated temperatures ( $\sim 200^\circ\text{C}$ ), since at higher temperatures thermally generated carriers dominate other types of carriers. It should be noted that heating of the sample also influences the diffusion length of untrapped positrons [see equation (2.5)].

Due to the known  $2\gamma/3\gamma$  decay ratio of positronium the fraction of positronium  $f_{ps}$  that is formed at the outer surface of a sample mounted in vacuum can be deduced from the ratio  $R$  of counts accumulated in different regions of the positron-annihilation spectrum (Deutsch and Dulet, 1951; Mills, 1978; Schultz *et al.*, 1984):

$$f_{ps} = \left[ 1 + \frac{P_1}{P_0} \frac{R_1 - R}{R - R_0} \right]^{-1}, \quad (2.27)$$

where  $R = (T - P)/P$ , with  $T$  the number of counts accumulated in the photon-energy region below 511 keV ( $3\gamma$  events; the energy of these  $\gamma$ -photons ranges continuously from 0 to 511 keV) and  $P$  the number of counts in the 511 keV peak region of the spectrum ( $2\gamma$  events).  $R$  equals  $R_0$  if there is no positronium formation and equals  $R_1$  in case of 100 % positronium. The factor  $P_1/P_0$  accounts for the probability of three photon contributions to the number of counts in the peak region.

Actually, samples of interest for positron depth profiling normally do not contain a uniform defect profile, but consist of several different layers (with or without built-in electric fields) or contain some defect profile, e.g., due to damage caused by ion implantation. In order to analyse this type of positron-annihilation data the diffusion equation [see equation (2.10)] must be solved iteratively, which can be done with the modelling and fitting program VEPFIT. For a description of this program see Schut (1990), or Van Veen *et al.* (1990).

In the analysis of positron beam measurements, several effects should be taken into account. First of all, the influence of epithermal positrons. Contrary to Huomo *et al.* (1989) there is no need to exclude the positron data of the first few keV when epithermal effects are taken into account. In the VEPFIT program this is done by the introduction of a so-called epithermal scattering length (in order to estimate the fraction of positrons returning to the sample), annihilation of which yields a separate  $S$ -parameter. Other surface-related effects (like reflection of backdiffusing positrons at the surface) are accounted

for in the program by the surface absorption length. This quantity has no direct physical meaning other than that it indicates how to extrapolate the solution of equation (2.10) at the surface boundary (radiative boundary conditions). For a discussion, see Schut (1990) or Van Veen *et al.*, 1990.

Secondly, at low incident energies the profile of thermalized positrons has a width of the same order as the mean free path of the positrons during thermalization (Nieminen and Oliva, 1980). Therefore, the spatial distribution of the positrons reaching thermal equilibrium is broader than the parameterized implantation profile [see equation (2.1)]. In addition, backscattering effects from reemitted positrons returning to the sample are another reason for the broadening of the Makhovian implantation profile (Huomo *et al.*, 1989). However, as discussed in section 2.2.2 these effects are more pronounced for surface-related experiments than for the positron depth-profiling experiments of this thesis.

Thirdly, according to Huomo *et al.* (1989) the measured  $S$ -parameter does not scale linearly proportional to the current of positrons returning to the surface due to positronium emission. This effect leads to relatively higher  $S$ -values, but it is masked to a certain extent by the emission of positronium formed from non-thermal positrons that tends to turn the measured  $S$ -parameter downwards. The absolute value of these combined effects is at most a few percent of the difference between the  $S$ -parameter values at low and high incident energy in case of 30–50 % positronium emission.

In practice, due to these effects the errors in the fitted parameters of positron depth-profiling measurements are estimated to be at most 1 % in the  $S$ -values and up to 10 % in fitted values for all lengths (diffusion lengths, depths of layer boundaries, etc.).

NEXT PAGE(S) left BLANK.

# Chapter 3

## The positron beam and auxiliary techniques

### 3.1 Introduction

The first section of this chapter (section 3.2) contains a description of the Delft Variable Energy Positron Beam (VEP). This beamline is located at the Interfaculty Reactor Institute of the Delft University of Technology and was used for the positron-annihilation experiments described in this thesis.

During the period 1984–1986 this positron facility has been designed and constructed and in March 1987 its first  $^{22}\text{Na}$  positron source was installed. After a period of testing the beamline was officially inaugurated in April 1988. In the following years the beam was adjusted by several minor changes in the configuration in order to optimize its performance. Finally, in January 1992 a new, stronger  $^{22}\text{Na}$  positron source was purchased and installed.

In this chapter a short description will be given of the beam configuration (section 3.2.1), the sample holder (section 3.2.2), the built-in ion beam for *in-situ* low-energy ion implantation (section 3.2.3) and the photon-detection system (section 3.2.4). In addition, a discussion on the beam performance is presented in section 3.2.5.

The positron-annihilation experiments were partly supplemented by other techniques. The second part of this chapter (section 3.3)

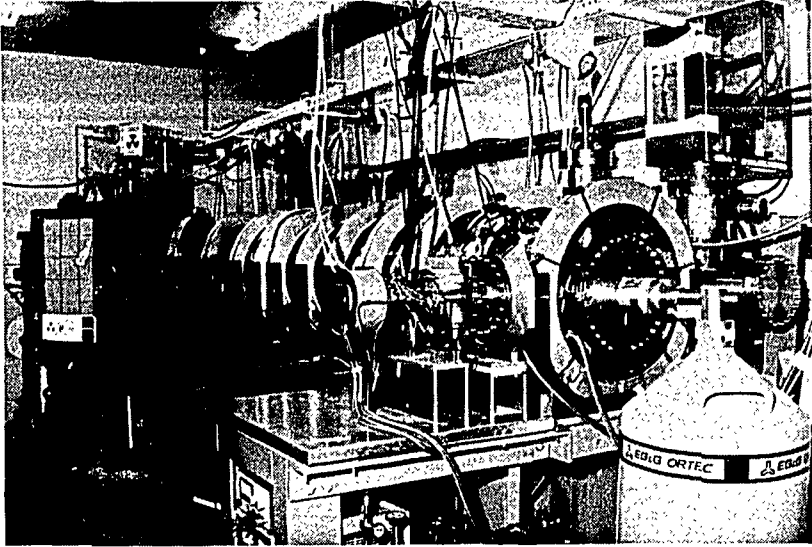


*Figure 3.1:* Photograph of the VEP in its current configuration.

provides a short description of these techniques, which include Free Carrier Lifetime Measurements (section 3.3.1), Raman spectroscopy (section 3.3.2), Small-Angle X-ray Scattering (section 3.3.3) and Nuclear Reaction Analysis (section 3.3.4).

## 3.2 The Delft Variable Energy Positron Beam

### 3.2.1 Design of the VEP

The positron-annihilation Doppler-broadening experiments have been performed with the Delft Variable Energy Positron Beam, commonly abbreviated as ‘VEP’. A photograph of this facility is shown in figure 3.1. An in-depth description of the VEP has been given by Schut (1990), so the account in this chapter will be confined to recent modifications of the equipment and to the beam performance.

Figure 3.2 shows a schematic reproduction of the VEP, a vacuum

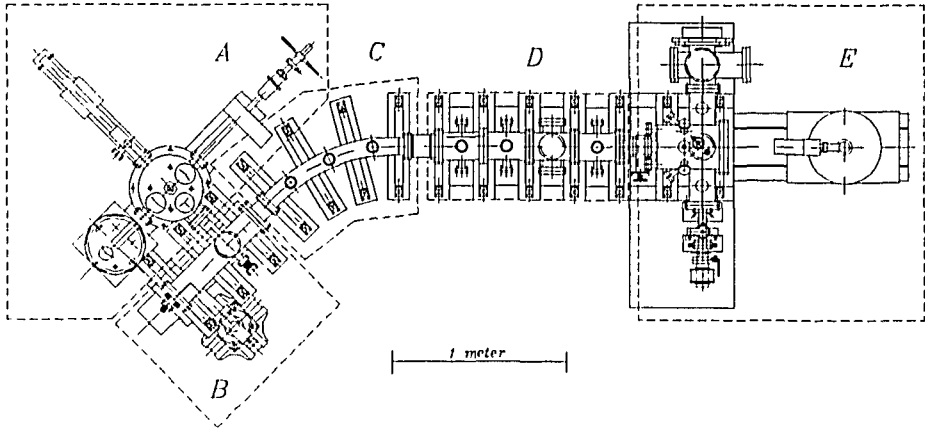


Figure 3.2: Schematic drawing of Delft Variable Energy Positron Beam (VEP). The VEP consists of a section for source storage (A), a source and moderator section (B), a bent section used for positron-energy filtering (C), a section used for positron acceleration (D) and the sample chamber and photon-detection area (E).

system that consists of several interconnected parts. The figure shows the source-storage section (A), the source and moderator area (B), the bent section used for positron-energy filtering (C), the section for beam acceleration (D), and, finally, the sample chamber and photon detection area (E).

The positron source, positioned in the vacuum chamber in the source section, consists of a 70 mCi  $^{22}\text{NaCl}$  source (90 % positron decay events), obtained from the Brookhaven National Laboratory (New York, U.S.A.). The emitted positrons are moderated by a 7  $\mu\text{m}$  thick 99.95 % pure polycrystalline tungsten foil (obtained from Goodfellow, Cambridge, United Kingdom) in transmission-moderation geometry.

The reemitted positrons are pre-accelerated to an energy of 115 eV and subsequently transported from the source area to the sample chamber by a 10 mT static axial magnetic field produced by 14 coaxial solenoids positioned in a Helmholtz configuration. A bent tube with a 1 m radius of curvature provides on the one hand additional filtering of fast moving positrons, on the other hand prevention of a direct line of sight between the photon detector positioned at the end of the positron beam and the positron source.

After passing the curved section the positrons are accelerated to their final energy (with a maximum of 30 keV), achieved by applying a high voltage (obtained from a Heinzinger HNC 40000-1 high voltage supply) to the beam section before the acceleration plates. The accelerated positrons enter the sample chamber through a 10 mm diaphragm and finally hit the sample.

A grid is located at the entrance of the sample chamber. Positive or negative voltages can be applied to this grid. With positive grid voltages (typically +50 V) reemitted positrons from the sample are forced to return to it. By applying a negative grid voltage in combination with a switched-on (trochoidal)  $\vec{E} \times \vec{B}$ -filter the reemitted positrons are prevented from returning to the sample. The  $\vec{E} \times \vec{B}$ -filter is necessary because without it, the reemitted positrons reflect at the accelerator package and return to the sample. The filter focuses incoming positrons on the sample, but reemitted positrons are deflected so that they end up hitting the sample chamber. An additional 80 mm long, 8 mm bore copper diaphragm can be positioned in front of the specimen in order to allow the study of small samples. The sample chamber can be closed off from the rest of the vacuum system by a viton sealed 60 mm ID valve.

With the exception of the positron-source storage vessel all parts meet the requirements set for operation under ultra-high vacuum (UHV) conditions. Pumping down from atmospheric pressure is done with a 145 l/s turbomolecular pump (Leybold Turbovac 150 CSV) in combination with a rotary roughing pump. During operation the pressure in the sample chamber was typically  $10^{-5}$  Pa, which could be reached without baking the system after changing the samples. The low pressure was achieved by several triode ion-getter pumps with capacities varying from 25 to 200 l/s.

### **3.2.2 The sample holder**

The samples for positron-annihilation study with the VEP are mounted on a rotatable sample holder. When the sample is attached to this holder, it can be placed either in front of the positron beam in order to perform the positron measurements or, after a 90° rotation, in front of the ion source in order to carry out ion implantations. The

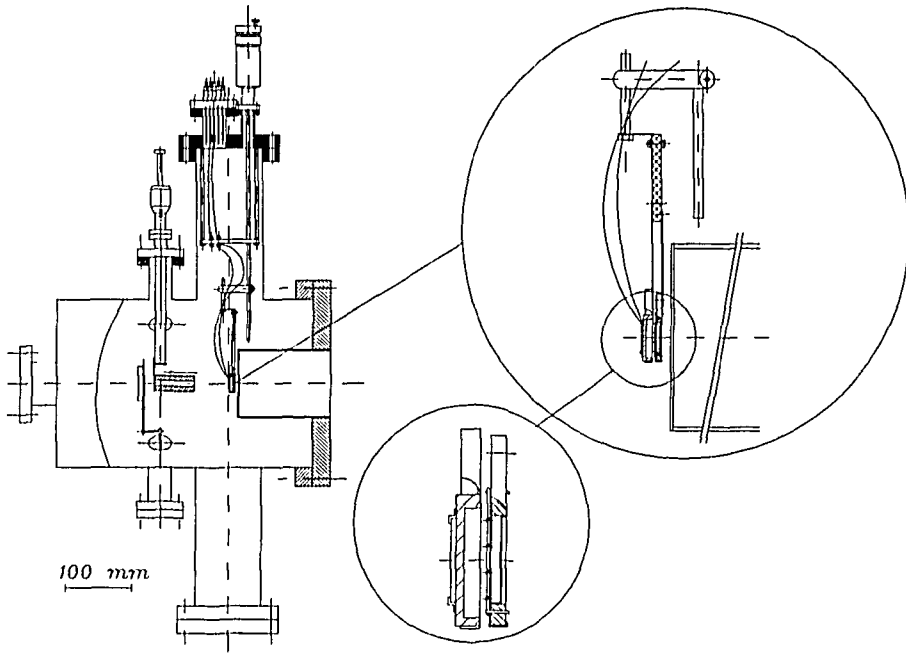


Figure 3.3: Cross-section of the sample chamber of the VEP with the sample holder. The molybdenum block with a mounted sample and the ceramic frame with the filament are shown in close-up.

sample holder is shown in figure 3.3.

The sample holder is connected to the 6" flange at the top of the detection chamber. The flange is provided with one mini CF port at which a rotary motion is connected, and one  $2\frac{3}{4}$ " port provided with a 7-pin electrical feedthrough. The position of the ports on the 6" flange is chosen so that the heart line connecting the two ports stands at an angle of  $45^\circ$  with the direction of the beam (see figure 3.4).

The sample holder is mounted on a spindle parallel to the spindle of the rotary motion, to which it is adjustably connected with a cross rod. To the lower end of the former spindle an (electrically insulating) ceramic plate ( $\text{Al}_2\text{O}_3$ ) is attached, at which in turn both a molybdenum block for holding the sample and a window-shaped ceramic frame ( $\text{Al}_2\text{O}_3$ ) with the filament are fastened.

From the middle of the 5 mm thick molybdenum block material has been removed reducing the thickness to  $\sim 1.5$  mm. When the

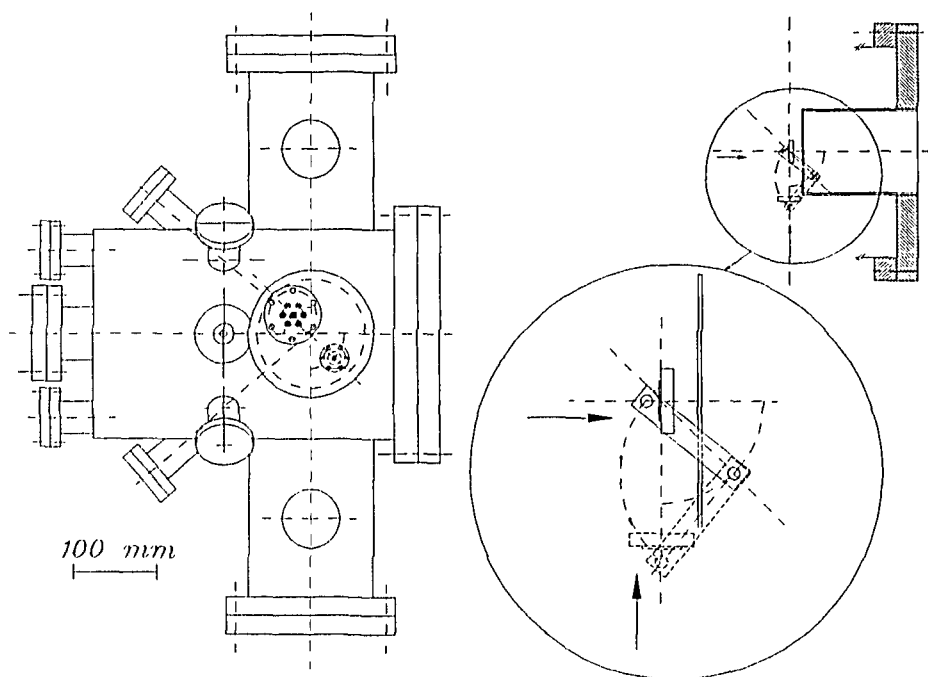


*Figure 3.4:* Top view of the sample chamber (left) and of the sample holder relative to the beam (right). The sample can be positioned facing both the positron beam and the ion source.

sample holder is in a position in front of the beam, the beam hits the centre of the molybdenum block. The sample can be spotwelded with tantalum strips onto the polished front side of the molybdenum block.

The ceramic frame, positioned behind the molybdenum block, contains small platinum rings through which thoriated tungsten wire has been twisted, acting as a filament. At the rear side of the ceramic frame a thin tantalum heating shield is placed. Due to its electrical isolation it is possible to apply a high voltage between the filament and the molybdenum block in order to heat the sample by electron bombardment. In this way the sample can be heated up to 900 °C.

The sample temperature is measured with a W3%Re-W25%Re thermocouple, which can be attached to the sample. When positron measurements are done while heating the sample, the molybdenum block can be grounded. Internally, all electrical components are connected to the 7-pin feedthrough.

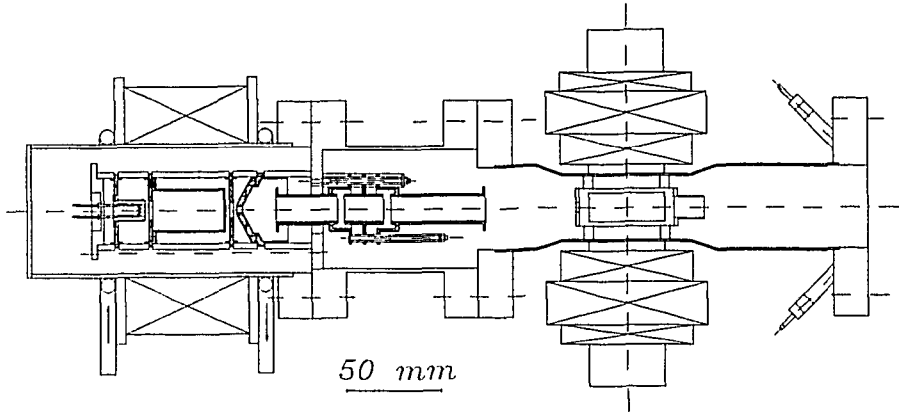


Figure 3.5: Cross-section of the ion source built in the VEP. Electrons emitted from the filament (left) ionize the gas in the ionization chamber. The extracted beam passes through a 3-element Einzel-lens system and a Wien filter. The deflection plates are not shown because they are located in the sample chamber (compare figure 3.6).

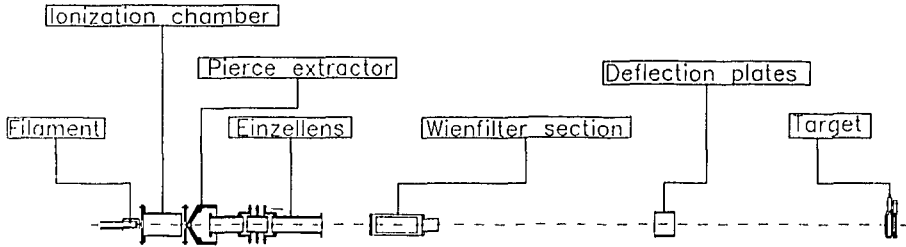


Figure 3.6: The electrodes and lenses of the ion-beam system (on scale).

### 3.2.3 The ion source

The VEP is equipped with an ion source for *in-situ* low-energy ion implantations into the sample mounted in the sample chamber. A schematic drawing of the ion source is shown in figure 3.5, while the lens system is represented in figure 3.6.

An ion source of the electron-impact type is placed on the sample chamber at a  $90^\circ$  angle with the direction of the positron beam. The sample mounted on the sample holder described in section 3.2.2 can be positioned facing the exit side of the ion beam system.

Electrons from a filament in the ion source cause ionization of gas (e.g., hydrogen or helium) entering the system through a gas inlet/reduction system and generate a low-pressure plasma (0.001 mbar) in the ionization chamber. Ions are extracted with a Pierce extraction geometry. The beam is transported and focused by a 3-element Einzel-lens system onto the target. Ions can be accelerated to energies ranging from say 100 eV up to 2.5 keV. Depending on the energy ion currents up to 1  $\mu$ A can be attained.

Deflection plates at low-frequency AC voltages generate a swept beam for uniform implantation over a large surface of the sample (frequencies around 50 Hz and 460 Hz for the horizontal and vertical sweep respectively). Mass selection of the beam is performed by an  $\vec{E} \times \vec{B}$  Wien filter, mounted in line with the optical axis of the ion-beam system (see Van Veen *et al.*, 1980). The resolving power of  $M/\Delta M \approx 6$  is sufficient to prevent co-implantation of impurity gases like nitrogen.

### 3.2.4 The photon-detection system

The photon-detection system consists of an intrinsic germanium solid-state detector (EG&G Ortec, GEM-30185-P) with a measured resolution of 1.75 keV and a relative efficiency of 33.1 % at 1.33 MeV ( $^{60}\text{Co}$ ), a Peak-to-Compton Ratio of 63:1 for  $^{60}\text{Co}$  and a measured resolution of 634 eV at 122 keV ( $^{57}\text{Co}$ ). The high voltage needed for detector operation (2500 V positive) comes from a High-Voltage Power Supply (Canberra, model 3106D).

Preamplifier pulses are fed into a fast spectroscopy main amplifier (Canberra, model 2024) connected to a 450 MHz Analog-to-Digital Converter (ADC, Canberra, model 8077) and a log/lin ratemeter (EG&G Ortec, model 449). The ADC output is accumulated in the spectrum buffer of a Canberra System 100 master board (model 4610), located in one of the slots of a 16 MHz 386DX IBM-compatible personal computer (Tandon 386/16). In most cases the spectrum contained 4096 channels (4K), although the system allowed for 16382 channels (16K). All modules are placed in a Canberra model 2100 Bin/Power Supply.

In order to improve the long-term spectrometer stability, a two-

point digital stabilizer (Canberra, model 8232) has been added, which corrects for the offset and gain of the spectrometer system. The offset is stabilized on the  $^{57}\text{Co}$  122 keV peak, while the gain is stabilized on the 511 keV peak of the annihilating positrons.

The Canberra System 100 Multi-Channel Analyser (MCA) is operated under the Windows 3.1 Operating System and programmed under Excel 4.0 in order to do automatic measurements of the  $S$ -parameter and the positronium fraction as a function of the positron energy. During the measurements the positron energy is adjusted by a program running under Excel 4.0 that sends signals to the high-voltage supply, interfaced by a Digital-to-Analog Converter (Keithley, DDA-06) in one of the slots of the personal computer.

### 3.2.5 Beam performance

#### Count rate

In the configuration described above about  $1.6 \times 10^4$  positrons reach the sample chamber per second at a positron energy of 2 keV. After annihilation about one fourth of these positrons contribute to the 511 keV peak ( $4.4 \times 10^3$ ), the remainder contributes to the Compton peak, etc. For thin samples ( $\sim 0.5$  mm) the positron count rate does not deviate much from this value, but for thicker samples, the effective count rate in the 511 keV peak region decreases significantly. Since for normal measurements about  $1 \times 10^6$  counts in the peak region suffice (see section 2.3), the measurement time is about 4 minutes for every positron energy.

When a stronger positron source was installed in the VEP in January, 1992, we have seized the opportunity to improve the beam by installing a new tungsten moderator foil and adjusting the currents through the solenoids for optimizing the count rate at the sample. After pumping the system down to  $10^{-5}$  Pa the moderator foil was subjected to several anneal cycles of 5 min. in oxygen at a pressure of  $\sim 10^{-4}$  Pa at 1500 °C followed by a 1 min. anneal at 1900 °C after pumping the oxygen, i.e. at a pressure  $\lesssim 10^{-5}$  Pa. By this procedure the carbon content of the film is reduced, leading to increased positron reemission and a narrowing of the energy spread of the reemitted

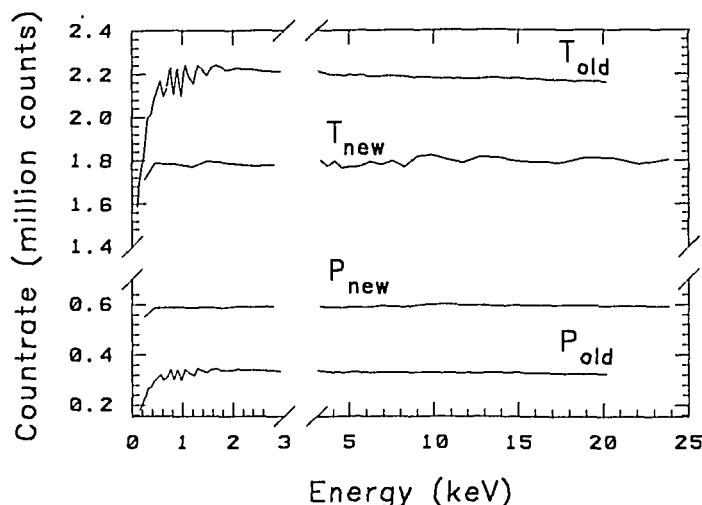


Figure 3.7: The total count rate ( $T$ ) and the 511 keV peak count rate ( $P$ ) as a function of the positron energy for the beam in its original configuration ('old') and in its new configuration ('new'). The measuring times per data point are 900 s and 300 s respectively.

positrons (Chen *et al.*, 1985; Jacobson *et al.*, 1990). After these changes the number of positrons reaching the sample was increased with a factor of 5 with respect to the configuration with the old positron source. A plot of the count rate (both in the 511 keV peak region and of the total spectrum; see section 2.3) is shown in figure 3.7.

With the new positron source, the dead time of the ADC (see section 3.2.4) amounted to  $\sim 10\%$  when the spectrum was digitized into 4096 channels,  $\sim 17\%$  for 8192 channels and  $\sim 25\%$  for 16382 channels. Therefore, in most cases the spectrum was accumulated in 4096 channels in order to retain the advantage of the high count rate, corresponding to an energy dispersion of approximately 135 eV per channel.

### Deconvolution of the Doppler-broadened 511 keV peak

Attempts have been made for deconvolution of the Doppler-broadened 511 keV annihilation peak in order to remove the instrumental dependency. When all Doppler-broadened spectra are deconvoluted following some fixed procedure, in future direct comparison of data

collected at different sites will be possible. Moreover,  $S$ -parameters derived from deconvoluted peaks are expected to be quantities that are less influenced by the configuration used for the measurements.

The deconvolutions described in this section have been carried out by implementing the algorithm of Press *et al.* (1986) in a computer program (see page 44f). After estimating the optimal filter with equation (2.25) a least-square fit of the deconvoluted signal is a simple division in Fourier space [see equation (2.22)].

The detector-resolution function (denoted by  $r(E)$  or  $R(\omega)$  in section 2.2.5) has been determined by measuring the detector signal of the 512 keV  $\gamma$ -rays of a 5  $\mu\text{Ci}$   $^{106}\text{Ru}$  source.  $^{106}\text{Ru}$  decays via  $\beta^-$  emission to  $^{106}\text{Rh}$ , which is unstable (half life of  $\sim 30$  s) and decays by emitting  $\beta^-$  and several  $\gamma$ 's, under which a 512 keV  $\gamma$  (relative intensity: 21 %). This spectrum was collected with the stabilizer disconnected, like all spectra used for deconvolution.

For deconvolution the Doppler-broadened 511 keV annihilation peak of 10 keV positrons implanted into thin polycrystalline tungsten foil which has been annealed at 1000  $^\circ\text{C}$  was chosen, for lack of a crystalline tungsten sample large enough for use in a positron-annihilation experiment. The measured spectrum, corrected for background counts, was deconvoluted and compared with 2D-ACAR spectra of crystalline tungsten [W(100) and W(010)]. The results, normalized to equal area, are shown figure 3.8.

Due to the broad detector-resolution function the deconvoluted peak is devoid of small-scale fluctuations, which are filtered out during the deconvolution process. This fine structure is visible in 2D-ACAR plots, which has a much smaller resolution function. As shown by figure 3.8 the *fwhm* of the deconvoluted Doppler peak is only slightly smaller than the *fwhm* of the 2D-ACAR spectra but the peak is much sharper. This might be due to overcorrection of the background signal at some stage in the deconvolution process. Although the polycrystalline tungsten foil may contain defects (leading to a sharper peak), the resemblance between the three peaks is remarkably well for a simple least-square deconvolution algorithm. In order to get some idea of the shape of deconvoluted peaks, figure 3.9 shows the deconvoluted curves of two Doppler-broadened 511 keV peaks, one with a low  $S$ -parameter, the other with a higher  $S$ .

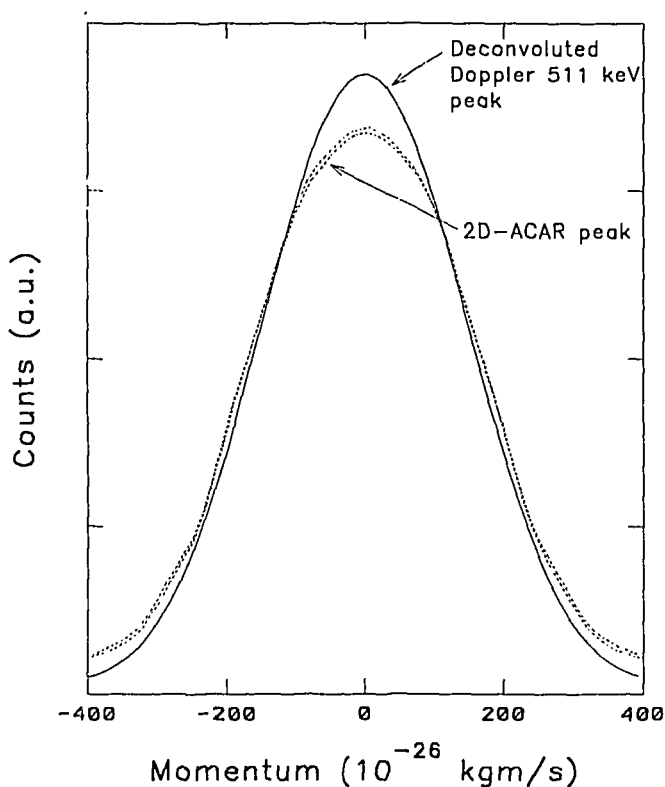
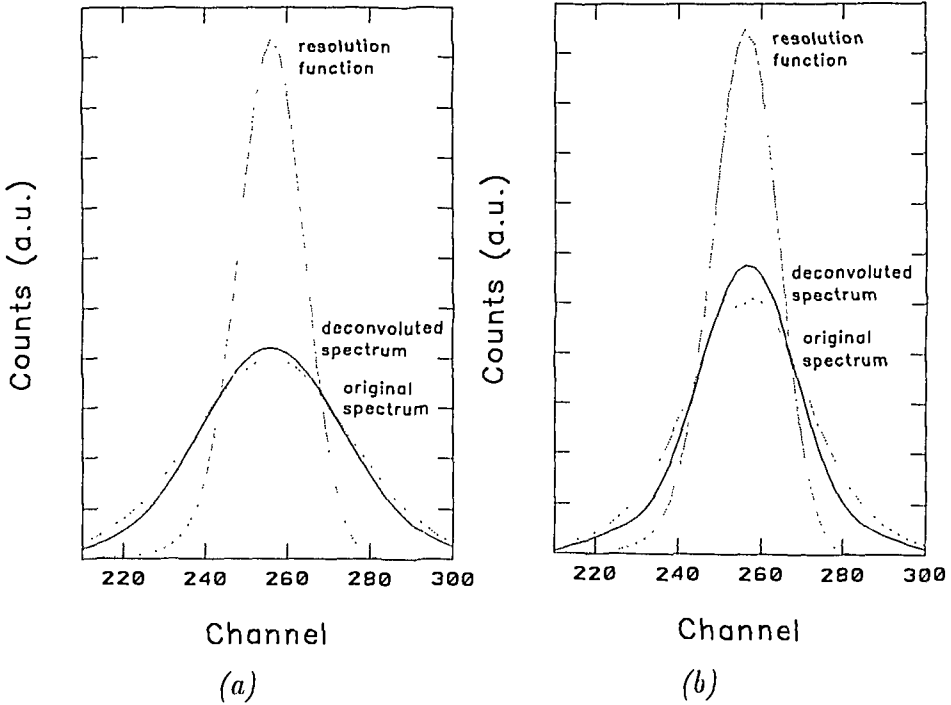


Figure 3.8: Deconvoluted 511 keV annihilation peak of polycrystalline tungsten (single curve) compared with 2D-ACAR plots crystalline W(100) and W(010) (double curves). The spectra are normalized to equal area.

In conclusion, deconvolution of the Doppler-broadened 511 keV peak is possible, but a precise knowledge of both the background noise and the instrumental resolution are essential for obtaining reliable results. The implementation of advanced deconvolution algorithms, in addition to an improved determination of the detector-resolution function and the background noise, may lead to a procedure for obtaining detector-independent Doppler-broadening spectra, which can be directly compared with similar spectra measured at other laboratories. However, it should be borne in mind that the obtained spectra are much less useful for detailed analysis than 2D-ACAR spectra due to their lack of fine structure.



*Figure 3.9:* Deconvolution of two 511 keV Doppler-broadened annihilation peaks with approximate  $S$ -parameters of 0.48 (*a.*) and 0.56 (*b.*). The resolution function and the measured 511 keV peak are dashed, while the deconvoluted curve is drawn with a solid line. The plots shown are actually annihilation peak shapes of 110 keV Rb-implanted tungsten measured for the damaged region and the deeper-lying undamaged region respectively.

### 3.3 Complementary techniques

#### 3.3.1 Free Carrier Lifetime Measurements

The Free Carrier Lifetime technique involves measurements of the reflectivity as a function of time of a plasma of optically generated free carriers in some semiconductor. The carrier lifetime depends primarily on the density of band-gap states (e.g., dangling bonds).

Carrier lifetime measurements were performed at the FOM-Institute for Atomic and Molecular Physics (Amsterdam, The Netherlands). Electron-hole plasmas were generated and probed using pulses

from a colliding pulse mode-locked laser (CPM; Fork *et al.*, 1981). The 100 fs pulses of 0.1 nJ each have an average wavelength of 620 nm and are produced at a repetition frequency of 110 MHz. The output of the CPM was split into two beams, the first (pump) was chopped at 50 kHz and focused to a 25  $\mu\text{m}$  spot, yielding an energy density of  $\sim 4 \mu\text{J}/\text{cm}^2$ . The second beam (probe) was sent through a mechanical delay line and focused to a 15  $\mu\text{m}$  spot. The energy density in the probe spot was about one tenth of that in the pump. The probe and a sample of the pump were detected by photodiodes. Using a lock-in technique, the observable reflectivity change is  $\sim 2 \times 10^{-6}$  (see further Stolk *et al.*, 1992a and 1993).

In case of a-Si the pump pulse is absorbed in the upper  $\sim 100$  nm, generating an electron-hole plasma with a peak carrier density of  $\sim 10^{18} \text{ cm}^{-3}$ . At this carrier density, the decay of the plasma is dominated by carrier trapping (Esser *et al.*, 1990), which occurs at different defect states each with a characteristic cross section  $\sigma_i$  describing the capture efficiency. If carrier capture is assumed to be ballistic, the effective decay rate  $1/\tau$  is:

$$1/\tau = v \sum_i N_i \sigma_i, \quad (3.1)$$

where  $N_i$  is the volume density of defects of type  $i$ , and  $v$  the average carrier velocity ( $\sim 10^7 \text{ cm/s}$ ). The plasma density decreases exponentially with the time constant  $\tau$ . According to a Drude model, the electron-hole plasma induces a reduction in the reflectivity which scales linearly with the plasma density (Doany *et al.*, 1987; Esser *et al.*, 1990). Hence, from exponential fits of the measured reflectivity the average carrier lifetime can be extracted, which in turn gives information about the number and character of the electrical defects present in the top layer of the sample (Stolk *et al.*, 1992a and 1993).

### 3.3.2 Raman spectroscopy

Raman scattering measurements provide a means of studying the lattice dynamics of disordered solids. From the intensity distribution of inelastically scattered light structural information about amorphous solids can be derived.

In ordered crystalline semiconductors conservation of crystal momentum causes narrow  $q \simeq 0$  phonon wavevector associated first-order Raman scattering processes. Increasing disorder which arises from, e.g., impurities or defects generally leads to a symmetric broadening of the first-order response, while loss of periodicity (local bond-angle and distance fluctuations as in amorphous materials) results in rather broad Raman spectra in which the absence of crystal momentum conservation implies the participation of all the vibrational eigenstates (Lannin, 1984).

Beeman *et al.* (1985) have done direct calculations of the Raman spectrum for different network structures of amorphous silicon. Using a Born potential to describe forces on an atomic scale, they have shown that for this material the width of the transverse-optic (TO) peak of the one-phonon Raman scattering process increases roughly linearly with  $\Delta\theta_b$ , the rms bond-angle deviation. The TO-peak width  $\Gamma$  (in  $\text{cm}^{-1}$ ) and  $\Delta\theta_b$  (in degrees) are related by:

$$\Gamma = 15 + 6 \Delta\theta_b. \quad (3.2)$$

The parameter  $\Gamma$  is defined as twice the half-width of the TO-peak on the high-frequency side at half the maximum height.

The Raman measurements were carried out at the University of Utrecht, The Netherlands. Raman scattering was performed with the 514.5 nm line of an Ar-ion laser. Spectra were taken in quasi-backscattering geometry, using a triple-grating monochromator to disperse the scattered light onto a CCD detector. The incoming laser beam was horizontally polarized, while the scattered light did not pass a polarization filter (HU-geometry). The total power at the sample was 100 mW at a focus of about  $50 \mu\text{m} \times 1.5 \text{ mm}$ .

### 3.3.3 Small Angle X-ray Scattering

With Small Angle X-ray Scattering (SAXS) large scale (i.e. large with respect to the interatomic distance) electron density fluctuations can be probed.

The SAXS experiments have been performed with the line-collimated setup at the Colorado School of Mines (Golden, Colorado, U.S.A.).

Cu  $K_\alpha$  radiation ( $\lambda = 0.154$  nm) from a Rigaku rotating-anode copper X-ray generator was selected with a crystal monochromator. The small-angle camera according to Kratky and Stabinger (Kratky, 1982) had been manufactured by Anton Paar K.G. (Graz, Austria). The scattered radiation was detected with an Ar-Xe gas-filled proportional counter with a maximum quantum efficiency of 90 % close to the energy of the Cu  $K_\alpha$  radiation. The count rate varied from  $\sim 200$  s $^{-1}$  for  $2\theta = 0.14^\circ$  to  $\sim 0.5$  s $^{-1}$  for  $2\theta = 8.4^\circ$ , leading to typical measuring times of 16 h. The setup allowed for the detection of electron-density fluctuations with sizes up to 26 nm (see Williamson *et al.*, 1989).

For voids in a material a straightforward expression for the void fraction  $v_f$  can be derived (Gerold, 1967):

$$v_f = \frac{\mu_m \rho_m}{(\Delta\rho)^2 K} \int_0^\infty h J(h) dh, \quad (3.3)$$

where  $\mu_m$  and  $\rho_m$  represent the mass absorption coefficient for Cu  $K_\alpha$  radiation in the (void-free) specimen material and the (mass) density of the (void-free) material, respectively,  $\Delta\rho$  the electron density difference in the voids from that of the surrounding bulk material,  $K$  a constant, determined by measuring  $v_f$  for a well characterized sample in some independent way (e.g., flotation analysis), and  $J(h)$  the normalized intensity as a function of the scattering vector  $h$  which has a magnitude  $h = (2\pi \sin 2\theta)/\lambda$ , where  $\lambda$  is the X-ray wavelength (see Van den Boogaard, 1992).

If the origin of  $\mathbf{x}$  is chosen in the centre of gravity of the electrons in a scattering particle with volume  $V_p$ , the radius of gyration  $R_g$  can be defined as:

$$R_g^2 = \frac{\int_{V_p} x^2 \bar{\rho}(\mathbf{x}) d\mathbf{x}}{\int_{V_p} \bar{\rho}(\mathbf{x}) d\mathbf{x}}, \quad (3.4)$$

where  $\bar{\rho}(\mathbf{x})$  is the electron density at  $\mathbf{x}$ , averaged over several atoms near  $\mathbf{x}$ . For a sphere with radius  $R$ ,  $R_g^2 = \frac{3}{5} R^2$ .

Guinier (1939) has shown that an approximation for the intensity  $j(h)$  at small scattering angles (in particular for  $hR_g \lesssim 1.2$ ) is:

$$\begin{aligned} j(h) &\propto \exp\left\{-\frac{1}{3}(hR_g)^2\right\} \\ &= 1 - \frac{1}{3}(hR_g)^2 + \dots, \end{aligned} \quad (3.5)$$

where  $j(h)$  denotes the scattering function for a single particle, averaged over all directions of  $h$  and normalized to  $j(0) = 1$ . This equation is generally referred to as Guinier's law.

Since the void fraction is proportional to  $\int_0^\infty hJ(h)dh$  [see equation (3.3)] it is appropriate to plot  $hJ(h)$  versus  $h$ .  $R_g$  can be directly derived from plots of  $\ln J(h)$  versus  $h^2$ , so-called Guinier plots [see equation (3.5)].

An extended description of SAXS-measurements and data-analysis can be found in Van den Boogaard, 1992.

### 3.3.4 Nuclear Reaction Analysis

Nuclear Reaction Analysis (NRA) is a technique based on resonant nuclear reactions, which means that the reaction can only take place for certain specific energies (Cachard and Thomas, 1978).

For neon profiling, the reaction  $^{22}\text{Ne}(p,\gamma)^{23}\text{Na}$  was used, which has been studied in detail by Meyer and Smit (1973). By counting the  $\gamma$ -rays an absolute determination of the amount of neon atoms is obtained. Neon at the surface is detected at a beam energy equalling the energy of the resonance, while neon at greater depths can be detected when the beam energy is increased. The energy loss of the incoming proton in the layer results in a nuclear reaction at this depth. This consideration, together with the value of the cross section, leads to the choice of the 851 keV resonance for neon detection.

NRA experiments on CK22 steel samples were performed at the University of Groningen, The Netherlands. The  $\gamma$ -rays were detected with a NaI detector. The energy discriminator was set to detect energies between 7 and 10 MeV. This high-energy window was necessary in order to filter out the radiation of a very strong fluorine resonance at 872 keV, which might be present on the surface due to contamination.

NEXT PAGE(S) left BLANK.

# Chapter 4

## Neon-implanted and laser-irradiated steel

### 4.1 Introduction

Over the past two decades the use of ion implantation has been promoted as a significant method of modifying the surface of materials. The improvement of the mechanical properties of ion-implanted surfaces is considerable (Dearnaley and Hartley, 1978). The major advantages of ion implantation are (Noordhuis, 1993):

- a wide variety of atoms can be implanted;
- bulk properties are not affected since ion implantation is a low temperature process;
- there are no adhesion problems since the implanted layer is bonded integrally to the substrate;
- high concentrations of insoluble atom species are easily obtained.

Commonly used ions in the field of ion-implantation metallurgy are nitrogen (N), boron (B), carbon (C), titanium (Ti), molybdenum (Mo), and chromium (Cr) [see, e.g., Dearnaley, 1990]. Implantation of neon is less commonly applied in order to improve mechanical properties like the wear resistance (Hartley, 1980). Nevertheless,

increased hardness (Hirvonen, 1978) and improved fatigue behaviour (Lyons *et al.*, 1982) have been reported. More recently it was found that implantation of neon significantly reduces the wear rate of laser-treated RCC steel, i.e. steel with 2.05 wt-% C, 11.05 wt-% Cr, and 0.62 wt-% W; De Beurs and De Hosson, 1988). In that case the inversion of the laser-induced tensile-stress state was held responsible for the improvement. Furthermore, the interaction of dislocations with the gas bubbles contributed to the wear resistance.

A similar experiment with neon-implanted laser-treated CK22 steel (0.22 wt-% C, 0.25 wt-% Si, and 0.6 wt-% Mn) does not result in an improved wear performance. The reason lies in the considerable difference between the microstructures of laser-treated RCC and CK22 steel. Firstly, CK22 steel has a dislocation density which is relatively high compared to RCC steel ( $>10^{16} \text{ m}^{-2}$  compared to  $10^{12}\text{--}10^{14} \text{ m}^{-2}$ ). Secondly, CK22 is fully martensitic while RCC is fully austenitic. Finally, the stress state is a tensile one in both cases, although the magnitude is higher for the RCC material. These differences lead to a different nucleation behaviour of neon bubbles after implantation. The maximum bubble radius is only about 5 nm for  $3 \times 10^{17} \text{ Ne/cm}^2$  in laser-treated CK22 steel, far less than the maximum radius in case of RCC steel, which amounts to 40 nm (Noordhuis, 1993). These differences explain why neon implantation is not beneficial in case of CK22 steel.

In recent years there has been some debate about the range of implanted ions in solids. Topics involved in this discussion are: sputtering, channelling, and stress-enhanced diffusion. Moreover, diffusion along dislocation lines might influence the resultant implantation profile.

Studies of neon-implanted laser-treated RCC steel revealed an average implantation depth of 80 nm. This value, obtained from Transmission Electron Microscopy (TEM) measurements, is approximately twice the one calculated with the TRIM program (Ziegler *et al.*, 1985). Channelling and the enhanced diffusion were given as an explanation for this large implantation depth (De Beurs, 1988).

In the recent past low-energy positrons have been utilized for studying ion-implanted materials, mainly inert-gas-implanted metals. These investigations yielded evidence for lattice damage well beyond

the range of implantation, e.g., in case of neon-implanted copper single crystals (Brusa *et al.*, 1989), krypton-implanted polycrystalline titanium (Smith *et al.*, 1990a), helium-implanted polycrystalline copper and nickel (Uedono *et al.*, 1991a), carbon-implanted 316 stainless-steel (Aruga *et al.*, 1992) and, recently, rubidium-implanted polycrystalline tungsten (Schut *et al.*, 1992). Evidence of this damage tail was also found by Gerritsen (1990) utilizing cross-sectional TEM.

In this chapter results are presented of positron-annihilation measurements in which the formation of a damage tail in annealed Fe-C steel (CK22) samples and laser-treated Fe-C samples is compared. Special attention was paid to the development of this tail during annealing, in order to establish the nature of these defects. Fe-C steel was chosen because the microstructure is heavily affected by laser melting with respect to dislocation density and carbon in solid solution. Furthermore, Nuclear Reaction Analysis (NRA) was carried out in order to measure the actual neon distribution in both types of samples.

## 4.2 Sample preparation

The samples for the positron-annihilation experiments were made of CK22-steel, of which the exact composition has been given above. In total four samples were studied. Two samples were laser treated, while neon was implanted into one of the laser-treated samples and into one of the non laser-treated samples.

The laser treatment was carried out with a continuous wave CO<sub>2</sub> laser, located at the University of Groningen, The Netherlands. This transverse-flow Spectra Physics 820 laser operates in a TEM<sub>00</sub> mode, which means that the beam shape is nearly gaussian. The wavelength of the CO<sub>2</sub> laser is 10.6  $\mu\text{m}$ . The laser beam, 19 mm in diameter, was focused using a water-cooled 127 mm ZnSe lens with its focal point 5 mm above the surface, i.e. yielding a spot diameter of 0.75 mm. The scan velocity was 15 cm/s, while adjacent tracks were made with a 40% overlap with one another. The power was 1300 W, corresponding to a power density at the surface of  $3 \times 10^5 \text{ W/cm}^2$ . All irradiations were done in an argon atmosphere to protect the lens as

well as to prevent oxidation of the sample. Besides, during irradiation the samples were placed on a water-cooled copper block in order to prevent bulk heating of the sample.

The non laser-treated samples were mechanically polished and subsequently annealed at 450 °C for 3 hours (these samples will be referred to below as the 'annealed samples'). The other samples were sandblasted with irregularly shaped Al<sub>2</sub>O<sub>3</sub> particles, approximately 50 µm in diameter, in order to increase the absorption for the laser irradiation. This yielded a surface roughness of the same dimension as the wavelength of the laser light. The expected absorption coefficient for iron-based alloys was 30 %.

After annealing or laser treating, the samples were implanted with 50 keV <sup>20</sup>Ne. The implantation was carried out using an Extrion 200 keV–200 µA machine, while the current density during implantation was so low that the sample temperature was kept well below 150 °C. The samples used for NRA experiments were implanted with <sup>22</sup>Ne. The dose was 2×10<sup>17</sup> cm<sup>-2</sup>, i.e. a dose just below the critical dose for blistering.

The main effect of the laser surface melting of CK22 steel is a large deformation, which has two causes:

- *the martensitic transformation:* During the rapid cooling process the austenitic phase transforms to a martensitic one in a diffusionless way. This transformation is accompanied by the so-called Bain deformation resulting in large lattice strains (see, e.g., Porter and Easterling, 1981). These, in turn, are relieved by dislocation glide in the case of low-carbon steels like CK22. The result is a lath martensite with a high dislocation density.
- *thermally induced deformation:* Due to the only local melting of the substrate surface at laser irradiation, large thermal strains arise during heating and cooling. The samples are covered with overlapping laser tracks, so that every part of the surface runs through a thermal cycle more than once.

TEM micrographs of laser-irradiated CK22 steel indicate dislocation densities higher than 10<sup>16</sup> m<sup>-2</sup>. In order to further quantify the dislocation density, the sample was investigated with X-ray diffraction

Table 4.1: Dislocation densities  $\rho$  obtained from the measured microstrain  $\epsilon$  and the particle size  $D$  as obtained from X-ray measurements of laser-irradiated CK22 steel and shot-peened and laser-irradiated pure iron.

	$D$	$\epsilon$	$\rho$
laser-treated CK22	26.8 nm	0.198 %	$8.9 \times 10^{16} \text{ m}^{-2}$
shot-peened pure Fe	254.2 nm	0.041 %	$1.9 \times 10^{15} \text{ m}^{-2}$
laser-treated pure Fe	137.4 nm	0.033 %	$2.9 \times 10^{15} \text{ m}^{-2}$

line-profile analysis, the Fourier single-line method being carried out on the  $\langle 110 \rangle$  reflection. An annealed pure iron (Fe) sample was used as a reference in order to eliminate the instrumental broadening. The measured microstrain and particle size can be converted to a dislocation density by following the procedures proposed by Williamson and Smallman (1956). The microstrain  $\epsilon$  and the particle size  $D$  (obtained from the measured peak widths and shapes of the reflections) are related to a density of dislocations  $\rho$  by (Mikkola and Cohen, 1966):

$$\rho = 2\sqrt{3} \frac{\sqrt{\langle \epsilon^2 \rangle}}{Db}, \quad (4.1)$$

where  $b$  is the magnitude of the Burgers vector. The results are shown in table 4.1. Measurements of dislocation densities of laser-treated pure iron yielded values of one order of magnitude smaller. This, in fact, illustrates why an experiment in which an extremely high dislocation density is required, cannot be performed on laser-treated samples of pure iron.

All samples have been measured in their *as-implanted/annealed* state and after 30 min. anneals at elevated temperatures, ranging between 100°C and 750°C (for the temperatures, see figure 4.2).

Nuclear Reaction Analysis (NRA; see section 3.3.4) has been carried out on the  $^{22}\text{Ne}$ -implanted samples in order to acquire direct information of the neon distribution.

### 4.3 Channelling

Since the neon distribution can be influenced by channelling effects, it is important to know the channelling probability of both protons (utilized in the NRA measurements) and neon in the studied material.

The critical angles  $\psi$  (in degrees) for channelling of 50 keV  $^{22}\text{Ne}$  and 851 keV protons follow from the following expressions for axial channelling (Gommel, 1974; Gerritsen, 1990):

$$\psi_{\text{axial}} = 2.61 \sqrt[4]{\frac{Z_1 Z_2 a^2}{d^3 E}}, \quad (4.2)$$

and for planar channelling:

$$\psi_{\text{planar}} = 0.172 \sqrt{\frac{N Z_1 Z_2 a}{E}}, \quad (4.3)$$

where  $Z_1$  and  $Z_2$  are the nuclear charges of the moving ion and the target ion,  $N$  the planar atomic density ( $\text{nm}^{-2}$ ),  $E$  the initial energy of the implanted ion (in MeV),  $d$  the atomic spacing along the lattice row (in nm) and  $a$  the Firsov screening length (also in nm), given by:

$$a = \frac{0.04685}{[\sqrt{Z_1} + \sqrt{Z_2}]^{2/3}}. \quad (4.4)$$

It follows from equations (4.2) and (4.3) that the channelling of protons can be neglected compared to the channelling of neon atoms. As a result, NRA experiments should be capable of detecting any channelling of neon.

In case of neon channelling calculations also show, by averaging over some directions, that axial channelling will occur more easily in a *bcc* crystal (e.g., the austenitic phase), whereas planar channelling occurs more easily in an *fcc* crystal (e.g., the martensitic phase). However, the difference amounts only to a factor of 2 and will therefore not be very important. Since our samples are polycrystalline, planar channelling is likely to dominate over axial channelling.

Dechannelling events may occur when a channelling neon atom encounters a defect like a dislocation, an interstitial carbon atom, a

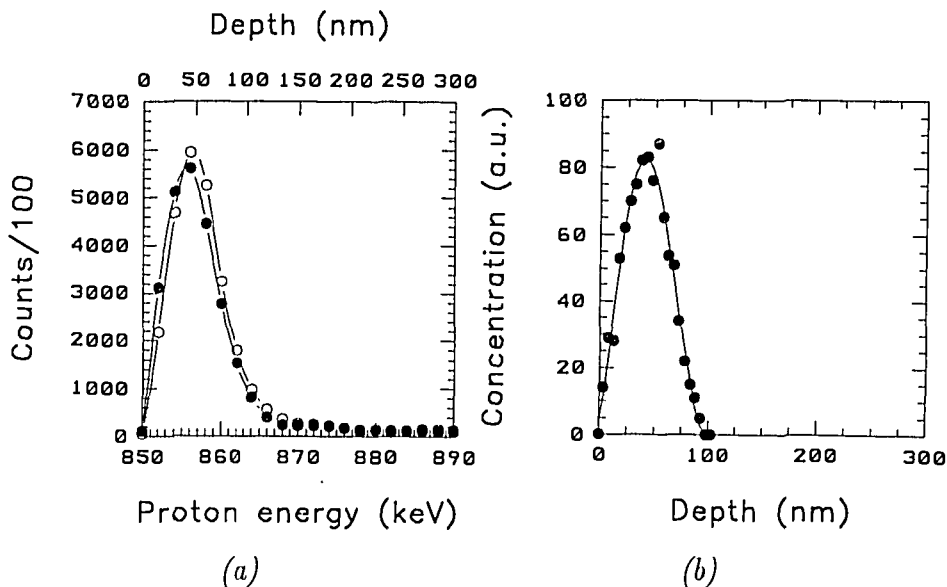


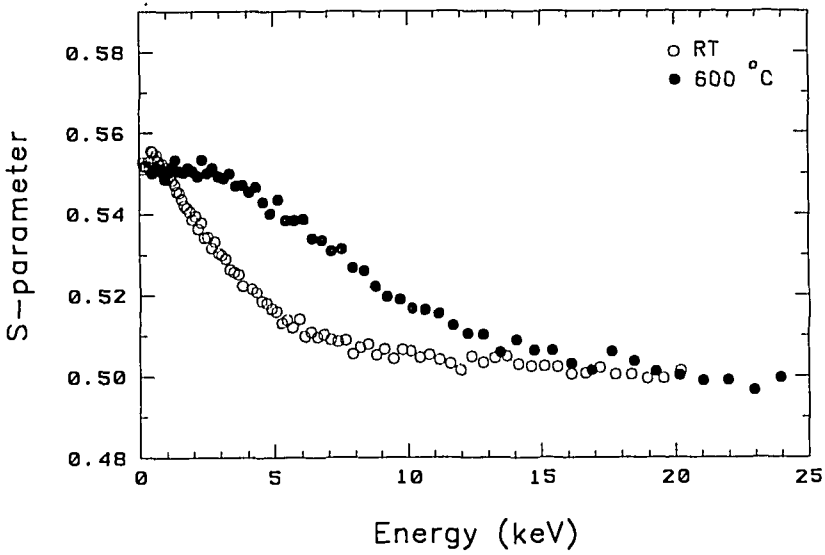
Figure 4.1: *a.* Depth profile of  $^{22}\text{Ne}$  in laser-treated (●) and annealed (○) CK22 steel as measured by NRA; *b.* TRIM profile of  $^{22}\text{Ne}$  in (amorphous) Fe.

neon bubble or a self-interstitial. The former two defects are induced by the laser treatment, while the latter two defect types are caused by the neon implantation.

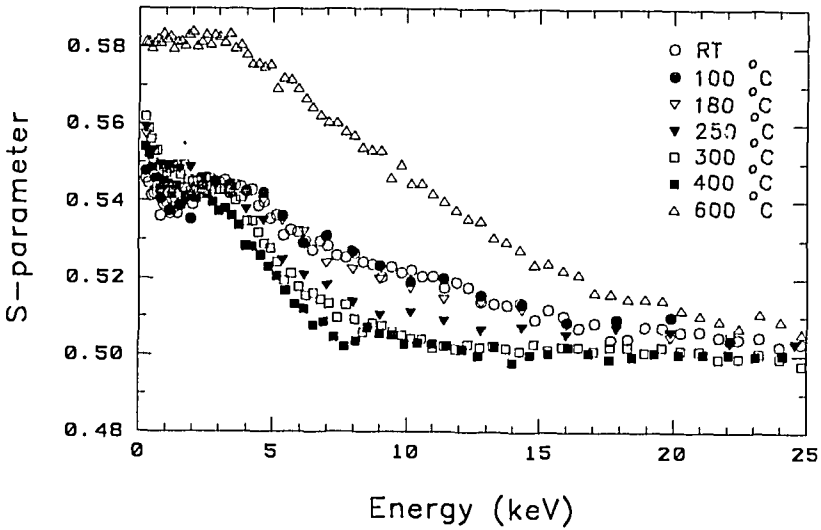
In the annealed samples the dislocation density is low and most carbon is present in the form of large cementite plates. In this case, channelling will only be reduced by the implantation-induced damage. In the laser-treated samples all of the carbon is dissolved and occupies octahedral sites. Furthermore, the dislocation density in the laser-treated samples is high. Since the critical angle for planar channelling is small, due to the high dislocation density a large reduction in the channelled fraction is to be expected.

## 4.4 Results

The depth profiles of  $^{22}\text{Ne}$  in laser-treated and annealed CK22 steel as measured by NRA are shown in figure 4.1*a*, while figure 4.1*b* shows the neon depth profile calculated by TRIM. The results of

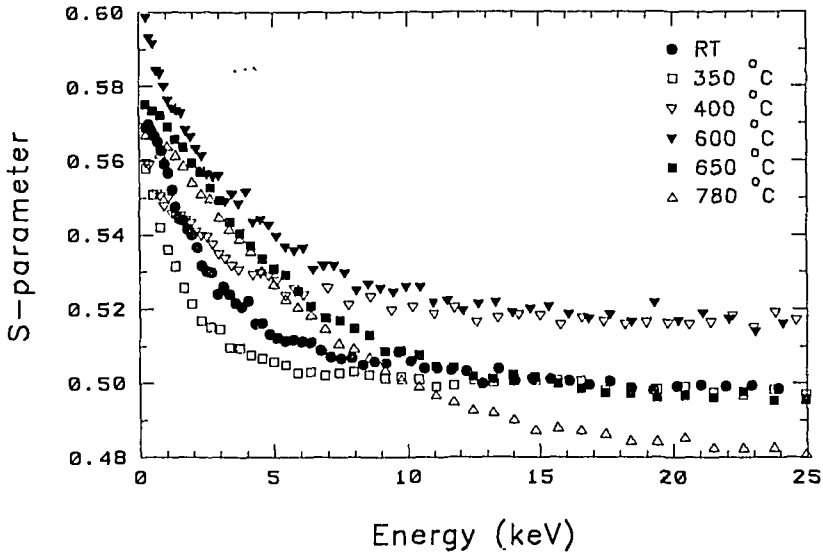


(a)

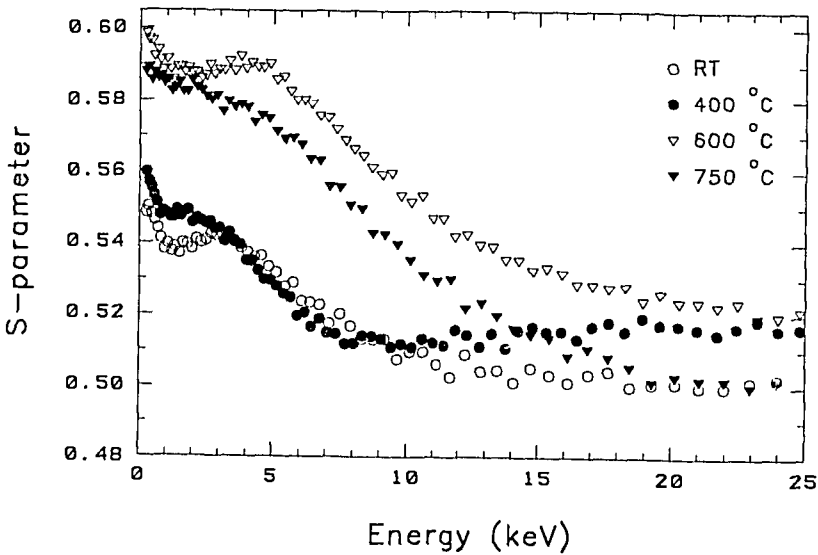


(c)

Figure 4.2: *S*-parameter vs. positron incident energy of CK22 steel, measured in its original state and after 30 min. anneals at the indicated temperatures. *a.* annealed; *c.* annealed and 50 keV neon implantation.



(b)



(d)

Figure 4.2 (continued): b. laser irradiated; d. laser irradiated and 50 keV neon implantation.

the positron-annihilation  $S$ -parameter measurements are shown in figure 4.2. TEM micrographs of neon-implanted CK22 steel after several 30 min. *in-situ* annealing steps are depicted in figure 4.3.

The positron-annihilation measurements reveal two zones with defects:

- *zone 1*: In both the annealed and laser-treated sample (see figure 4.2c and d) a high concentration of defects centered around the mean implantation depth of the neon ( $\sim 50$  nm, corresponding to a positron energy of  $\sim 3$  keV) is visible. The approximately gaussian profile can be identified with the defect distribution caused by the neon implantation. The defects in this zone remain unaffected up to temperatures of  $400^\circ\text{C}$ . After an anneal above this temperature these defects appear to have been changed into defects that yield a very high  $S$ -value, presumably large open-volume defects.
- *zone 2*: Only in the annealed sample (see figure 4.2c), beyond zone 1, at depths up to 10 times the mean implantation depth, a zone with a lower defect concentration is visible (i.e. at a depth  $> 100$  nm, corresponding with positron energies of 5–10 keV). The majority of the defects in this zone disappear (or reduce to a size where they yield  $S$ -values indistinguishable from the  $S$ -parameter of the bulk) after annealing at  $250^\circ\text{C}$ . At some temperature above  $400^\circ\text{C}$  these defects reappear again.

Additionally, there is a bulk effect in the laser-irradiated sample (see figure 4.2b). After an anneal at  $400^\circ\text{C}$  the  $S$ -value of the bulk has increased, but after an anneal at  $650^\circ\text{C}$  the  $S$ -parameter is back at its original value, whereas an anneal at  $780^\circ\text{C}$  leads to an  $S$ -value far below its original value.

The TEM micrographs of the implanted samples show the presence of neon bubbles which can be identified with the high  $S$ -value defects in the first zone. The *in-situ* annealing experiments show that the observed increase in  $S$  in figure 4.2c coincides with an increase in the bubble size.

The NRA experiments reveal a neon distribution that is similar for the annealed and the laser-treated samples. The small shift of the profile towards the surface in the case of laser-treated material is too

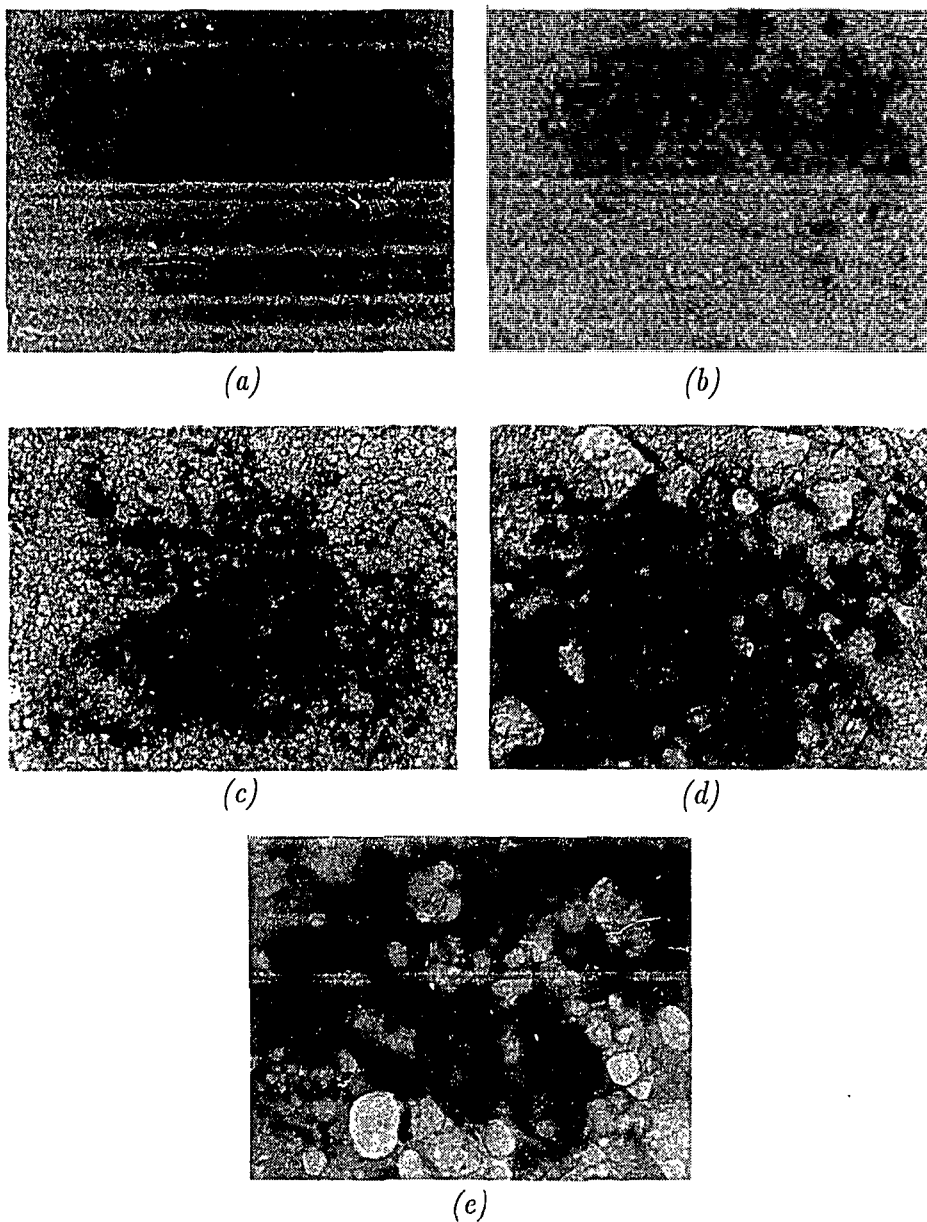


Figure 4.3: TEM micrographs of neon-implanted CK22 steel at room temperature (a), and after 30 min. annealing steps at 250 °C (b), 400 °C (c), 500 °C (d), and 600 °C (e).

small to be significant and is probably due to a slight instability of the Van de Graaff generator. The total number of counts in the tail is approximately 10 % higher in the annealed sample than in the laser-treated sample, but this percentage amounts to only 1 % of the total number of counts. Therefore, we can conclude that NRA experiments did not detect any significant fraction of channelled ions within its experimental resolution limit.

In the unimplanted annealed and laser-irradiated samples the large increase of the  $S$ -parameter after an anneal at higher temperatures was absent (see figure 4.2*a* and *b*). The high dislocation density in the laser-treated sample did not result in a significant change of the annihilation characteristics. In the neon-implanted laser-treated sample no damage in the second zone was observed (see figure 4.2*d*).

## 4.5 Discussion

### 4.5.1 Interpretation of the data

When NRA and positron-annihilation measurements are compared, it must be concluded that positron annihilation is much more sensitive to the low concentration of defects at depths above 100 nm (i.e. zone 2). The high concentration of defects in zone 1 is clearly visible with both techniques.

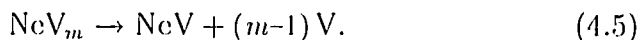
#### A. Zone 2 defects up to 400 °C

A 'tail' of damage distribution has been reported by several authors who employed positron-beam analysis to study the damage profile of implanted ions in metals. Brusa *et al.* (1989) reported 'deep disorder' in 30–100 keV neon-implanted copper ( $10^{15} \text{ cm}^{-2}$ ), which they ascribed to dislocation loops formed by aggregation at a large depth of self-interstitial atoms during bombardment. Smith *et al.* (1990a), who reported positron trapping well beyond the implantation range of 100 keV krypton in titanium at a dose of  $1.5 \times 10^{16} \text{ cm}^{-2}$ , assume deeply knocked-in krypton atoms in order to be able to explain their data. This deep damage could be removed by annealing at 400 °C. Aruga *et al.* (1992), who observed the defect depth profile of carbon

implanted into stainless steel to be about twice as deep as predicted from TRIM calculations, suggested two possible explanations. Either "vacancies migrate to larger depths along the steep gradient of the distribution of radiation-produced point defects", or TRIM underestimates the nonlinear collisional effects resulting in a larger energy transfer into the deeper regions of the sample.

In order to explain the deep damage of zone 2, we propose that a part of the neon atoms reaches larger depths by channelling during implantation in the annealed material (grain size  $> 1 \mu\text{m}$ ). This is in agreement with Gerritsen *et al.* (1989), who concluded from their experiments that ion channelling is inevitable in case of ion implantation in crystalline materials. At the end of the range small  $\text{NeV}_m$  ( $m > 1$ ) complexes are formed. These defects may either originate from the 'end-of-the-range damage' (compare Bolse, 1992) or from low-energy transfers during the channelling.

The excess vacancies dissociate at  $250^\circ\text{C}$  rendering the neon atoms in substitutional sites:



Desorption studies on keV-implanted argon in molybdenum and Mössbauer spectroscopy and Perturbed Angular Correlation measurements on indium-implanted nickel give evidence for this defect reaction (Hohenemser *et al.*, 1977; De Waard *et al.*, 1981; Van Veen *et al.*, 1982).

Substitutional neon (NeV) is virtually invisible in positron-annihilation experiments, since the  $S$ -value reduces to a near bulk value due to the absence of much open volume. This explains the disappearance of the damage tail after an anneal at  $250^\circ\text{C}$ . The laser-treated material has a substructure consisting of a very high dislocation density, which may have prevented the neon atoms from reaching large depths, e.g., by dechannelling events occurring at the dislocations or by stress effects. An alternative explanation may be the presence of dissolved interstitial carbon atoms blocking the channelling.

The recovery stage we observe at  $400^\circ\text{C}$  for the deep defects (zone 2) corresponds well with the main recovery stage reported in bulk-damaged nickel by Dlubek *et al.* (1979). They observe vacancy

clustering and void growth at this temperature. Beasley *et al.* (1987) also report vacancy-clustering at this temperature in quenched nickel.

### B. Zone 1 and 2 defects from 400 °C

After annealing at 600 °C sufficient thermal vacancies become available for the bubbles in zone 1 to reach thermal equilibrium. The TEM micrographs show that coalescence occurs (figure 4.3), which leads to an increase in the open volume and hence a higher  $S$ -value. At this temperature the substitutional neon in zone 2 starts to diffuse, assisted by the vacancies, and also forms small neon agglomerates. This causes an increase of the  $S$ -parameter also at depths corresponding with zone 2. Uedono *et al.* (1990) have likewise observed a drastic increase of the Doppler parameter upon annealing at 600 °C of JPCA stainless steel implanted with 70 keV helium to a dose of  $10^{16} \text{ cm}^{-2}$ .

This interpretation is in agreement with the results of Amarendra *et al.* (1991), who reported helium bubble growth starting at 300 °C in 0.5 MeV alpha-irradiated copper. Jensen *et al.* (1988b) observed an increase of the longest lifetime in copper and nickel containing 3 and 5 % krypton respectively, during annealing. The lifetime started to go up at a temperature around 300 °C in the former and around 430 °C in the latter case, which the authors ascribed to krypton bubble growth. For the mechanism of vacancy generation they suggested at lower temperatures loop punching, while at higher temperatures (at a temperature of approximately half the melting point) the concentration of thermal vacancies should be high enough for equilibrium bubbles to be established. Lower krypton concentrations in the bubbles corresponded to a longer positron lifetime. Since positrons trap at the cavity surfaces, i.e. at the krypton-metal interface (Jensen *et al.*, 1990), a lower inert gas concentration in the bubble results in a reduced contribution of core-electron annihilations and therefore a higher  $S$ -parameter.

The increase of the  $S$ -parameter in zone 1 of the neon-implanted laser-treated sample is similar to that in the neon-implanted annealed sample (see figures 4.2c and d). It is caused by the coalescence of the bubbles.

### C. Defects not related to the neon implantation

Annealing of the annealed sample at 600 °C leads to a higher  $S$ -parameter in the surface region (figure 4.2a), but this effect is probably due to diffusion of impurities from the (rather bad) vacuum into the sample during heating.

Annealing of both laser-treated samples shows yet another effect (figures 4.2b and d). Annealing at 400 °C results in an increased  $S$ -value of the bulk material. This increment is visible in both the implanted and the unimplanted sample and, therefore, cannot have anything to do with channelled neon atoms. Most likely these defects must be identified with clustering of the quenched-in vacancies that are present after the rapid cooling caused by the laser treatment. Self-interstitials or self-interstitial clusters are not very likely to appear at 400 °C because during heating vacancies are much more likely to be formed than interstitials (which have a higher formation energy).

This explanation corresponds well with the experiments of Lopes Gil *et al.* (1992), who studied laser-surface-melted pure nickel samples. Small vacancy clusters quenched-in during the fast cooling process were found at greater depths, although they were not present in the first 1  $\mu\text{m}$ , which the authors ascribe to “the pumping effect of the surface”. An increase in both the lifetime and the Doppler parameter gave evidence of a clustering of these vacancies after an anneal at 300 °C.

At 600 °C these vacancy clusters (or voids) have disappeared, as shown by the decrease of the  $S$ -parameter (see figures 4.2b and d). At this temperature the diffusion of vacancies is so rapid that a large number of them are lost through the sample surface. As a consequence, the vacancy clusters shrink, leading to a lowering of the  $S$ -value, which has even decreased below the bulk value after an anneal at 780 °C.

#### 4.5.2 Estimates for the defect concentrations

The positron-annihilation measurements of figure 4.2 have been analysed with the computer code VEPFIT. The fit results for the annealed sample, the laser-treated sample, the annealed ion-implanted sample

*Table 4.2:* Fit results of the positron-annihilation measurements on annealed CK22 steel at room temperature (RT) and after an anneal at 600 °C. A 3-layer model was used with the layer boundaries fixed at 30 and 300 nm. The diffusion length in layer 3 ( $L_3$ ) was fixed at 68 nm. Relative errors in the values of  $L$  are 10 %.

	$S_1$	$S_2$	$S_3$	$L_1$	$L_2$
RT	0.5282 (24)	0.5039 (3)	0.4995 (5)	34.2 nm	31.4 nm
600 °C	0.5656 (13)	0.5335 (32)	0.4962 (4)	23.5 nm	59.8 nm

*Table 4.3:* Fit results of the positron-annihilation measurements on laser-treated CK22 steel at room temperature (RT) and after anneals at several temperatures. A 3-layer model was used with the layer boundaries fixed at 30 and 300 nm. The diffusion length in layer 3 ( $L_3$ ) was fixed at 68 nm. Relative errors in the values of  $L$  are 10 %.

	$S_1$	$S_2$	$S_3$	$L_1$	$L_2$
RT	0.5184 (7)	0.5043 (3)	0.4975 (4)	13.4 nm	32.7 nm
350 °C	0.5144 (6)	0.5013 (3)	0.4974 (4)	6.4 nm	15.9 nm
400 °C	0.5400 (4)	0.5200 (4)	0.5157 (4)	5.1 nm	24.5 nm
600 °C	0.5584 (4)	0.5210 (4)	0.5160 (4)	6.6 nm	48.1 nm
650 °C	0.5517 (14)	0.5022 (5)	0.4942 (4)	18.7 nm	59.7 nm
780 °C	0.5514 (13)	0.4939 (6)	0.4796 (4)	18.3 nm	69.8 nm

and the laser-treated ion-implanted sample are presented in tables 4.2, 4.3, 4.4, and 4.5, respectively.

The fitted values for  $S_3$ ,  $S_4$  and  $L_4$  (i.e. the  $S$ -parameter of layers 3 and 4 and the diffusion length in layer 4) of both neon-implanted samples as a function of the anneal temperature are graphically depicted in figure 4.4. From this figure it is clear that the damage tail in neon-implanted annealed CK22 steel leads to a higher  $S$ -parameter and a lower diffusion length in depth-region 4 (60–300 nm) as compared with the neon-implanted laser-treated sample.

Estimates for the defect concentration can be derived from equations (2.6) and (2.8) on the assumption that there is only one type of defect present. The effective diffusion length and the diffusion length

Table 4.4: Fit results of the positron-annihilation measurements on annealed CK22 steel implanted with 50 keV neon at room temperature (RT) and after anneals at several temperatures. A 5-layer model was used with the layer boundaries fixed at 2, 20, 60, and 300 nm. Furthermore, several  $S$ -values and diffusion lengths ( $L$ ) were fixed:  $S_1=0.5100$ ,  $S_5=0.5015$ ,  $L_1=4.0$  nm,  $L_3=0.01$  nm and  $L_5=68$  nm. Relative errors in  $L$ -values are 10 %.

	$S_2$	$S_3$	$S_4$	$L_2$	$L_4$
RT	0.4958 (43)	0.5472 (4)	0.5203 (3)	15.0 nm	14.7 nm
100 °C	0.4731 (68)	0.5480 (7)	0.5211 (5)	15.0 nm	18.5 nm
180 °C	0.4893 (64)	0.5460 (6)	0.5162 (6)	14.8 nm	27.4 nm
250 °C	0.5303 (66)	0.5459 (7)	0.5086 (5)	14.8 nm	7.6 nm
300 °C	0.5181 (42)	0.5449 (4)	0.4998 (3)	14.9 nm	12.2 nm
400 °C	0.5088 (51)	0.5409 (5)	0.4987 (3)	15.5 nm	3.5 nm
600 °C	0.5956 (42)	0.5821 (4)	0.5490 (4)	15.0 nm	34.3 nm

in defect-free material are related by:

$$\left( \frac{L_{+,eff}}{L_+} \right)^2 = \frac{\lambda_b}{\lambda_b + \kappa_t}, \quad (4.6)$$

with  $\kappa_t$  as defined in equation (2.9). The defect concentration  $n_t$  may now be estimated by:

$$n_t = \frac{\lambda_b}{\nu_t} \left[ \left( \frac{L_+}{L_{+,eff}} \right)^2 - 1 \right]. \quad (4.7)$$

The specific trapping rate for monovacancies in iron has been evaluated by lifetime measurements to be about  $1.1 \times 10^{15} \text{ s}^{-1}$  (Vehanen *et al.*, 1982), while theoretical calculations have shown that, for small clusters, the trapping rate scales linearly with the number of vacancies in the cluster (Nieminen and Laakkonen, 1979). Assuming a positron diffusion length in defect-free CK22 steel of 68.0 nm (earlier experiments yielded this value for both annealed and laser-treated steel), the defect concentration in some of the regions of the samples can be estimated, expressed in the equivalent number of monovacancy trapping sites.

*Table 4.5:* Fit results of the positron-annihilation measurements on laser-treated CK22 steel implanted with 50 keV neon at room temperature (RT) and after anneals at several temperatures. A 5-layer model was used with the layer boundaries fixed at 2, 20, 60, and 300 nm. Furthermore, several  $S$ -values and diffusion lengths ( $L$ ) were fixed:  $S_1=0.5100$ ,  $L_1=4.0$  nm,  $L_3=0.01$  nm and  $L_5=68$  nm. Relative errors in  $L$ -values are 10 %, errors in  $S$  about 0.0010.

	$S_2$	$S_3$	$S_4$	$S_5$	$L_2$	$L_4$
RT	0.5136	0.5440	0.5024	0.4996	9.9 nm	39.4 nm
400 °C	0.5481	0.5425	0.5065	0.5195	0.5 nm	12.8 nm
600 °C	0.5704	0.5921	0.5024	0.5166	9.7 nm	60.0 nm
750 °C	0.6191	0.5797	0.5194	0.4952	24.8 nm	62.3 nm

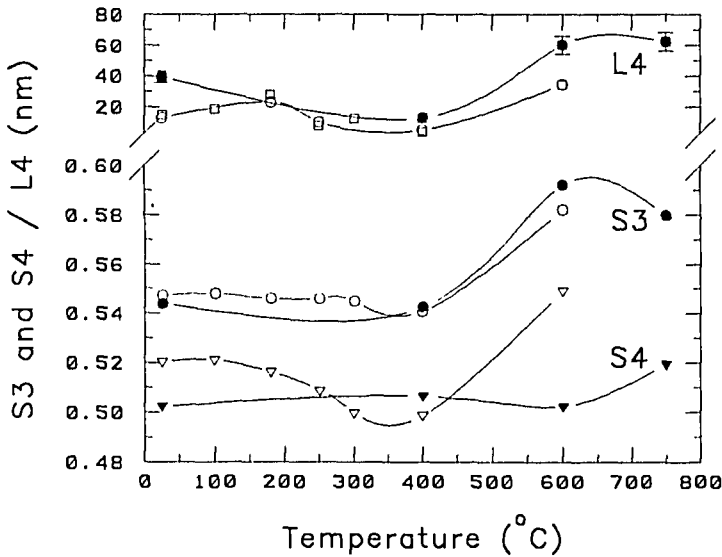


*Figure 4.4:* The fitted values (from tables 4.4 and 4.5) for  $S_3$  (○),  $S_4$  (▽) and  $L_4$  (□) of the laser-treated (filled symbols) and the annealed (hollow symbols) neon-implanted samples as a function of the anneal temperature. The lines are to guide the eye.

Taking for the free-positron annihilation rate in CK22 steel the value for pure iron ( $\lambda = 9.4 \times 10^9 \text{ s}^{-1}$ ; Barbiellini *et al.*, 1991), the room-temperature value of  $L_4$  (the diffusion length in the region from 60–300 nm) in case of laser-treated neon-implanted steel (39.4 nm) corresponds with a vacancy concentration of  $1.7 \times 10^{-5}$ , while this value for annealed neon-implanted steel (14.7 nm) yields a vacancy concentration of  $1.7 \times 10^{-4}$ . These concentrations may serve as estimates for the defect concentrations in the ‘tail’-region. They are indeed too low for detection by NRA.

The size of the neon bubbles is related to the value of the  $S$ -parameter in the bubble region (zone 1) of the neon-implanted samples (S3) which amounts to  $\sim 0.546$ . This value corresponds to a (normalized)  $S$  of 1.092 after scaling to the bulk  $S$ -parameter [ $\sim 0.500$ ; compare equation (2.16)]. As a reference, divacancies in silicon give an  $S$  of about 1.035 (Simpson *et al.*, 1990), while micro-cavities in metals yield  $S$ -values of  $\sim 1.15\%$  (see, e.g., Schut *et al.*, 1992). The low  $S$  can be explained by the ‘passivation’ of the traps by the neon atoms filling the free space. The very high  $S$ -value of  $\sim 0.59$ , i.e.  $S \approx 1.18$  points to large bubbles with a low neon-gas density (equilibrium value; Eldrup, 1992), in agreement with the large voids visible in the TEM micrographs (see figure 4.3).

The concentration of quenched-in vacancies in the laser-treated sample can be deduced from the fitted diffusion length in region 2 (30–300 nm), which amounts to 24.5 nm after the anneal at 400 °C. Equation (4.7) [see page S5] now gives an estimated vacancy concentration of  $5.7 \times 10^{-5}$ .

## 4.6 Conclusions

Positron-annihilation  $S$ -parameter measurements have been performed on annealed and laser-treated 0.22 wt-% carbon steel that has been implanted with 50 keV neon to a dose of  $2 \times 10^{17} \text{ cm}^{-2}$ , in addition to TEM, NRA and X-ray diffraction experiments.

In the non laser-treated samples due to the implanted neon, damage is observed at depths up to 10 times the mean implantation range. This defect ‘tail’ is absent in the neon-implanted laser-treated

samples. The data has been explained by assuming channelling of the neon to greater depths in case of (poly-)crystalline sample material. At the end of the range small  $\text{NeV}_m$  ( $m > 1$ ) complexes are formed. The excess vacancies dissociate at 250 °C rendering the neon atoms in substitutional sites, resulting in a lowering of the  $S$ -parameter.

At even higher temperatures (600 °C) the  $S$ -parameter related to the neon profile increases dramatically, which has been explained by bubble growth caused by coalescence of bubbles and accumulation of thermal vacancies. At this temperature the deep neon starts to diffuse and also forms small neon agglomerates leading to an increase in the  $S$ -parameter.

Annealing of a non-implanted laser-treated sample at 400 °C shows an increase of the  $S$ -parameter, which is probably due to clustering of quenched-in vacancies. These vacancy clusters are annealed out at 600 °C.

# Chapter 5

## Helium and hydrogen-implanted silicon

### 5.1 Introduction

*Ion implantation in silicon*, either at a high dose in order to amorphize the sample material (see, e.g., Rai *et al.*, 1987; Elliman *et al.*, 1988; Linnros *et al.*, 1988; Tamura and Suzuki, 1989), or at a low dose, e.g., in order to passivate the dopants, has drawn much attention in recent years (Pankove *et al.*, 1983; Pantelides, 1987; Pankove, 1992). One area of interest is the nature of the defects generated by the implantation process. Although ion-implantation is a useful method of introducing impurity atoms into materials in a controlled manner, the process invariably results in damage and ultimately amorphous zones.

In crystalline silicon, hydrogen is known to have a role of saturating broken chemical bonds, thereby passivating these electrical defects (DeLco *et al.*, 1984; Müller, 1988; Pankove, 1992). In recent years it was discovered that hydrogen in silicon is also capable of passivating shallow-level and deep-level defects (Pearson, 1986; Pearson *et al.*, 1987; Estreicher *et al.*, 1989). In *p*-type Si, hydrogen is found to passivate shallow-acceptor impurities causing a dramatic increase in the resistivity of the samples (Pankove *et al.*, 1983; Sah *et al.*, 1983; Huang *et al.*, 1992), while passivation of shallow-donor impurities

has also been observed in *n*-type Si (Johnson *et al.*, 1986; Bergman *et al.*, 1988). In addition to passivating the existing defects, hydrogen can induce microdefects and electronic deep levels in silicon (Johnson *et al.*, 1987; Boyce *et al.*, 1992). For reviews, see Johnson *et al.* (1991) and Pankove (1992).

Inert-gas impurities in silicon are also of great interest because they are used for sputtering, ion etching and gettering. The existence of inert-gas atoms in a semiconductor, often due to the above-mentioned processes or irradiation damage, can change the electrical properties of the material. On the other hand, there is much fundamental interest concerning, e.g., the interaction of inert-gas atoms with the host semiconductor and the diffusion process, while only few theoretical or experimental studies of these systems are available (Van Wieringen and Warmoltz, 1956; Van Veen *et al.*, 1988; Karavaev *et al.*, 1990; S. Mäkinen *et al.*, 1991; Alatalo *et al.*, 1992). Recently, Griffioen *et al.* (1987) have shown that stable voids in silicon can be prepared by high-dose helium implantation and subsequent annealing (see also Evans *et al.*, 1987).

Positron annihilation has proven to be very suitable for studies of helium in metals (Snead *et al.*, 1977; Hansen *et al.*, 1985; Jensen and Nieminen, 1987; Jensen *et al.*, 1988a; Rajanmäki *et al.*, 1988), but only few positron studies on helium implanted into silicon are available at present (Motoko-Kwete *et al.*, 1990; S. Mäkinen *et al.*, 1991; Simpson *et al.*, 1992).

This chapter describes positron-annihilation experiments on silicon implanted with low-dose low-energy helium both in its *as-implanted* state and after annealing. The voids induced by helium clustering have been decorated with both helium and hydrogen. The influence of the void contents on the *S*-parameter has been examined by studying the annealing behaviour.

## 5.2 Sample preparation

Helium ions have been implanted at a slightly off-normal orientation into a *p*-type B-dope float-zone c-Si(100) wafer (17–23  $\Omega\text{cm}$ ) of  $\sim 25 \times 25 \text{ mm}^2$ . The implantations were carried out with the ion

source described in section 3.2.3 with the sample mounted on the sample holder described in section 3.2.2, so that alternate *in-situ* anneals and positron-beam measurements were possible. Ion-mass selection was taken care of by adjusting the Wien filter so that helium and hydrogen implantations were done principally with  $\text{He}^+$  and  $\text{H}_2^+$  ions respectively, while the beam was swept over the sample by applying low-frequency voltages to the deflection plates (compare figure 3.6 on page 57), which led to homogeneous implantations over an area of at least  $20 \times 20 \text{ mm}^2$ . Ion doses were determined by integration of the ion current over time and have an error of about 20 %. During the room-temperature implantations the ion current was approximately  $1 \mu\text{A}$ . There was no measurable sample heating.

The first implantation (labelled *low-dose* helium implantation) was done with 2.5 keV  $\text{He}^+$  to a dose of  $8 \times 10^{15} \text{ cm}^{-2}$ , i.e. a maximum helium concentration of  $\sim 3 \text{ at.}\%$  at a depth of  $\sim 30 \text{ nm}$  (Gnaser *et al.*, 1986). Thermal Helium Desorption Spectrometry (THDS; see figure 5.1) shows that this dose results in the creation of small helium-vacancy complexes from which the helium starts to desorb at  $\sim 300^\circ\text{C}$  (Van Veen *et al.*, 1991). Positron-beam measurements have been performed after the implantation and after 5 min. anneals at 600, 700, 800, and  $900^\circ\text{C}$ . After the  $900^\circ\text{C}$  anneal all helium-induced defect complexes were removed from the sample.

The same sample has been implanted for a second time, again with 2.5 keV  $\text{He}^+$ , but now to a dose of  $1.6 \times 10^{16} \text{ cm}^{-2}$ , i.e. a maximum helium concentration of  $\sim 6 \text{ at.}\%$  (*high-dose* helium implantation). At room temperature this implantation leads to the formation of small helium bubbles, that start to dissociate and agglomerate to larger bubbles at temperatures above  $\sim 400^\circ\text{C}$ , finally releasing the helium (Evans *et al.*, 1987). This is in accordance with the THDS experiments of figure 5.1. These show that helium release principally takes place at temperatures above  $600^\circ\text{C}$ , which is consistent with desorption from larger voids (compare Fink *et al.*, 1991). The sample has been subjected to positron-annihilation measurements both in its as-implanted state and after several 5 min. anneals, this time performed at 600, 700, 750, and  $800^\circ\text{C}$ . By the latter anneal all helium desorbed but the voids were not removed.

The voids created by the  $1.6 \times 10^{16} \text{ He}^+/\text{cm}^2$  bombardment have

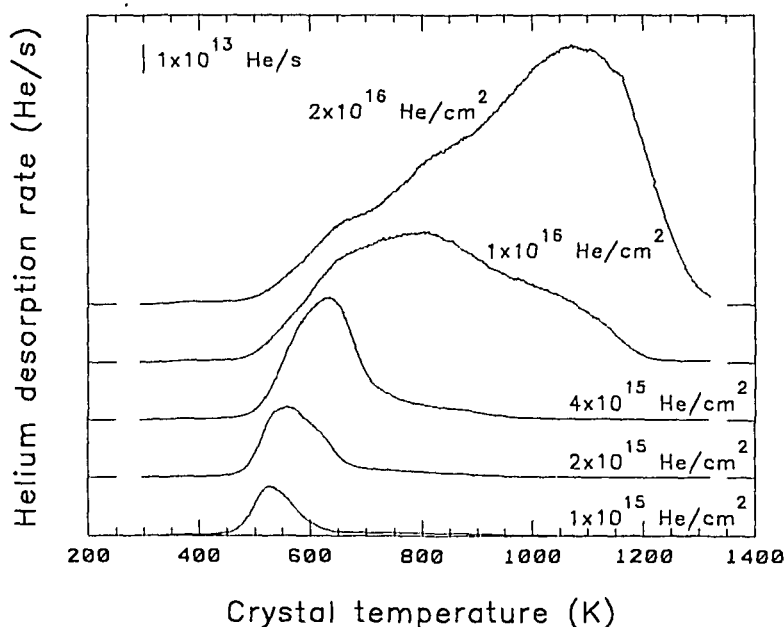


Figure 5.1: Thermal helium desorption spectra for 2.5 keV  $\text{He}^+$  implanted into silicon (heating rate: 10 K/s). The dose has been varied as indicated. The  $2 \times 10^{16} \text{ cm}^{-2}$  implantation and subsequent annealing to 1000 K induces void formation.

been decorated with both helium and hydrogen. Firstly, the sample has been subjected to an  $8 \times 10^{15} \text{ He}^+/\text{cm}^2$  implantation, followed by a  $300^\circ\text{C}$  anneal (also for 5 min.). Secondly, the sample has been implanted again with  $8 \times 10^{15} \text{ He}^+/\text{cm}^2$ . Since the helium of the first implantation was still present, the total implanted dose amounted to  $1.6 \times 10^{16} \text{ He}^+/\text{cm}^2$ . Helium was released from the sample by letting the gas desorb at  $800^\circ\text{C}$ . Thirdly, the voids have been filled with hydrogen by a 2.5 keV  $\text{H}_2^+$  implantation to a dose of  $8 \times 10^{15} \text{ cm}^{-2}$ . This time annealing steps at 200, 600, and  $800^\circ\text{C}$  were applied. It should be noted that in case of  $\text{H}_2^+$  implantation in fact two 1250 eV hydrogen atoms are injected for each  $\text{H}_2$ -molecule.

No attempt was undertaken to measure the gas released during the annealing. For desorption information we rely on the identical measurements carried out on a separate thermal-gas-desorption spectrometer shown in figure 5.1. These desorption spectra have been

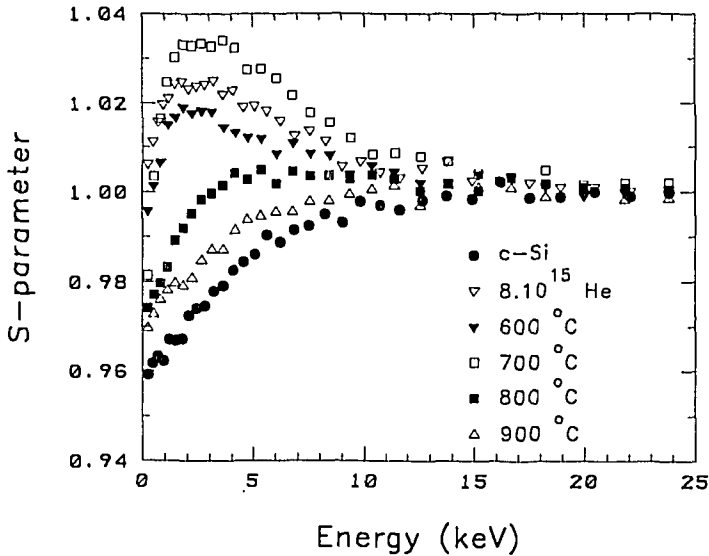


Figure 5.2: Positron-annihilation measurements of a 2.5 keV helium implantation into c-Si to a dose of  $8 \times 10^{15} \text{ cm}^{-2}$  (*low-dose*) and after subsequent anneals at 600, 700, 800, and 900 °C.

recorded with approximately the same isochronal heating rate as the annealing experiments in the positron beam apparatus, i.e. a heating rate of  $\sim 10 \text{ K/s}$ .

## 5.3 Results

The results of the positron-annihilation measurements of the *low-dose* helium implantation into c-Si ( $8 \times 10^{15} \text{ cm}^{-2}$ ) and subsequent anneals are shown in figure 5.2, the results of the *high-dose* helium implantation ( $1.6 \times 10^{16} \text{ cm}^{-2}$ ) and anneals in figure 5.3, the results of the helium refilling of the voids induced by the second implantation in figure 5.4, and the results of the hydrogen decoration ( $8 \times 10^{15} \text{ cm}^{-2}$ ) in figure 5.5.

In order to get an indication of the change of the *S*-parameter related to the defects induced by the implantations, the positron data have been analysed with VEPFIT. According to Gnaser *et al.* (1986) the projected range of 2.5 keV helium in silicon amounts to 30 nm

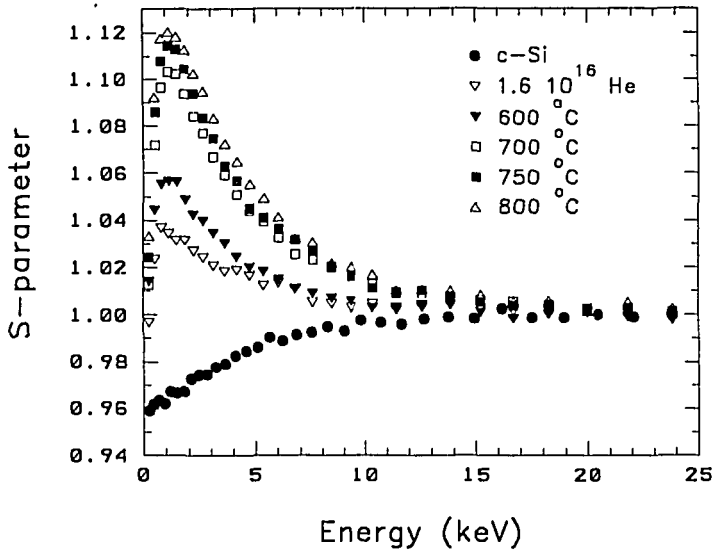


Figure 5.3: Positron-annihilation measurements of a 2.5 keV helium implantation into c-Si to a dose of  $1.6 \times 10^{16} \text{ cm}^{-2}$  (*high-dose*) and after subsequent anneals at 600, 700, 750, and 800 °C.

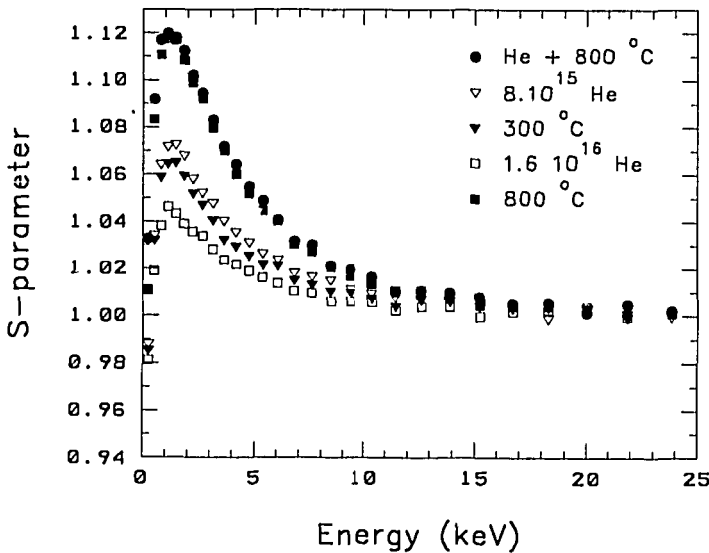


Figure 5.4: Refilling of the voids in c-Si created by the *high-dose* implantation, with 2.5 keV helium to doses of  $8 \times 10^{15} \text{ cm}^{-2}$  and  $1.6 \times 10^{16} \text{ cm}^{-2}$  and after anneals at 300 and 800 °C, respectively.

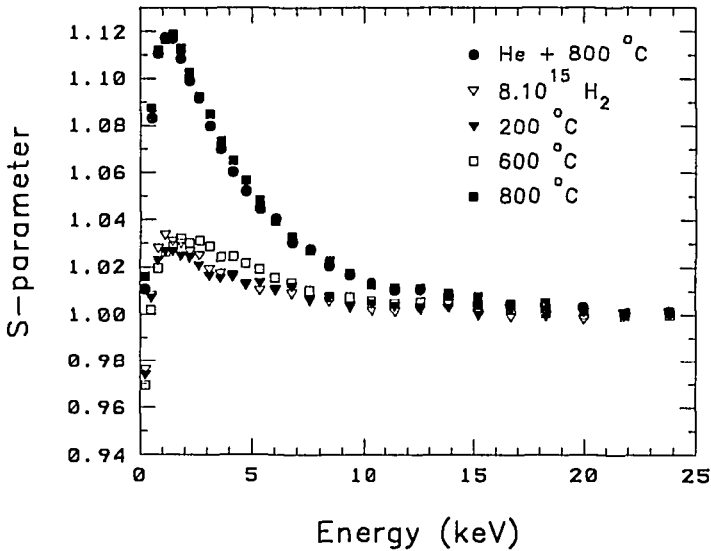


Figure 5.5: Decoration of voids in *c*-Si by a 2.5 keV hydrogen implantation to a dose of  $8 \times 10^{15} \text{ cm}^{-2}$  and after anneals at 200, 600, and 800 °C.

with a range straggling of  $\sim 40 \text{ nm}$ . These data have been included in the fit model by assuming a Gaussian defect profile characterized by the two afore mentioned quantities. The fitted *S*-parameters related to the helium damage after the various implantations and anneals, normalized to the *S*-value of *c*-Si, are tabulated in table 5.1. It should be remembered that some of the fits were rather poor. The relative *S*-values are only serving as an indication of the shift in the *S*-parameter after the several sample treatments.

## 5.4 Discussion

### 5.4.1 Low-dose helium implantation

By the first, *low-dose* helium implantation ( $8 \times 10^{15} \text{ cm}^{-2}$ ) only small point defects (e.g., divacancies, trivacancies, etc.) are formed. This is consistent with the observed helium desorption even at a rather low temperature (desorption starts at 300 °C; compare Van Veen *et al.*, 1988), although at this temperature part of the helium released from

*Table 5.1:* Fitted defect  $S$ -parameters of 2.5 keV helium-implanted Si(100) to doses of  $8 \times 10^{15} \text{ cm}^{-2}$  and  $1.6 \times 10^{16} \text{ cm}^{-2}$ , and a 2.5 keV hydrogen implantation ( $8 \times 10^{15} \text{ cm}^{-2}$ ) after the 800 °C anneal of the *high-dose* helium implanted specimen. The  $S$ -parameters, normalized to  $S_{\text{c-Si}}$  and estimated by assuming a gaussian defect profile, are only indicative.

anneal temperature	$8 \times 10^{15} \text{ cm}^{-2}$ 2.5 keV He <sup>+</sup>	$1.6 \times 10^{16} \text{ cm}^{-2}$ 2.5 keV He <sup>+</sup>	$8 \times 10^{15} \text{ cm}^{-2}$ 2.5 keV H <sub>2</sub> <sup>+</sup>
—	1.035	1.038	1.032
200 °C	...	...	1.025
600 °C	1.022	1.054	1.034
700 °C	1.039	1.103	...
750 °C	...	1.116	...
800 °C	1.007	1.119	1.118
900 °C	1.0002	...	...

the small vacancy-complexes clusters with other helium atoms before it reaches the surface. After implantation the  $S$ -parameter related to the defects amounts to  $\sim 1.035$ , also indicating small vacancy-type defects (compare table 7.3 on page 143).

At room temperature the helium atoms are immobile but the monovacancies are mobile and have therefore disappeared. The divacancies ( $V_2$ ) and trivacancies ( $V_3$ ) are immobile and form positron traps. Probably helium filled monovacancies (HeV, formed by  $\text{He} + \tilde{V} \rightarrow \text{HeV}$ , with  $\tilde{V}$  denoting a mobile monovacancy) are invisible for positrons (compare section 5.4.3 below).

After an anneal at 600 °C the  $S$ -parameter shows a shift downward to  $\sim 1.022$ , which can be explained by the removal of the smaller defects during the anneal (e.g.,  $\text{HeV} \rightarrow \text{He} + \text{V}$ ; Van Veen *et al.*, 1988) and the removal of the excess vacancies from larger  $\text{He}_m\text{V}_n$ -clusters (as irradiated:  $n \gtrsim m$ ; after loss of excess vacancies:  $n \approx m$ ).

At a temperature around 100 °C the helium atoms start to be mobile. According to the early data of Van Wieringen and Warmoltz (1956), the solution enthalpy of interstitial helium in silicon is as low as 0.5 eV, while the helium migration energy is rather large (1.2 eV). Therefore, the dissociation energy of helium from any defect in silicon

should not exceed 1.7 eV (assuming the Van der Waals binding of helium with silicon can be neglected). Applying a first order detrapping mechanism with attempt frequencies of the order of the Debye frequency ( $10^{13} \text{ s}^{-1}$ ) and neglecting entropy effects, helium desorption from the defects is expected to start at a temperature not higher than 550 K (Van Veen, 1991). Defects like the  $\text{HeV}_2$  ( $\text{He} + \text{V}_2$ ) and  $\text{He}_2\text{V}$  ( $\text{He} + \text{HeV}$ ) complexes can now be formed. Divacancies become mobile somewhere between 470 and 610 K (Watkins and Corbett, 1965; Dannefaer *et al.*, 1976; Corbett *et al.*, 1981; Mayer *et al.*, 1985; Keinonen *et al.*, 1987). In this temperature range both helium release from  $\text{HeV}_2$  and  $\text{He}_2\text{V}$  defects and some vacancy clustering may start, accounting for the observed decrease of the  $S$ -parameter (compare S. Mäkinen *et al.*, 1991).

During the anneal at  $700^\circ\text{C}$  the  $S$ -parameter increases to  $\sim 1.039$ . Helium is released from the small vacancy-complexes, probably accompanied by vacancy clustering to some extent (*Ostwald ripening*; see, e.g., Greenwood and Boltax, 1962; Markworth, 1973; Rothaut *et al.*, 1983), leading to an increase of the  $S$ -parameter. As will be discussed below, helium present in the vacancies prohibits positrons trapping in the centres of these cavities. The only available positron traps are near the inner surface of the small vacancy-complexes. This leads to relatively low  $S$ -values (much overlap with core-electron wave functions). Once the helium is desorbed, the small cavities are empty and deeper positron traps farther away from the silicon atoms become available.

Annealing the sample at  $800^\circ\text{C}$  leads to a strong reduction in the  $S$ -parameter down to  $\sim 1.007$ . After an anneal at  $900^\circ\text{C}$  the  $S(E)$ -curve has almost returned to the shape of the curve for c-Si (see figure 5.2). Obviously, almost all irradiation damage has been removed from the sample by the latter anneal (compare Keinonen *et al.*, 1987).

### 5.4.2 High-dose helium implantation

By the second, *high-dose* helium implantation larger helium agglomerates are formed in the silicon (see Griffioen *et al.*, 1987, and compare figure 5.1). A high-dose irradiation leads to the formation of small

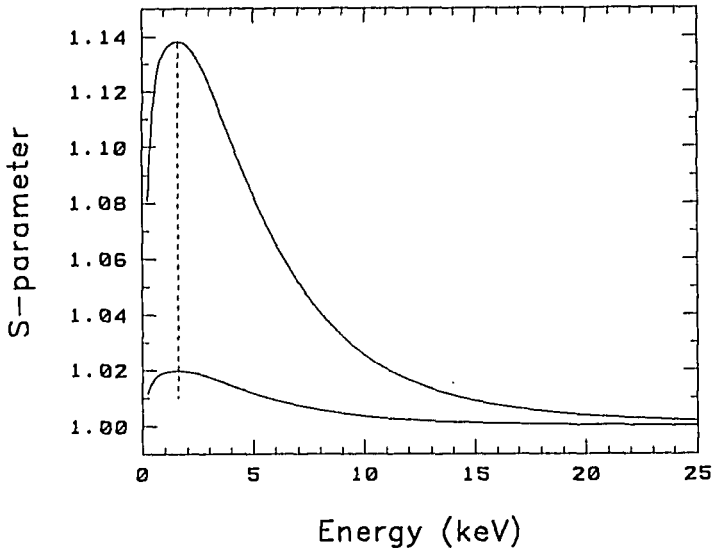


Figure 5.6: Simulated  $S(E)$ -curves of a gaussian defect profile in silicon. Input parameters:  $S_b = S_s = 1.00$ , bulk diffusion length: 245 nm, minimum diffusion length in defected region: 2 nm, position gaussian: 30 nm under surface, *fwhm* gaussian: 40 nm, and defect  $S$ -parameters of 1.02 (lower curve) and 1.14 (upper curve). The energies for which the  $S$ -parameter reaches a maximum value are comparable for both curves.

helium bubbles during the implantation itself (see Evans *et al.*, 1987), in contrast with the low-dose helium case where only the formation of smaller helium-vacancy complexes is expected (note that cluster growth does not go linearly with the ion dose). This is consistent with the positron-annihilation data, since the  $S$ -parameter related to the defects in the damaged silicon is somewhat higher than in the case of the *low-dose* helium implantation, namely  $\sim 1.038$ .

Besides, the damage peak lies closer to the surface for the *high-dose* implantation than for the *low-dose* implantation. The absence of a shift in the peak position of the simulated  $S(E)$ -curves in figure 5.6 proves that a shift of the  $S$ -peak to lower energies cannot only be accounted for by an increasing defect  $S$ -parameter. A comparison of the position of the peak in figure 5.3 with the peak positions in figure 5.2 now shows that the defect region lies closer to surface in case of the *high-dose* implantation.

Sample annealing at 600 °C leads to an increase of the  $S$ -parameter to  $\sim 1.054$ , indicating helium desorption from the voids. Anneals at 700–800 °C lead to even higher  $S$ -parameters of  $\sim 1.10$ – $1.12$ . At the latter temperature all helium is released from the voids, but the voids themselves are still stable. Evans *et al.* (1987) observed a significant release of helium in silicon around 1000 K, leading to the formation of empty cavities. The empty voids form strong positron traps in which even positronium can be formed. In our opinion, positronium formation is responsible for the observed high  $S$ -parameter. This will be argued in section 7.4.3.

Our results are consistent with the experiments of Motoko-Kwete *et al.* (1990), who implanted MeV helium into silicon to a dose of  $4 \times 10^{17} \text{ cm}^{-2}$ . They observed one annealing stage over a long temperature range of 700–1000 K, which they ascribed to the degassing of helium atoms from defects and the growth of the vacancy-clusters. The positron lifetime in these defects increased from 290 ps for helium filled voids to  $\sim 530$  ps for the voids at 1000 K, indicating that the vacancy-clusters have a mean size of more than 8 vacancies.

In conclusion, summarizing the results of sections 5.4.1 and 5.4.2, above  $\sim 400$  °C a continuous process of vacancy-cluster dissociation and formation of new but larger clusters or bubbles takes place (*Ostwald ripening*), which will probably be over-pressurized, i.e. their pressure is higher than the equilibrium pressure. At even higher temperatures the helium starts to desorb leaving empty cavities behind. At low dose the clusters are too small to survive and therefore completely break up (see section 5.4.1). At high dose voids are left behind that are stable at least up to 800 °C (see section 5.4.2).

### 5.4.3 Helium refilling of the voids

The sample that underwent the *high-dose* helium implantation contained empty large voids in the top layer after the 800 °C anneal. These voids have been refilled with helium by a 2.5 keV helium implantation both to a low dose ( $8 \times 10^{15} \text{ cm}^{-2}$ ) and to a high dose ( $1.6 \times 10^{16} \text{ cm}^{-2}$ ). The results presented in figure 5.4 show clearly that the  $S$ -parameter is influenced by the implantation.

After the low-dose re-implantation of helium, the  $S$ -parameter

decreased from  $\sim 1.119$  to  $\sim 1.073$ . This probe dose of helium was sufficient to partially refill the empty cavities, though trapping in the silicon matrix also took place. Annealing at  $300^\circ\text{C}$  leads to the somewhat lower value of  $\sim 1.065$ . Presumably, after implantation the helium atoms have only partly filled the voids, but at  $300^\circ\text{C}$  more helium atoms detrapp from small helium-vacancy complexes and start diffusion. Finally, nearly all atoms become trapped in the cavities. At this temperature it is highly improbable that there are still helium atoms left at interstitial sites and in small defects.

After another helium implantation to a dose of  $8 \times 10^{15} \text{ cm}^{-2}$  the total implanted helium amounted to  $1.6 \times 10^{16} \text{ cm}^{-2}$  (it should be noted that some of the helium may have desorbed during the  $300^\circ\text{C}$  anneal). Now, the  $S$ -parameter appears to have decreased further to a value of  $\sim 1.046$ . A comparison of this value with the  $S$ -value after the initial *high-dose* helium implantation (1.0377) shows that it is somewhat higher. This difference can be accounted for by realizing that the re-implantation also generates new damage while some of the helium was already lost by the  $300^\circ\text{C}$  anneal. Therefore, the effective helium filling of the defects is lower than after the initial *high-dose* helium implantation. After annealing at  $800^\circ\text{C}$  all helium atoms have been desorbed, which is evident from the  $S$ -value that has resumed its original high value of  $\sim 1.12$ .

These experiments show clearly that helium filling of the voids affects the positron-annihilation characteristics. Although the voids can be filled only partially after the low-dose helium re-implantation, the helium atoms trapped in the vacancy-complexes effectively reduce low-momentum annihilations. Since helium is an inert gas, there is no bond between helium and silicon atoms (like Si-H bonds in case of hydrogen). Therefore, the helium atoms are probably located in the centres of the voids, only leaving traps for the positrons near the inner surface of the cavities. By lowering the available positron-trap volume, the formation probability of positronium, which in our opinion accounts for the high  $S$ -parameter for empty cavities (see section 7.4.3), is effectively reduced, leading to a significantly lower  $S$ -parameter (compare section 7.4.4). After removing the helium from the voids, the  $S$ -parameter resumes its high value. Now, the free volume of the void is again large enough to permit positron-

ium formation. It is interesting that the  $S(E)$ -curve before the re-implantation is practically identical to the curve after the 800 °C anneal (see figure 5.4). During the refilling experiments the actual cavities were unaffected and retained their original size.

#### 5.4.4 Hydrogen refilling of the voids

The voids created by the *high-dose* helium implantation have also been refilled with hydrogen, namely by a 2.5 keV  $H_2^+$  implantation to a dose of  $8 \times 10^{15}$  ions/cm<sup>2</sup>, the range of which corresponds roughly to the range of 2.5 keV helium in silicon.

After the implantation hydrogen may be present in silicon in three forms (Pearson, 1986; Boyce *et al.*, 1992):

1. *Hydrogen bound to a dangling bond at a defect site.* These states give rise to the multiplicity of Si-H stretching modes observed by infrared absorption in the frequency range 1800–2300 cm<sup>-1</sup>. This is the lowest energy site of the states of hydrogen. Hydrogen may also be trapped at an impurity or defect site where in principle a dangling bond does not exist. The Si-H bond amounts to 3.1 eV, while the binding of atomic interstitial hydrogen to silicon amounts to 1 eV (compare Johnson *et al.*, 1986), so that for dissociation  $\sim 2.1$  eV is required (see figure 5.7), corresponding to a hydrogen release temperature of  $\sim 800$  K (Van Veen, 1991). However, Myers *et al.* (1992b) note that the dissociation energy depends heavily on the other bonds formed by the same silicon atom.
2. *Molecular hydrogen* ( $H_2$ , binding energy: 1.2 eV per atom), which is the stable configuration in the absence of defect sites to which hydrogen can bond. It is formed from the reaction  $H + H \rightarrow H_2$  at low temperature in the absence of dangling bonds, but also at temperatures above 400 °C, when bound hydrogen starts to diffuse but out-diffusion is still negligible (Cerofolini *et al.*, 1990). Molecular hydrogen is electrically and optically inactive and essentially immobile at low temperatures ( $< 500$  °C). Molecular hydrogen may either be present in large voids or otherwise occupy the tetrahedral site under equilibrium conditions.

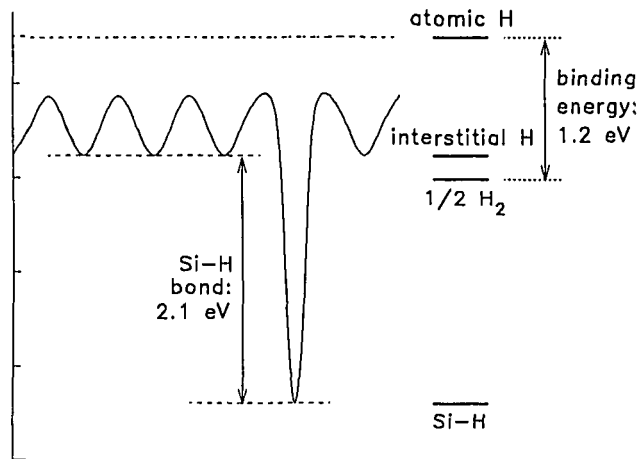


Figure 5.7: Schematic representation of the energy levels of the several hydrogen states in silicon, viz. atomic hydrogen, molecular hydrogen and hydrogen bound to silicon (Si-H bond).

3. *Atomic hydrogen* occupying the so-called (interstitial) M-site (see Corbett *et al.*, 1983; Shi *et al.*, 1984). The diffusivity of this species is high even at room temperature (as high as  $10^{-11}$  cm<sup>2</sup>/s; Seager and Anderson, 1988; Buda *et al.*, 1989). It is the state responsible for the passivation of dangling-bond electrical activity. Due to its high diffusivity it is apt to bond at defect sites or to coalesce into molecules. The migration energy of atomic hydrogen amounts to 0.5 eV (Van Wieringen and Warmoltz, 1956; compare Johnson *et al.*, 1991).

The hydrogen implantation led to a decrease of the  $S$ -parameter from  $\sim 1.12$  to  $\sim 1.032$ . It decreased further to  $\sim 1.025$  after the short anneal at 200 °C. Annealing at 600 °C led to a small recovery of the  $S$ -parameter to  $\sim 1.034$ , but only after the anneal at 800 °C it was restored to its high value of  $\sim 1.12$  (see figure 5.5).

By the introduction of hydrogen into the sample, some of the hydrogen bonds to silicon dangling bonds (forming Si-H bonds), some hydrogen gets trapped in the voids and forms a molecular gas, while

the remaining hydrogen either occupies interstitial sites in the silicon lattice or sticks at the inner surface of the voids (surface adsorption). The fractions of atomic and molecular hydrogen in the silicon are in thermodynamic equilibrium (Shi *et al.*, 1984; Pearton, 1986). The molecular hydrogen in the voids will repel any positron or formed positronium from the interior of the voids (leading both to a reduction of the positronium formation probability and to increased annihilations in the proximity to the surface), while the atomic hydrogen adsorbed at the surface also influences the positronium formation probability and the positron-annihilation characteristics. The combined effect of these processes is a large reduction of the  $S$ -parameter after hydrogen implantation. In summary, the passivating effect of hydrogen can be explained by hydrogen trap filling resulting in a reduction of the number of positronium annihilations (which give rise to a high  $S$ -parameter; see section 7.4.3).

This is in accordance with the experiments of Gossmann *et al.* (1992) who measured the  $S$ -parameter for a silicon surface terminated with hydrogen to be equal to that for bulk silicon. In addition, Lynn *et al.* (1989) and Rubloff *et al.* (1990) observed a decrease of the surface  $S$ -parameter of a very thin ( $\sim 2$  nm)  $\text{SiO}_2$  layer on Si(111) upon  $\text{H}_2$  exposure (compare also Brower, 1988). With respect to surface trapping of positrons, the mentioned authors concluded that their results suggest that positrons and hydrogen may be trapped at the same, or nearby, sites. The high temperature anneal needed to reverse the hydrogen adsorption ( $> 700^\circ\text{C}$ ) suggested a strong binding to the trapping site. Nielsen *et al.* (1989) have reported that hydrogen interacts with defects at the Si/ $\text{SiO}_2$  interface, changing the electronic structure of the defects and leading to lower  $S$ -parameters, but their conclusion has been called into question by Smith *et al.* (1990b) since the latter authors observed no change in the  $S$ -parameter after a 40 keV hydrogen implantation. However, it is beyond doubt that hydrogen may passivate the electrical activity of defects that otherwise attract positrons (Brusa *et al.*, 1992; Smith *et al.*, 1992).

By the  $200^\circ\text{C}$  anneal detrapping from small defects and diffusion of atomic hydrogen is enhanced. This probably leads to an increased molecular-hydrogen pressure in the voids, which is evident from the

small reduction of the  $S$ -parameter after the anneal. Keinonen *et al.* (1988) have shown that hydrogen tends to saturate vacancy sites while on the other hand, vacancies seem to be associated with Si-H centres.

The small rise of the  $S$ -parameter after the 600 °C anneal can be explained by the detrapping and diffusion of bound hydrogen (in Si-H bonds), which may start at a temperature around 550 °C (see above). The peak in the  $S(E)$ -curve (corresponding with the defect profile) is now somewhat broader (see figure 5.5), probably indicating that some hydrogen desorption from the voids also takes place (resulting in more open volume in the voids). This effect is clearly visible in the energy region between 3 and 6 keV, but is masked by other defects in the peak-region of the spectrum (1–3 keV). The measured recovery temperature is in agreement with the results of Myers *et al.* (1992a), who reported deuterium release from helium-implanted silicon starting at  $\sim 550$  °C

After the 800 °C anneal all hydrogen has been released from the sample and the voids are empty again. Positronium formation is now possible again, restoring the  $S$ -parameter to its high value.

## 5.5 Conclusions

In this chapter it has been shown that stable voids can be created in silicon by helium implantation and annealing. The (smaller) voids created by a *low-dose* helium implantation ( $8 \times 10^{15} \text{ cm}^{-2}$ ) could be removed by annealing at 800 °C but the (larger) voids resulting from a *high-dose* helium implantation ( $1.6 \times 10^{16} \text{ cm}^{-2}$ ) were stable at least up to 800 °C. It was also possible to refill these voids with helium and hydrogen. By annealing the void structure as before the second implantation was completely recovered.

The effect of helium and hydrogen present in silicon containing voids is understood. The decoration of the voids with these gases leads to a reduction of the  $S$ -parameter, which is large for the empty cavities. This passivating effect is for *helium* ascribed to the build-up of an high atomic density and thus increased overlap with the core-electrons within the cavity. For *hydrogen* the effect is ascribed both to

---

the molecular-hydrogen gas filling of the voids and to the decoration of the inner surface of the cavities by atomic hydrogen. Both effects diminish the positronium formation probability which is responsible for the high  $S$ -values of large empty cavities in silicon.

NEXT PAGE(S) left BLANK.

# Chapter 6

## Ion-beam amorphized silicon

### 6.1 Introduction

Both amorphous (a-) and crystalline (c-) silicon may contain structural defects. In crystalline silicon, many defects have been identified. Examples are the divacancy and the dislocation loop, which have been identified by spectroscopic and imaging techniques such as Electron Paramagnetic Resonance (EPR) and Transmission Electron Microscopy (TEM), respectively. In amorphous silicon, only one defect has been identified (by EPR), namely the dangling bond. This identification, however, is limited in the sense that very little is known about the atomic structure surrounding the dangling bond except that it may vary from site to site, whence the wide range of recovery temperatures (Thomas *et al.*, 1978). Moreover, because EPR has a limited sensitivity (it can only probe defects if they have an unpaired electron, i.e. a dangling bond; see, e.g., Watkins and Corbett, 1965), it cannot be excluded that other types of defects exist in amorphous silicon.

It has been suggested that not only the electrical but also the structural properties of amorphous silicon are dominated by defects (Turnbull, 1986). In this view structural relaxation, which is also known as short-range ordering, is thought to be mainly controlled by atomic motion similar to the atomic motion responsible for damage repair in heavily defected crystalline silicon. Experimental indications

supporting this suggestion were primarily based on calorimetry of radiation damage in amorphous silicon (Roorda *et al.*, 1990a). It was found that the kinetics and the temperature dependence of annealing of ion-irradiation damage in amorphous silicon cannot be distinguished from those of defect annealing in similarly treated crystalline silicon. This has been corroborated by Raman spectroscopy of ion-damage accumulation in relaxed amorphous silicon (Roorda *et al.*, 1990b). More recently, measurements of impurity (Cu, Pd) diffusion and solubility in amorphous silicon showed a complicated behaviour that can be understood very well within the framework of a defect-mediated structural relaxation in amorphous silicon (Polman *et al.*, 1990; Coffa *et al.*, 1991). It is noteworthy that the above results, although based on entirely different experimental techniques, are not only in *qualitative*, but also in *quantitative* agreement (Roorda, 1990; Roorda *et al.*, 1991). In addition to the above-mentioned probes of defects in amorphous silicon, there has recently been reported Mössbauer spectroscopic evidence for the vacancy-Sb complex to be microscopically similar in amorphous and crystalline silicon (Van den Hoven *et al.*, 1992).

Positron annihilation is a sensitive probe of vacancies and vacancy-type defects in metals and semiconductors. It has been used to study monovacancies (Dannefaer *et al.*, 1986; S. Mäkinen *et al.*, 1991) and divacancies (Mascher *et al.*, 1989; Simpson *et al.*, 1991) in crystalline silicon but also to detect vacancy-type defects in amorphous metals and voids in both pure and hydrogenated amorphous silicon (Dannefaer *et al.*, 1983; He *et al.*, 1986; Bhide *et al.*, 1987). This chapter reports how positron annihilation has been used to study radiation damage, structural relaxation, and defect passivation in amorphous silicon. In addition, lifetime measurements of photogenerated carriers have been performed (see section 3.3.1). The positron annihilation results are consistent with the notion that amorphous silicon contains a large variety of vacancy-like defect structures, some of which disappear upon thermal annealing. The results appear to be in quantitative agreement with the calorimetry and impurity-diffusion measurements. From the hydrogen-induced detrapping of metal impurities (Cu, Pd) in amorphous silicon, it has been shown that electrical defects in *as-implanted* amorphous silicon are associated with structural imper-

fections, possibly vacancy-type defects, controlling diffusion of transition metals (Coffa and Poate, 1991). Our present results also indicate that such a correlation exists.

The generally accepted mechanism of the crystalline-to-amorphous transition under ion bombardment is that highly disordered zones are produced in lower deposited energy-density zones (outside the cascade core), and overall amorphization follows when sufficient overlap occurs (compare Müller and Kalbitzer, 1980; Ruault *et al.*, 1983; Washburn *et al.*, 1983; Elliman *et al.*, 1988; Tamura and Suzuki, 1989). Implanted ions, both light and heavy, always create Frenkel pairs. The defect zones coalesce when the dose becomes sufficiently high, and thus amorphous zones are formed.

It should be pointed out here that this study concerns *pure* and *void-free* amorphous silicon rather than hydrogenated amorphous silicon (a-Si:H). By applying silicon implantation into high-purity c-Si targets, amorphous silicon can be prepared in a form free of macroscopic voids or impurities which may occur in amorphous silicon made by evaporation or sputter deposition (Bean and Poate, 1980; Saitoh *et al.*, 1981). Voids especially can have a large effect on the interaction between positrons and amorphous silicon, as has already been shown (Dannefaer *et al.*, 1983; He *et al.*, 1986; Blide *et al.*, 1987). A comparative study on positron annihilation in several types of amorphous silicon will be given in chapter 7 (see also Hakvoort *et al.*, 1992a and 1992b). The aim of the present study is to investigate (changes in) the atomic structure of amorphous silicon. Therefore, we have used pure amorphous silicon prepared by ion implantation. In some of the samples we have post-implanted hydrogen into the amorphous silicon. Our results on hydrogen in a-Si are expected to relate to the hydrogenated amorphous silicon of chapter 7 only insofar as isolated Si-H bonds in a-Si:H are concerned and not to clustered Si-H bonds associated with microvoids and internal surfaces.

## 6.2 Sample preparation

Amorphous layers of  $\sim 1 \mu\text{m}$  thickness were formed on c-Si wafers by  $^{28}\text{Si}^+$  implantation (0.5 and 1 MeV,  $5 \times 10^{15} \text{ cm}^{-2}$  each). The ion beam

was defocused and rastered electrostatically over the sample surface. During the implantations, the temperature of the targets, which were heat sunk to a liquid-nitrogen cooled piece of solid copper, was about  $-100^{\circ}\text{C}$ . The ion current was kept below 25 nA, which resulted in negligible sample heating during the implantations. Several pieces of  $15 \times 15 \text{ mm}^2$  were prepared. One piece was set aside (*as-implanted*). Most pieces were annealed in vacuum at  $500^{\circ}\text{C}$  for 1 h (*annealed*), some of which were subsequently re-implanted with 0.5 MeV  $^{28}\text{Si}^+$  ions, but this time to much lower doses of  $2.5 \times 10^{11}$ ,  $2.5 \times 10^{12}$ , or  $2.5 \times 10^{13} \text{ cm}^{-2}$  (*damaged*). Pieces of c-Si were also subjected to these low-dose implantations whereupon the damage profiles (in c-Si) were measured by ion scattering and channelling of 2 MeV helium ions. During the low-dose implantations, the samples were not cooled.

Some a-Si samples were implanted with hydrogen ions ( $\text{H}^+$ ) and annealed at  $150^{\circ}\text{C}$ . One implantation was performed using an energy of 50 keV and a dose of  $1 \times 10^{17} \text{ ions/cm}^2$ . This implantation resulted in a hydrogen implantation profile that peaks at a depth of  $\sim 0.5 \mu\text{m}$ , where it reaches a local hydrogen concentration of  $\sim 7 \text{ at.}\%$ . In addition, a sample was implanted with 2, 4, and 15 keV  $\text{H}_2^+$  ions to a dose of  $5 \times 10^{15} \text{ cm}^{-2}$ , resulting in a hydrogen profile that is distributed over  $0.15 \mu\text{m}$  in the near-surface region. For the low-energy implantation, the peak hydrogen concentration is about 2.5 at.%. The 50 keV hydrogen implanted sample was used for positron-annihilation measurements. The depth of the hydrogen profile was chosen to optimize the possible effect of defect passivation by implanted hydrogen on the positron experiments. The low-energy implanted material was used for carrier-lifetime measurements. The range of the implanted hydrogen corresponds to the probe depth of the laser light.

The (*ex-situ*) thermal anneals at  $500^{\circ}\text{C}$  were carried out in a quartz-tube vacuum furnace at a pressure below  $10^{-6}$  inbar. The (*in-situ*) thermal anneals at  $150^{\circ}\text{C}$  in between positron-annihilation experiments were performed by heating a filament in close proximity to the sample. The temperatures are nominal values only (with an accuracy of  $\pm 10^{\circ}\text{C}$ ).

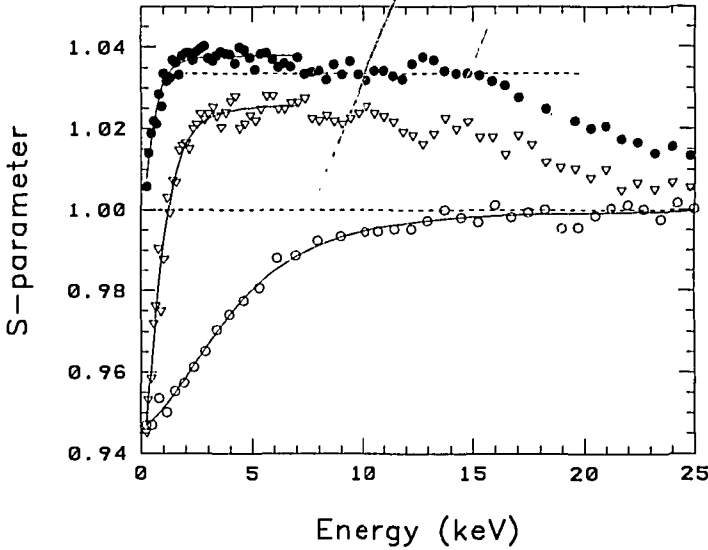


Figure 6.1:  $S$ -parameter (normalized to bulk  $c$ -Si) as a function of the positron incident energy for  $c$ -Si ( $\circ$ ), *as-implanted* pure  $a$ -Si ( $\bullet$ ), and *annealed* pure  $a$ -Si ( $\nabla$ ). The dashed line indicates the  $S$ -value of  $150^\circ\text{C}$  annealed  $a$ -Si.

## 6.3 Results

### 6.3.1 Ion-implantation amorphized silicon and thermal annealing

The results of the positron-annihilation measurements for  $c$ -Si, *as-implanted*  $a$ -Si and *annealed*  $a$ -Si are shown in figure 6.1. The results of the VEPFIT analysis of the first 7 keV of the spectra are presented in table 6.1. The fits assume a homogeneous damage profile and serve as estimates for the  $S$ -parameters and the diffusion lengths. Extraction of damage profiles has not been attempted.

The  $S(E)$ -curves for the  $a$ -Si samples differ in two ways from that for  $c$ -Si: (1) The  $S$ -parameter is considerably higher, and (2) the positron diffusion length is much shorter (see table 6.1). Both effects are in accordance with the results of Hautojärvi *et al.* (1988) and Nielsen (1990). The  $500^\circ\text{C}$  anneal results in a slight decrease of the  $S$ -parameter and a substantial increase of the diffusion length (from

*Table 6.1:* Summary of the fit results of the  $S$ -parameter (normalized to bulk c-Si) and the positron diffusion length ( $L$ ) derived from the positron-annihilation measurements (first 7 keV), and of the fitted carrier lifetimes derived from the carrier-lifetime measurements ( $\tau$ ). ‘Deep hydrogen’ means a 50 keV  $H^+$  implantation, ‘shallow hydrogen’ a 2, 4 and 15 keV  $H_2^+$  implantation. The labels (a), (b) and (c) for the ‘damaged’ samples indicate 0.5 MeV  $Si^+$  implantations to a dose of  $2.5 \times 10^{11} \text{ cm}^{-2}$ ,  $2.5 \times 10^{12} \text{ cm}^{-2}$ , and  $2.5 \times 10^{13} \text{ cm}^{-2}$ , respectively.

sample description	anneal temperature	$S$ ( $\pm 5 \times 10^{-4}$ )	$L$ (nm) ( $\pm 0.5$ )	$\tau$ (ps) ( $\pm 10\%$ )
c-Si	—	1.0000	245 $\pm$ 5	...
as-implanted	—	1.0379	8.6	1
low $T$ annealed	150 °C	1.0336	...	1.6
high $T$ annealed	500 °C	1.0257	15.5	11
deep hydrogen	—	1.0391	6.5	...
deep hydrogen	150 °C	1.0249	5.3	...
shallow hydrogen	150 °C	...	...	1.6 & 13
damaged (a)	(500 °C)	1.0308	16.3	...
damaged (b)	(500 °C)	1.0317	15.0	...
damaged (c)	(500 °C)	1.0369	13.7	...

8.5 to 15.5 nm). It should be noted that this anneal temperature is far below the one necessary for noticeable crystal nucleation (Iverson and Reif, 1987), while solid-phase epitaxial crystallization at the c-Si/a-Si interface is limited to a few Å (Olson and Roth, 1988). Annealing of *as-implanted* a-Si at an even lower temperature of 150 °C led to small but noticeable changes in the  $S$ -parameter (these data are not shown except for the dashed line indicating the level of the  $S$ -parameter in figure 6.1, but the results of the curve fitting are reported in table 6.1).

### 6.3.2 Hydrogen implantation and annealing

In this section we describe the measurements on amorphous silicon that was post-implanted with  $H^+$  ions. It should be noted that this material is not grown like conventional hydrogenated a-Si (a-Si:H) and therefore may have different properties. The absence of macroscopic

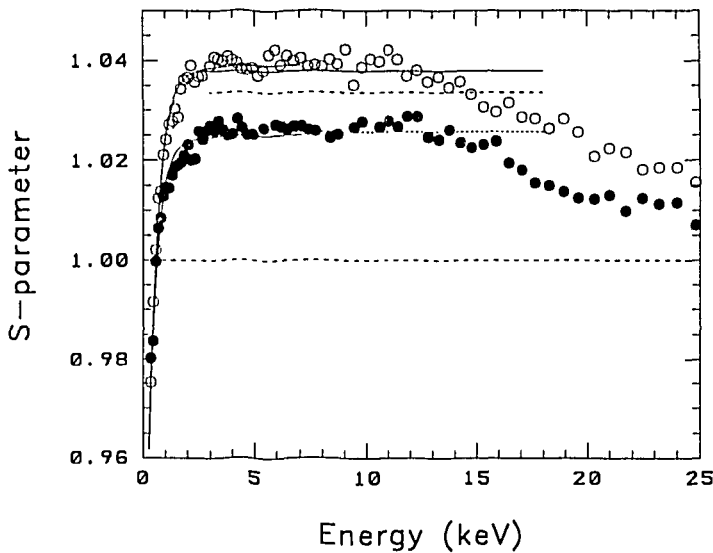


Figure 6.2:  $S$ -parameter (normalized to bulk c-Si) as a function of the positron incident energy for a-Si post-implanted with hydrogen (○) and after heating at  $\sim 150^\circ\text{C}$  for 25 h (●). The  $S$ -values of pure a-Si (*as-implanted* and after 150 or  $500^\circ\text{C}$  anneals) shown in figure 6.1 are indicated.

voids in ion-implanted a-Si, for example, may preclude the presence of clustered hydrogen that is normally found in a-Si:H.

The results of the measurements of amorphous silicon that has been post-implanted with 50 keV,  $5 \times 10^{16} \text{ cm}^{-2} \text{ H}^+$  and annealed at  $\sim 150^\circ\text{C}$  for 25 h are shown in figure 6.2.

It can be seen that merely implanting hydrogen does not change the interaction of positrons with the a-Si to a measurable extent, except perhaps a small increase in the  $S$ -parameter. However, the annealing behaviour of this material differs from that of pure a-Si. This is evident from the change in the  $S$ -parameter, which reaches a value equal to that in  $500^\circ\text{C}$  annealed pure a-Si after prolonged (25 h) annealing at  $150^\circ\text{C}$ . Apparently, the effect of high-temperature annealing of pure a-Si on the positron-annihilation measurements (a decreasing  $S$ -parameter) can be mimicked by hydrogen implantation and low-temperature annealing. It is well known that hydrogen passivates electrical defects in silicon (see, e.g., Pankove, 1992). The

present result therefore suggests a relation between the passivation of dangling and strained bonds by hydrogen and the high-temperature annealing behaviour of pure a-Si. This relation will be discussed further in section 6.4.

### 6.3.3 Radiation damage in crystalline silicon and annealed amorphous silicon

Three samples of crystalline silicon and three samples of ion-beam amorphized silicon which has been annealed in vacuum at 500 °C, have been bombarded with 500 keV Si<sup>+</sup> ions to a dose of  $2.5 \times 10^{11}$ ,  $2.5 \times 10^{12}$ , and  $2.5 \times 10^{13}$  cm<sup>-2</sup>, respectively.

The depth profile of displaced target atoms due to violent nuclear collisions (in displacements per atom, DPA) was estimated using Monte-Carlo simulation (TRIM; see Ziegler *et al.*, 1985). The amount of ion damage has also been determined by channelling measurements of 2 MeV He<sup>+</sup> ions backscattered from the identically bombarded c-Si samples. A piece of c-Si bombarded with  $2.5 \times 10^{11}$  Si<sup>+</sup> ions/cm<sup>2</sup> could not be distinguished from unimplanted c-Si, indicating that the density of displaced atoms is well below an at.%. The other sample did show a measurable increase in the dechannelling. The dechannelled yield in the sample bombarded with  $2.5 \times 10^{12}$  Si<sup>+</sup>/cm<sup>2</sup> was consistent with 0.013 DPA and the yield in the  $2.5 \times 10^{13}$  Si<sup>+</sup>/cm<sup>2</sup> sample was indicative of >0.10 DPA. It should be noted that the output of TRIM is in DPA, but the real defect concentration is much lower due to room-temperature annealing of the sample. In addition, ion channeling measures small deviations of atoms from the lattice sites and is therefore insensitive to vacancies formed by removing lattice atoms.

The positron-annihilation data of the silicon implantation into c-Si and a-Si are shown in figures 6.3 and 6.4, respectively. From the calculated ion-damage profile convoluted with the positron implantation profile (not shown) follows that the effect of ion damage on the  $S(E)$ -curves of will be most pronounced for positron energies between 4 and 10 keV. The fits of the positron-annihilation data for implanted c-Si assuming a gaussian defect profile are given in table 6.2. From

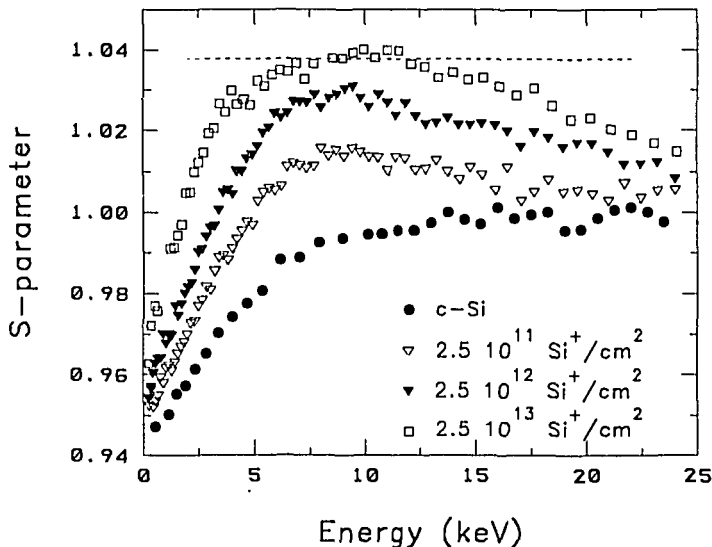


Figure 6.3:  $S$ -parameter (normalized to bulk  $c$ -Si) as a function of the positron incident energy for  $c$ -Si ( $\bullet$ ) and  $c$ -Si implanted with 500 keV  $\text{Si}^+$  to a dose of  $2.5 \times 10^{11}$  ( $\nabla$ ),  $2.5 \times 10^{12}$  ( $\blacktriangledown$ ), and  $2.5 \times 10^{13} \text{ cm}^{-2}$  ( $\square$ ). The  $S$ -value of pure  $a$ -Si (*as-implanted*) shown in figure 6.1 is indicated.

the fitted maximum trapping rates maximum defect concentrations have been derived using equation (2.9) [see page 37]. For the specific trapping rate  $\nu_i$  the value for divacancies in silicon ( $3 \times 10^{14} \text{ s}^{-1}$ ) has been taken (Dannefaer, 1987). It is interesting to note that the fitted  $S$ -parameter associated with the implantation damage lies close to the  $S$ -value of *as-implanted*  $a$ -Si. This is already true for the lowest dose implantation.

As shown by figures 6.3 and 6.4, the  $S(E)$ -curve for crystalline and amorphous silicon bombarded with the lowest ion dose already differ from that of  $c$ -Si and annealed  $a$ -Si, respectively. For silicon, bombarded with 500 keV  $\text{Si}^+$  ions to a dose of  $2.5 \times 10^{11} \text{ cm}^{-2}$ , the density of displaced silicon atoms (according to TRIM) is at most  $2 \times 10^{-4}$ . Moreover, the ion-channelling measurements suggest that the density of displaced target atoms is as low as  $1 \times 10^{-3}$  DPA. Yet the positron-annihilation measurements clearly distinguish between the slightly damaged samples and the reference material. It shows that positron annihilation is a sensitive technique for detection of

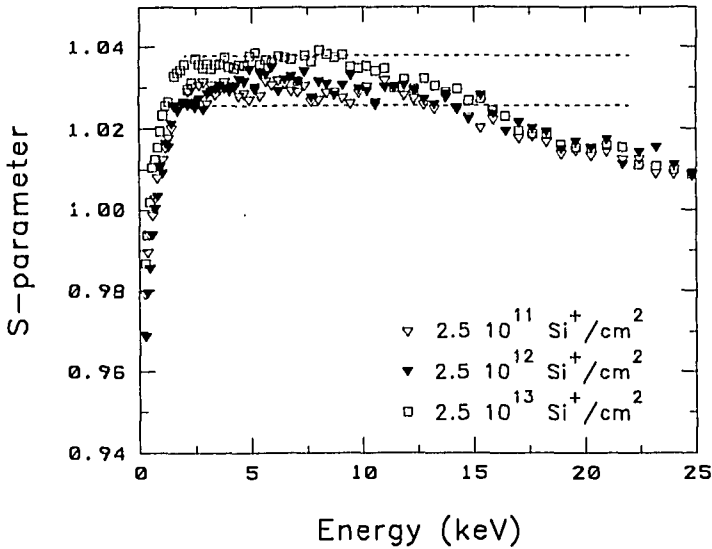


Figure 6.4:  $S$ -parameter (normalized to bulk  $c$ -Si) as a function of the positron incident energy for  $a$ -Si implanted with 500 keV  $\text{Si}^+$  to a dose of  $2.5 \times 10^{11}$  ( $\nabla$ ),  $2.5 \times 10^{12}$  ( $\blacktriangledown$ ), and  $2.5 \times 10^{13}$   $\text{cm}^{-2}$  ( $\square$ ). The  $S$ -values of pure  $a$ -Si (*as-implanted*) and  $a$ -Si after a 500 °C anneal (*annealed*) shown in figure 6.1 are indicated.

Table 6.2: Fits of the  $S$ -parameter (normalized to bulk  $c$ -Si) associated with the defects in  $c$ -Si bombarded with 500 keV  $\text{Si}^+$  to the indicated doses (see figure 6.3) and the (fitted) minimum diffusion length ( $L_{\min}$ ) and maximum trapping rate ( $\kappa_{t,\max}$ ). A gaussian defect profile has been assumed. Maximum defect concentrations ( $n_{t,\max}$ ) have been estimated with equation (2.9) using the divacancy trapping rate  $\nu_t = 3 \times 10^{14} \text{ s}^{-1}$ .

dose	$S_t$	$L_{\min}$	$\kappa_{t,\max}$	$n_{t,\max}$
$2.5 \times 10^{11} \text{ cm}^{-2}$	1.0343	132 nm	$1.1 \times 10^{10} \text{ s}^{-1}$	$3.7 \times 10^{-5}$
$2.5 \times 10^{12} \text{ cm}^{-2}$	1.0392	85 nm	$3.2 \times 10^{10} \text{ s}^{-1}$	$1.1 \times 10^{-4}$
$2.5 \times 10^{13} \text{ cm}^{-2}$	1.0408	51 nm	$9.9 \times 10^{10} \text{ s}^{-1}$	$3.3 \times 10^{-4}$

implantation damage in c-Si and a-Si.

Monte-Carlo calculations of the damage in silicon bombarded to a dose of  $2.5 \times 10^{12} \text{ cm}^{-2}$  and  $2.5 \times 10^{13} \text{ cm}^{-2}$  yield densities of displaced silicon atoms of at most  $2 \times 10^{-3}$  and  $2 \times 10^{-2}$ , respectively. A comparison with the defect concentrations in table 6.2 shows that the positron-annihilation measurements give values of more than an order of magnitude lower. This discrepancy can be accounted for by realizing that TRIM gives maximum values (defects may vanish after creation, e.g., due to the room-temperature mobility of monovacancies in silicon). Besides this, TRIM (and ion-beam methods) are sensitive to atoms displaced from lattice sites, whereas positron annihilation detects mainly vacancy-type defects (compare Mitchell *et al.*, 1990). A third reason is that the gaussian defect profile assumed for the analysis of the positron data is not very realistic (nuclear stopping leads to a highly asymmetrical defect profile).

The  $S(E)$ -curve for annealed a-Si, bombarded with  $2.5 \times 10^{13} \text{ Si}^+$  ions/ $\text{cm}^2$  already closely resembles the  $S(E)$ -curve for a-Si in its *as-implanted* state. Apparently either the damage generated by ion bombardment begins to saturate when the density of displaced atoms is several at.% or the saturation occurs not in the defect concentration but in the trapping of positrons. It follows from the silicon implantations into crystalline silicon (see figure 6.3) that the latter explanation is more probable. However, damage saturation has also been observed by Raman spectroscopy measurements (Roorda *et al.*, 1990a) and calorimetry (Roorda *et al.*, 1990b) of ion damage in a-Si. These experiments suggest that the defect density in a-Si cannot exceed a few at.%.

The fitted  $S$ -parameters and diffusion lengths of the damaged amorphous silicon samples are presented in table 6.1. Firstly, there is already a marked difference between the  $S$ -parameter of  $500^\circ\text{C}$  annealed a-Si (1.0257) and that of the least damaged sample (1.0308). Secondly, the  $S$ -value of the most highly damaged sample (1.0369) is close to that of *as-implanted* a-Si (1.0379), indicating saturation. In addition, the effective diffusion length is seen to decrease with increasing damage dose.

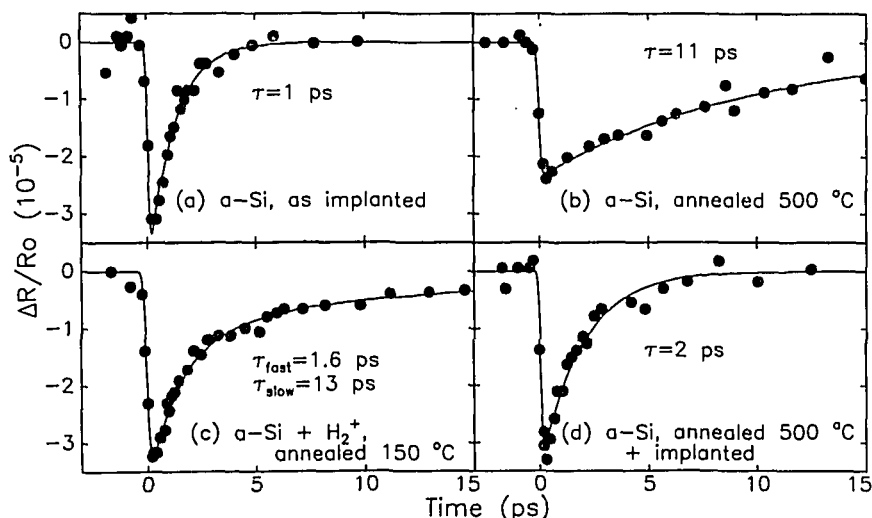


Figure 6.5: Normalized reflectivity changes (●) as a function of time difference between pump and probe for: *a.* as-implanted a-Si; *b.* a-Si annealed in vacuum at 500 °C; *c.* a-Si post-implanted with low-energy H<sup>+</sup> and annealed at 150 °C; and, *d.* a-Si annealed at 500 °C and re-implanted with 1 MeV Si<sup>+</sup> ions to a dose of  $2 \times 10^{13} \text{ cm}^{-2}$ . Time 0 corresponds to overlap of pump and probe. Solid lines are exponential decay curves convoluted with the experimental resolution.

### 6.3.4 Carrier-lifetime measurements

Free carriers (electrons and holes) have been generated and detected optically in samples similar to those previously investigated with positrons. Measurements of the reflectivity as a function of time, following on the generation of a plasma of free carriers by a 100 fs light pulse (see section 3.3.1 on page 63), are shown in figure 6.5. Four measurements are shown: (*a*) as-implanted a-Si, (*b*) a-Si annealed in vacuum at 500 °C, (*c*) a-Si post-implanted with low-energy hydrogen and annealed at 150 °C, and (*d*) a-Si annealed at 500 °C and re-implanted with 1 MeV silicon to a dose of  $2 \times 10^{13} \text{ cm}^{-2}$ . The lines represent fits assuming a single exponential decay of the photogenerated plasma (with one exception, which will be discussed below) and a time resolution of 0.2 ps.

For as-implanted a-Si (figure 6.1), the reflectivity returns to its

original level within several picoseconds. The reflectivity for *a*-Si annealed at 500 °C recovers significantly slower, and only after 60 ps the initial reflectivity is reached (not shown). For comparison: for *c*-Si a return of the reflectivity to its original value takes more than 1000 ps (Stolk *et al.*, 1992c). A significant positive change in the reflectivity, which would be indicative of sample heating (Downer and Shank, 1986; Esser *et al.*, 1990), has not been observed at the low laser intensities employed for these measurements. Higher irradiation conditions would also lead to a situation where Auger-recombination processes become important (Rehm and Fischer, 1979; Esser *et al.*, 1990). The decay time  $\tau$ , deduced from the single-exponential decay curves shown as lines, is 1 ps in *as-implanted a*-Si, and 11 ps in *annealed a*-Si.

The sample that has been post-implanted with low-energy hydrogen and annealed at 150 °C shows a reflectivity recovery, shown in figure 6.5c, intermediate between those of the previous two samples. The reflectivity initially decays at the same rate as that measured for pure *a*-Si, annealed at 150 °C ( $\tau = 1.6$  ps), but is followed by a significantly slower process ( $\tau = 13$  ps). In our opinion, this is caused by the light probing two distinct regions. In the region of the hydrogen profile ( $\sim 0.1 \mu\text{m}$  below the surface), electrical defects have been passivated but deeper (and shallower) layers that are also probed have not changed at all, except for a small thermal effect resulting from the 150 °C anneal ( $\tau = 1.6$  ps). The line through the datapoints represents the sum of two single-exponential decay curves with  $\tau = 1.6$  and 13 ps and relative intensities of 70 % and 30 %, respectively.

A carrier-lifetime measurement of an *a*-Si sample that has been annealed at 500 °C and subsequently re-implanted with 1 MeV silicon to a dose of  $2 \times 10^{13} \text{ cm}^{-2}$  is shown in figure 6.5d. The density of displaced target atoms in the near-surface region of this sample has been estimated with TRIM to amount to 0.3 at.%. The reflectivity is observed to return quickly to its original value. It can be characterized by a single-exponential decay time with a value of  $\tau = 2$  ps.

It appears that photocarrier-lifetime measurements, like positron annihilation, can be used as a sensitive probe of collisional damage in annealed amorphous silicon (for a more elaborate report of photocarrier-lifetime measurements in *a*-Si and *c*-Si, see Stolk *et al.*, 1992a and 1992b).

## 6.4 Discussion

### 6.4.1 Positron trapping at defects – qualitative

#### A. Networks and defects

The most obvious explanation of the present positron-annihilation data is in terms of structural defects acting as traps for the positrons. It is believed that amorphous silicon contains a wide variety of structural imperfections, including vacancy-type defects (Roorda *et al.*, 1990a and 1990b; Polman *et al.*, 1990; Coffa *et al.*, 1991). Starting from a (hypothetical) ‘defect’-free continuous random network (CRN), real amorphous silicon can be represented as a CRN with defects. These defects can be unique to the network (e.g., single dangling or floating bonds) or may be similar to point defects and small point-defect clusters in crystalline silicon (e.g., divacancies). In principle, both vacancy and interstitial-type defects may exist in amorphous silicon, but positron trapping is most likely to occur only at vacancy-type defects.

Structural defects in amorphous silicon are expected to be accompanied by a strain field, similar to that surrounding point defects in crystalline silicon. Differences in the defect population in the amorphous-silicon network are then thought to give rise to the variable short-range order or structural-relaxation phenomena. In addition, it is reasonable to expect that structural defects have dangling or highly strained bonds (or both) associated with them. These would give rise to band-gap states that are not necessarily unique for the CRN but similar to defects states in crystalline silicon.

Structural defects can be removed by thermal annealing, they can be generated by ion irradiation, and their electrical activity can be passivated by hydrogen. Such treatments are expected to modify the interaction of positrons with amorphous silicon because vacancy-type defects are known to act as traps for positrons. A high concentration of defects therefore reduces the positron diffusion length. Annealing or passivation is expected to lead to larger, and ion irradiation to smaller diffusion lengths. This is exactly what is observed in the figures 6.1 and 6.4.

In addition to changes in the positron diffusion length, changes in the bulk  $S$ -parameter are observed. When a distribution of defects is present, the measured  $S$ -parameter is the weighed average of the  $S$ -parameters characteristic to each of the defects [see equation (2.17) on page 43]. From the values of the diffusion length (see table 6.1) and based on the assumption that the positron diffusivity in amorphous silicon equals the one in crystalline silicon, it follows that the vast majority of the positrons are trapped. The fact that the  $S$ -parameter changes upon annealing would indicate that the distribution of defects changes. Some defect species anneal out but others remain.

## B. Other interpretations

Other interpretations of the positron-annihilation data are possible, some of which cannot be completely excluded.

The slope in the  $S(E)$ -curve may not be due solely to positron diffusion but to positron drift in an electric field (band bending) that might be present near the surface. Although in amorphous silicon such a field is not expected to penetrate far into the material (because of the high density of states in the gap), it may play a role in the case of crystalline silicon. This would make it difficult to quantify the present results (see the next section) but the qualitative conclusion that the trapping rate in amorphous silicon reduces upon annealing would still be valid.

Changes in the  $S$ -parameter could also be due to a change in density, especially in a covalently bonded material. However, it has been shown that though the density of a-Si prepared by ion implantation is 1.7 % less than that of c-Si, it does not change more than 0.1 % by thermal annealing up to temperatures of 580 °C (Custer *et al.*, 1990; Volkert and Polman, 1992). Such a density change is far too small to cause the changes observed in the  $S$ -parameter. Moreover, upon annealing amorphous silicon expands rather than contracts (Volkert and Polman, 1992), which would give rise to an increase in the  $S$ -parameter rather than a decrease.

An alternative scenario to explain both the change in the diffusion length and in the  $S$ -parameter induced by thermal annealing of amorphous silicon could be that the same number of defects are

present, but that the character of (some of) the defects changes. If, for example, some of the defects assume a positive charge state, positrons will be repelled and the trapping rate for that particular defect is strongly reduced (Puska *et al.*, 1990). In this context, it should be noted that free-carrier capture is to some extent analogous to the capture of positrons at defect centres. A reduction in the density of trapping (or recombination) centres has been observed by carrier-lifetime measurements (see figure 6.5), where the negatively charged electron is thought to be the main probe (the hole mobility is much smaller than the electron mobility). When both negatively and positively charged probes (i.e. electrons and positrons) experience a reduced decay rate, the most likely explanation is an actual reduction in the number of trapping sites.

#### 6.4.2 Positron trapping at defects – quantitative

In this section, we will try to obtain a quantitative estimate of the defect concentrations in the samples studied. Such an estimate requires knowledge of both the diffusivity of positrons in defect-free amorphous silicon and the positron trapping rate for trapping at the several possible defects (in every possible charge state). Neither is known and, therefore, we have to make some assumptions about these quantities, namely that they are equal (or at least similar) to the corresponding properties in crystalline silicon. Therefore, the assumptions have to be taken with some reserve.

The measured room-temperature values for the positron diffusivity in c-Si range from  $2.7 \times 10^{-4} \text{ m}^2\text{s}^{-1}$  to  $3.1 \times 10^{-4} \text{ m}^2\text{s}^{-1}$  (for references, see section 2.2.3). Positron trapping rates at defects are largely unknown, but some values have been reported for the neutral divacancy in c-Si. Calculations of trapping rates at single vacancies or multivacancy complexes have shown that the trapping rate does not depend very strongly on the size of the defect (Dlubek and Krause, 1987; Puska *et al.*, 1990). Therefore, we will use the divacancy trapping rate as a typical positron trapping rate in damaged silicon. Experimental values for the (transition-limited) specific trapping rate at the divacancy are of the order of  $\nu_t = 3 \times 10^{14} \text{ s}^{-1}$  (Shimotamai *et al.*, 1981; Dlubek and Krause, 1987; Motoko-Kwete *et al.*, 1989).

The concentration  $n_t$  of positron traps can be estimated from a comparison of the positron diffusion lengths  $L$  in crystalline and amorphous silicon using equation (4.7). The annihilation rate  $\lambda_b$  in trap-free a-Si is assumed to be equal to the one in c-Si. Using the above-mentioned values for the positron diffusivity and trapping rate, the trap density in *as-implanted* a-Si would correspond to 1.2 at.%, while the defect density in *annealed* a-Si is found to be 0.4 at.%. These values give some faith in the validity of the assumptions because they are in good agreement with estimates based on entirely different methods, namely calorimetry, Raman spectroscopy combined with Monte-Carlo damage calculations (Roorda *et al.*, 1991), and impurity-diffusion measurements (Coffa *et al.*, 1991).

The estimated defect densities in *as-implanted* and *annealed* amorphous silicon are consistent with the positron-annihilation measurements on annealed and re-implanted amorphous silicon. The minimum amount of ion damage that could be distinguished was of the order of  $10^{-3}$  at.fr. while the damage had saturated at an atomic fraction of several %.

### 6.4.3 Structural and electrical defects

Positrons are known to probe vacancy-like defects in both crystalline and amorphous metals and in crystalline semiconductors. It is not unreasonable, therefore, to expect that positrons probe vacancy-type defects in amorphous silicon as well. In the previous sections it has been argued that the results shown in figure 6.1 are indicative of a thermally induced removal of vacancy-type defects in amorphous silicon. The photocarrier-lifetime measurements (figures 6.5a and b) show that concurrent with the removal of vacancy-type defects, the number of band-gap states (e.g., dangling bonds) is strongly reduced. This already suggests that a correlation exists between structural and electrical defects in amorphous silicon.

The existence of such a relation is corroborated by the results on hydrogen-implanted amorphous silicon. Implantation of hydrogen and thermal annealing at 150°C leads to a reduced number of band-gap states as evidenced by the relatively long photocarrier lifetime in that material (see figure 6.5c). This result was not un-

expected because it has long been known that hydrogen passivates dangling bonds, thereby reducing the number of band-gap states. The positron-annihilation measurements on hydrogen implanted and 150 °C annealed a-Si indicate that the trapping of positrons is also affected. In that case, the anneal temperature is too low for any significant structural changes to occur. It appears, therefore, that some of the vacancy-type defects that were able to trap positrons no longer serve as such traps after the dangling bonds have been passivated with hydrogen. This suggests that (some of) the hydrogen atoms are now occupying the vacancies, which in turn means that (at least some of) the original dangling bonds were located at vacancy-type defects.

Although it is fully expected that the formation and removal of vacancy-type defects lead to the appearance and disappearance of dangling bonds, it is not easily shown experimentally. A spatial relation between defective bonds and radiation-damage sites in ion-bombarded amorphous silicon has previously been suggested to exist by Heidemann *et al.* (1984), who used ellipsometry of bevelled a-Si samples. Moreover, Coffa and Poate (1991), observed that hydrogen implanted into amorphous silicon leads to detrapping of metal impurities (Cu, Pd) that had previously been gettered in a defect-rich a-Si layer (hydrogen is more strongly bonded to the traps than copper or palladium). This suggests that the electrical defects are located at the same site as the structural defects that can trap metal atoms. It is concluded that the present data and the explanation presented in this chapter are consistent with these results, and can therefore be taken as additional evidence for the spatial correlation between structural and electrical defects in amorphous silicon. It appears that dangling bonds are associated with vacancy-type defects.

## 6.5 Conclusions

In summary, we have studied structural and electrical defects in amorphous silicon by positron-annihilation experiments and optically generated free-carrier-lifetime measurements. By making some bold assumptions on the behaviour of positrons in amorphous silicon (namely

that the positron diffusivity and the trapping rate of vacancy-type defects in amorphous silicon equal those in crystalline silicon), an estimate for the density of vacancy-type defects in amorphous silicon prepared by ion implantation can be obtained. This density would be about 1.2 at.%, and reduces to 0.4 at.% upon annealing at 500 °C. These values are in good agreement with several recent results based on entirely different observations, and may therefore serve as a justification for the assumptions mentioned above.

Concurrent with the apparent removal of vacancy-type defects from amorphous silicon by annealing at 500 °C, a tenfold increase in the lifetime of an optically generated free-carrier plasma is observed, suggesting a significant reduction in the number of band-gap states (e.g., dangling bonds). A large increase in the free-carrier lifetime has also been obtained by a low-temperature (150 °C) anneal, but with hydrogen post-implanted into the amorphous silicon. Such a low-temperature anneal (with post-implanted hydrogen) also leads to a reduction of the *S*-parameter similar to the decrease observed after a high-temperature anneal without hydrogen. This suggests that the band-gap states acting as trapping and recombination centres for free carriers are associated with the vacancy-type defects.

Finally, it has been found that both positron-annihilation and carrier-lifetime measurements are sensitive probes for ion-radiation damage in amorphous silicon annealed at 500 °C. When the estimated density of displaced atoms due to nuclear collisions approaches  $10^{-3}$ , both methods clearly detect a change. This suggests that the defect density in amorphous silicon annealed at 500 °C is not much higher than a few tenths of an at.%. Moreover, at an ion-damage level of several at.%, the damage saturates according to the positron-annihilation measurements, yielding an independent confirmation of the estimated defect density in *as-implanted* amorphous silicon.

NEXT PAGE(S) left BLANK.

# Chapter 7

## Amorphous silicon

### 7.1 Introduction

The present interest in amorphous silicon ( $a\text{-Si}$ ) dates back to the early sixties (see, e.g., Alvager and Hansen, 1962). Studies of its properties and behaviour upon various treatments have been carried out ever since. A new stimulus was given by the discovery that hydrogenated amorphous silicon ( $a\text{-Si:H}$ ) showed semiconducting properties and could be used as a semiconductor in devices (Spear and Lecomber, 1975). Although  $a\text{-Si:H}$  differs in many respects from its ‘clean’ counterpart  $a\text{-Si}$ , fundamental questions concerning the atomic structure are similar for the two types of material (Roorda, 1990).

The short-range order of amorphous silicon has been the subject of much research since it was generally believed that ordered networks are essential for sharp band tails and low ‘defect’ concentrations. Besides this, the role of hydrogen is still a key topic in the research of  $a\text{-Si:H}$ . The technological promise of large-area device arrays on inexpensive glass substrates continues to drive intensive efforts to better understand the electronic and material properties of amorphous silicon (Winer, 1991).

Since not all silicon atoms in amorphous silicon are tetrahedrally bonded, the material contains unpaired electrons in nonbonding orbitals, called ‘dangling bonds’, which limit the conductivity of amorphous silicon by trapping electrons. Moreover, fivefold-coordinated

bonds may be present in amorphous silicon, called 'floating bonds' (Pantelides, 1986). The existence of floating bonds has been a subject of debate (Phillips, 1987), but is now supported by molecular dynamics simulations of melt-quenched silicon (Car and Parinello, 1988). Hydrogenating amorphous silicon by  $\sim 10$  at.% reduces the dangling-bond concentration from  $\sim 10^{20} \text{ cm}^{-3}$  (one dangling bond for every  $\sim 500$  Si atoms) to somewhere between  $10^{15}$  and  $10^{16} \text{ cm}^{-3}$  (Street, 1991a).

Hydrogen is known to be mobile in amorphous silicon at moderate temperatures ( $\sim 150^\circ\text{C}$ ), although the diffusion coefficient in  $a\text{-Si:H}$  is time-dependent, which is partly due to trapping of hydrogen in microvoids (Scher and Montroll, 1975; Kakalios *et al.*, 1987; Shinar *et al.*, 1989; Van den Boogaard *et al.*, 1992). Besides, hydrogenated amorphous silicon is metastable. At temperatures exceeding  $150^\circ\text{C}$  the diffusion of hydrogen induces structural changes while the material approaches equilibrium (Jones, 1991; Street, 1991b).

In amorphous silicon the presence of microscopic voids plays an important role. Large voids are sometimes present in low-temperature deposited amorphous-silicon films (Brodsky *et al.*, 1970; Thomas *et al.*, 1978; Saitoh *et al.*, 1981; Sinke *et al.*, 1988). These voids affect on the one hand certain electrical properties of amorphous semiconductors (Bean and Poate, 1980) while on the other hand, voids appear to inhibit the diffusion of atomic hydrogen in  $a\text{-Si:H}$  (Mittra *et al.*, 1989 and 1990) but serve as a medium for the rapid desorption of molecular hydrogen (Beyer, 1991).

Low-energy ion bombardment (krypton) can be employed to assist and control silicon-film growth (Tsai *et al.*, 1990). In sputter deposition a negative bias at the substrate causes a considerable flux of low-energy krypton atoms hitting the growing film. In ion-assisted molecular beam epitaxy (MBE) an extra ion gun can provide the required ions. Beneficial effects on the growth process have been reported by, e.g., Ohmi *et al.* (1991), who found growth of homoepitaxial silicon films at a lower temperature than with conventional thermal molecular beam epitaxy (MBE). Chapman (1980) has reviewed the early work on thin film growth by inert-gas sputtering, while the basic incorporation processes of inert-gas atoms in metals and silicon have been reviewed by Van Veen (1986 and 1991).

This chapter describes positron-annihilation measurements on three types of amorphous silicon, viz. krypton-sputtered a-Si, plasma-enhanced chemical-vapour deposited a-Si, and a-Si grown in an molecular-beam epitaxy system at a low deposition temperature. Additionally, chapter 6 has dealt with a fourth species, namely ion-beam amorphized silicon. The first kind of amorphous silicon has a high concentration of krypton (a-Si:Kr), the second a high concentration of hydrogen (a-Si:H), while samples prepared in the third way are free of foreign atoms but contain large voids.

## 7.2 Sample preparation

Three different types of amorphous silicon have been examined, viz. krypton-sputtered a-Si, plasma-enhanced chemical-vapour deposited (PECVD) a-Si and a-Si grown in a molecular-beam epitaxy (MBE) system.

Krypton-sputtered amorphous-silicon films were prepared by sputtering of silicon in a low-pressure (0.01–0.1 Pa) krypton plasma, as described by Van Veen (1986). In order to enable the incorporation of inert-gas ions, the substrate was at a negative bias with respect to the plasma. The thickness of the sputtered layer was monitored with the aid of a quartz-crystal microbalance and calibrated by weighing the deposited films. For our experiments a-Si:Kr films with an area of  $10 \times 10 \text{ mm}^2$  were deposited on a Si(100) wafer at a temperature of  $310^\circ\text{C}$  and a substrate bias of  $-50 \text{ V}$ , using a silicon-target potential of  $-1.5 \text{ kV}$ . By varying the duty cycle of the pulsation of the substrate potential between 1 and 100 %, the krypton flux could be varied between  $4.4 \times 10^{14}$  and  $4.4 \times 10^{16} \text{ cm}^{-2}\text{s}^{-1}$ . The silicon flux at the substrate was on the average  $4 \times 10^{15} \text{ cm}^{-2}\text{s}^{-1}$ . In this way several films were deposited with an average thickness of  $6 \mu\text{m}$  but with different krypton concentrations (for the influence of the deposition parameters on the film characteristics, see Van Veen *et al.*, 1992). The six samples are labelled SiKrx with  $x$  ranging from 1 to 6.

The krypton concentrations in the film have been measured by means of X-ray analysis (see Greuter *et al.*, 1992), while Mössbauer spectroscopy was applied to probe the local environment of the in-

corporated krypton (see Greuter *et al.*, 1991). Cross-sectional high-resolution Transmission Electron Microscopy (TEM) pictures on samples with a duty cycle of 30 % (see figure 7.1) show the alternating layers with high and low krypton concentrations in the film (for the procedure, see Greuter, 1993, and Greuter *et al.*, 1993). The formation of the sub-layers shown in figure 7.1 originates from the process conditions during deposition. While silicon is continuously sputtered at a rate of  $0.65 \pm 0.1$  nm/s, the krypton is injected in cycles of 0.5 Hz (30 % duty cycle). According to TRIM calculations (Ziegler *et al.*, 1985), the range of 50 eV krypton in silicon amounts to only 1 nm. Assuming the krypton atoms are immediately frozen in the structure, this processing technique results in the formation of layers with alternating low and high krypton concentrations with a period of  $1.3 \pm 0.2$  nm, in agreement with the period shown in the TEM micrograph (figure 7.1). The stress in krypton-sputtered a-Si films is rather large. From monitoring the wafer bending with an optical microscope the uniform stress was estimated to be  $\sim 0.34$  GPa. From this value the hydrostatic pressure in the small krypton agglomerates could be derived, which amounts to  $\sim 3.9$  GPa (Greuter *et al.*, 1993).

The second type of amorphous silicon was deposited in a PECVD process from a 1:1-volume-ratio mixture of  $\text{SiH}_4$  and  $\text{H}_2$  at substrate temperatures  $T_s$  of 50, 100, 150, and 200 °C, and from undiluted  $\text{SiH}_4$  at 50 and 200 °C. The substrates were thermally oxidized crystalline-silicon wafers (Wacker-Chemitronic, Burghausen, Germany). The thickness of the silicon-dioxide layer was 220 nm, while the a-Si:H film itself was approximately 1  $\mu\text{m}$  thick. The power densities in the 13.56 MHz plasma were  $38 \text{ mWcm}^{-3}$  and  $13 \text{ mWcm}^{-3}$  respectively for the deposition from  $\text{H}_2$ -diluted and undiluted  $\text{SiH}_4$ , yielding comparable deposition rates of  $\sim 0.15 \text{ nm s}^{-1}$  at  $T_s = 200$  °C. The samples are described in more detail elsewhere (Van den Boogaard, 1992).

The third species of examined amorphous silicon was a-Si made in an MBE system. After standard RCA cleaning of a Si(100) wafer (B-dope,  $0.01 \Omega\text{cm}$ ), 30 Å  $\text{SiO}_2$  was chemically grown. In the MBE-system this oxide was removed by an anneal at 850 °C and  $10^{-11}$  Torr. The first 10 nm silicon was grown at room temperature in order to get an amorphous layer, followed by 300 nm deposited at 250 °C. The sample underwent an anneal at 350 °C for 30 minutes. Sam-

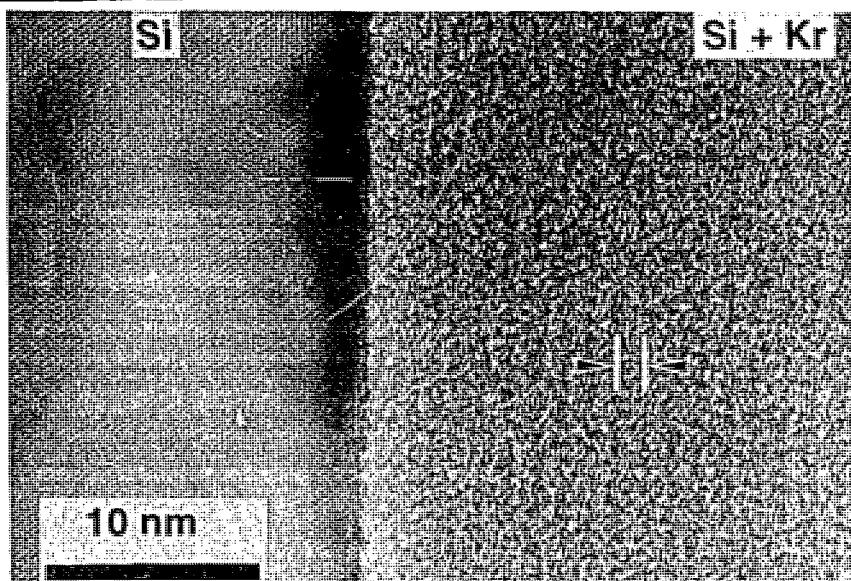


*Figure 7.1:* Cross-sectional TEM micrograph of a a-Si:Kr film (right) and the crystalline silicon substrate in the [110] orientation (left). The amorphous layer shows sub-layers with alternating dark and bright contrast (with a period of 1.3 nm), that are interpreted to represent regions with high and low krypton concentrations respectively (from Greuter *et al.*, 1993).

ples prepared under these conditions are expected to be amorphous (Jork *et al.*, 1989; Eaglesham *et al.*, 1990). Although Perovic *et al.* (1991) have grown epitaxial silicon layers at 300 °C much thicker than predicted by the above-mentioned authors, our room-temperature growth step guarantees a completely amorphous layer, which has been confirmed by Raman spectroscopy (see below). The spectrum indicates that at least 99 % of our MBE-deposited film is amorphous.

The krypton-sputtered amorphous-silicon samples have been examined by positron-annihilation and Raman measurements (see section 3.3.2). After the Raman measurements the samples have been annealed at 310 °C and 480 °C for 2 hours and re-measured in order to study the relaxation. The hydrogenated amorphous-silicon films have been subjected to positron-annihilation measurements, while samples grown under similar conditions on glass substrates were subjected to Small-Angle X-Ray Scattering experiments (SAXS; see section 3.3.3). Finally, the MBE-system grown amorphous-silicon film has been ex-

amined with both positron annihilation and Raman spectroscopy.

Values for the  $S$ -parameter and the positron diffusion length have been extracted from the positron data by means of the computer code VEPFIT. We realize that the value of the diffusion length is influenced by epithermal positron effects (compare section 2.2.6), but our main concern lies in analysing series of samples that show only small differences. It is expected that epithermal positron behaviour is identical in all samples of such a series, so that the different annihilation characteristics may be attributed principally to the material quality. Further, all positron  $S$ -parameters have been normalized with respect to the value for c-Si, according to equation (2.16) on page 41.

## 7.3 Results

### 7.3.1 Krypton-sputtered and MBE-system grown amorphous silicon

The results of the positron-annihilation experiments on krypton-sputtered and MBE-system grown amorphous-silicon films are shown in figures 7.2 and 7.3. The Raman spectra are shown in figure 7.4. The fitted  $S$ -parameters, diffusion lengths and normalized Raman TO-peak widths ( $hwhm$ ) are presented in table 7.1. In addition, results of the Raman measurements of the samples after the 310 °C and 480 °C anneals and the krypton concentrations in the films are also listed. The results for the  $a$ -Si:Kr samples are plotted as a function of the krypton concentration in figure 7.5.

The  $S$ -parameter of MBE-system grown  $a$ -Si is very high (1.145), while the positron diffusion length is rather small (5.4 nm). The  $S$ -parameter of krypton-sputtered  $a$ -Si ranges almost linearly from 1.024 for low krypton concentrations (0.5–1 at.%) to 1.018 for high concentrations (4–5 at.%). The positron diffusion length in the latter  $a$ -Si:Kr films is significantly lower than in the films with a low krypton concentration. The width of the TO-peak of the Raman measurements increases for higher krypton concentrations. The anneals at 310 °C and 480 °C lead to an overall lowering of the TO-peak width of about  $1.5 \text{ cm}^{-1}$  for each anneal. We emphasize that the TO-peak

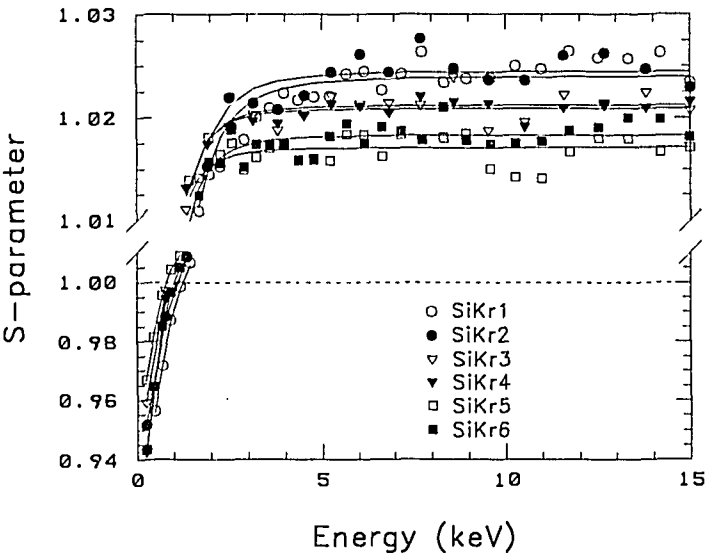


Figure 7.2: Positron-annihilation measurements on the krypton-sputtered amorphous-silicon films. The six samples are labelled SiKr1-SiKr6.

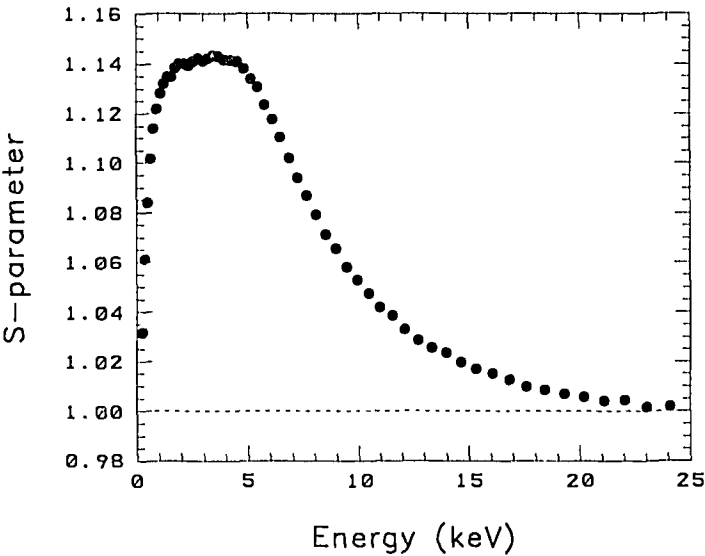


Figure 7.3: Positron-annihilation measurements on MBE-system grown amorphous silicon.

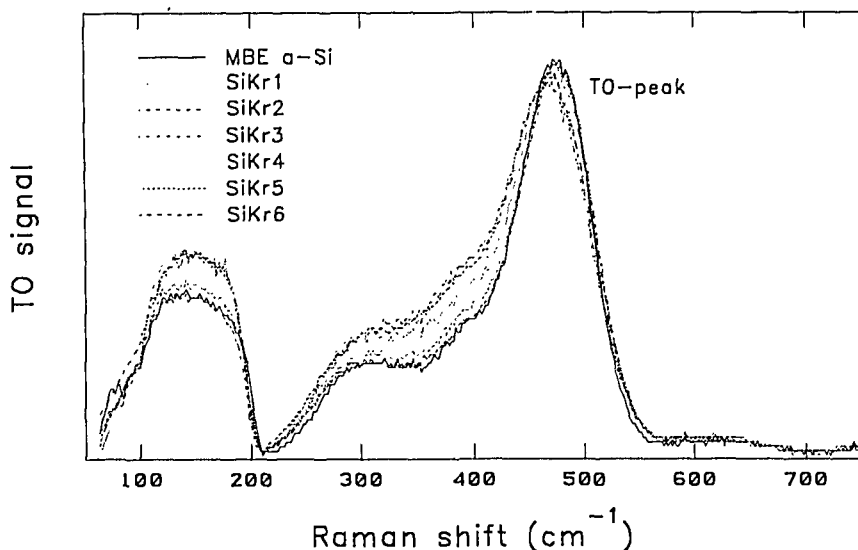


Figure 7.4: Raman spectra of the six krypton-sputtered a-Si samples (labelled SiKr1–SiKr6) and the MBE-system grown a-Si film.

Table 7.1: Fit results of the positron-annihilation and Raman measurements for krypton-sputtered and MBE-system grown a-Si in its *as-deposited* state and after a 310 °C and 480 °C anneal (only Raman measurements). *S* and *L* denote the *S*-parameter and the positron diffusion length respectively. For reference, the values for a-Si prepared by ion-implantation are also given (see chapter 6).

sample	Kr conc.	<i>S</i> ( $\pm 5 \times 10^{-4}$ )	<i>L</i> (nm) ( $\pm 0.5$ )	<i>hwhm</i> TO-peak (cm <sup>-1</sup> ) ( $\pm 0.4$ )		
				<i>as-dep.</i>	310 °C	480 °C
SiKr1	0.55 %	1.0240	13.8	38.5	36.8	35.4
SiKr2	1.0 %	1.0244	12.6	39.5	37.6	36.5
SiKr3	2.7 %	1.0213	8.7	41.9	40.6	38.0
SiKr4	3.0 %	1.0209	7.0	42.9	41.7	40.2
SiKr5	3.9 %	1.0170	7.1	43.2	41.3	39.2
SiKr6	4.8 %	1.0183	8.0	43.5	42.6	40.5
‘MBE’ a-Si	—	1.1450	5.4	37.2	35.6	34.0
as-impl. a-Si	—	1.0379	8.6	—	37.3	35.1

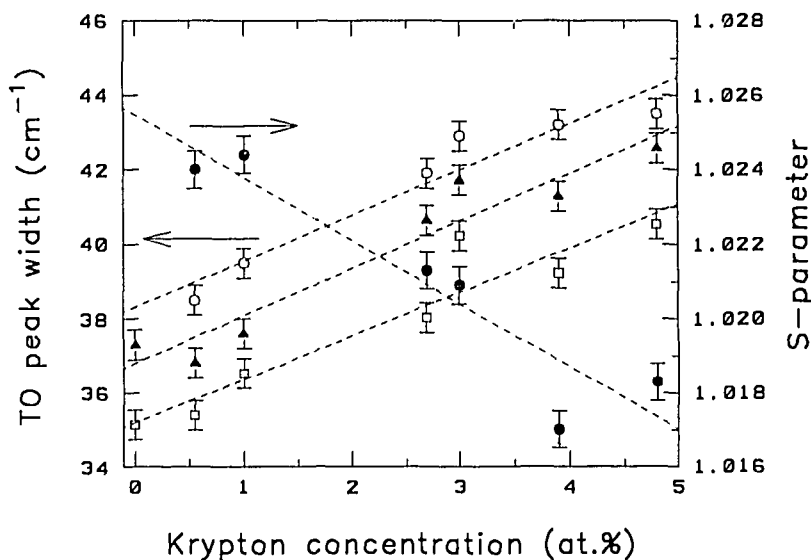


Figure 7.5:  $S$ -parameter (●) and TO-peak width (○) of the  $a$ -Si:Kr films as a function of the krypton concentration. The widths of the TO-peak after relaxation at 310 °C (▲) and 480 °C (□) are also plotted. The data for 0% krypton indicate the TO-peak widths of ion-beam amorphized silicon relaxed at 310 °C, and 480 °C, respectively. The dashed lines are to guide the eye.

width of amorphous silicon annealed at 310 °C, extrapolated to 0% krypton, lies close to the value for the ion-beam amorphized silicon discussed in chapter 6, annealed at 310 °C (see figure 7.5), of which the measured value [ $37.3(4) \text{ cm}^{-1}$ ] is in agreement with the literature (Roorda *et al.*, 1991).

### 7.3.2 Hydrogenated amorphous silicon

The results of the Doppler-broadening measurements on the hydrogenated amorphous silicon, deposited in a PECVD process either from a 1:1-volume-ratio mixture of  $\text{SiH}_4$  and  $\text{H}_2$  at temperatures ranging from 50 to 200 °C or from undiluted  $\text{H}_2$  at 50 or 200 °C, are shown in figure 7.6. SAXS spectra of a series of PECVD samples are shown in figure 7.7. As outlined in section 3.3.3, the Guinier plots of figure 7.7a and b can be used to determine, for each sample, the

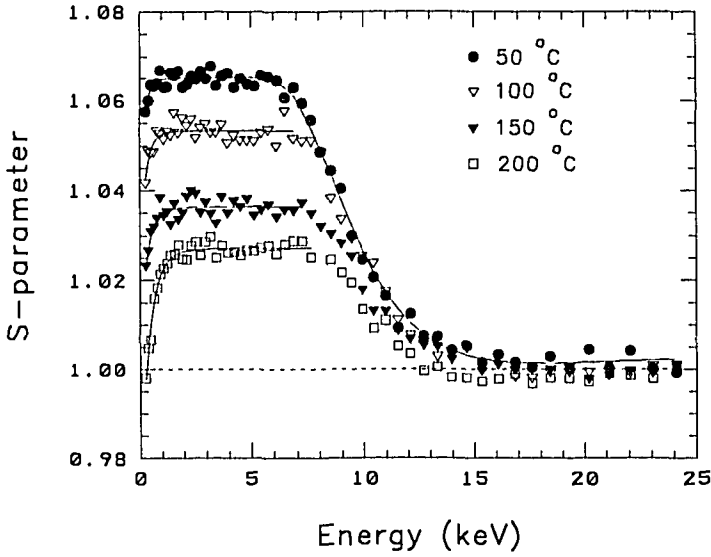
Table 7.2: Fit results for the  $S$ -parameters and diffusion lengths ( $L$ ) from the positron-annihilation measurements on the a-Si:H samples, and the radius of gyration of the voids ( $R_g$ ) and void fraction ( $v_f$ ) derived from the SAXS data.  $T_s$  is the substrate temperature during deposition.

growth conditions		$S$	$L$ (nm)	$R_g$ (nm)	$v_f$
gases	$T_s$	( $\pm 5 \times 10^{-4}$ )	( $\pm 0.6$ )		
SiH <sub>4</sub>	50 °C	1.0662	3.0	0.65	0.2521
SiH <sub>4</sub>	100 °C	...	...	0.59	0.1002
SiH <sub>4</sub>	200 °C	1.0327	5.0	0.54	0.0239
SiH <sub>4</sub> /H <sub>2</sub>	50 °C	1.0651	2.4	0.59	0.1168
SiH <sub>4</sub> /H <sub>2</sub>	83 °C	...	...	0.57	0.0679
SiH <sub>4</sub> /H <sub>2</sub>	100 °C	1.0534	2.4	...	...
SiH <sub>4</sub> /H <sub>2</sub>	125 °C	...	...	0.57	0.0447
SiH <sub>4</sub> /H <sub>2</sub>	150 °C	1.0364	3.3	0.52	0.0274
SiH <sub>4</sub> /H <sub>2</sub>	200 °C	1.0273	6.2	0.48	0.0167

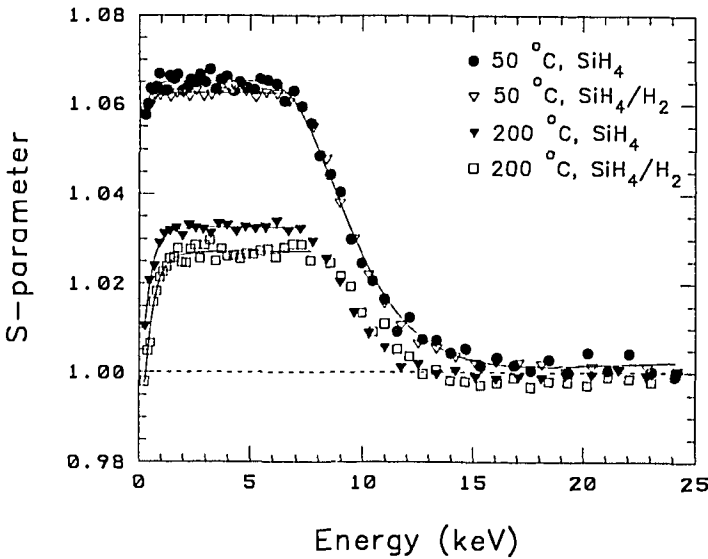
radius of gyration  $R_g$  of the voids causing the scattering. From a plot of  $hJ(h)$  versus  $h$ , as in figures 7.7c and d, the void fraction can be derived [see equation (3.3) on page 66 and see below]. The results of these calculations are listed in table 7.2.

As shown in figure 7.6, an increase of the deposition temperature leads to a decrease of the  $S$ -parameter and an increase of the positron diffusion length. Moreover, layers grown from undiluted SiH<sub>4</sub> have a higher  $S$ -parameter than layers grown from the SiH<sub>4</sub>/H<sub>2</sub> mixture. The tabulated results for  $R_g$  and  $v_f$  (table 7.2) show a decrease of the radius of gyration and void fraction for increasing deposition temperatures, while films grown from undiluted SiH<sub>4</sub> have both larger voids (larger  $R_g$ ) and a higher void fraction.

It should be noted that it is difficult to correctly estimate the angular range for which Guinier's law [equation (3.5) on page 66] holds for a line-collimation geometry. For most samples the shape of the spectrum suggests that the Guinier approximation is valid for values of  $h$  that are considerably larger than the theoretical limit,  $hR_g \lesssim 1.2$ . However, due to polydispersity, the fact that the voids do not all have the same size (Williamson *et al.*, 1989), the average radius of gyration may be overestimated significantly. If a distribution of voids has a



(a)



(b)

Figure 7.6: Positron-annihilation measurements on PECVD-grown hydrogenated amorphous silicon. *a.* deposition from a 1:1 mixture of  $\text{SiH}_4/\text{H}_2$  at 50, 100, 150, and 200 °C; *b.* deposition from the  $\text{SiH}_4/\text{H}_2$  mixture and from undiluted  $\text{SiH}_4$  at 50 and 200 °C.

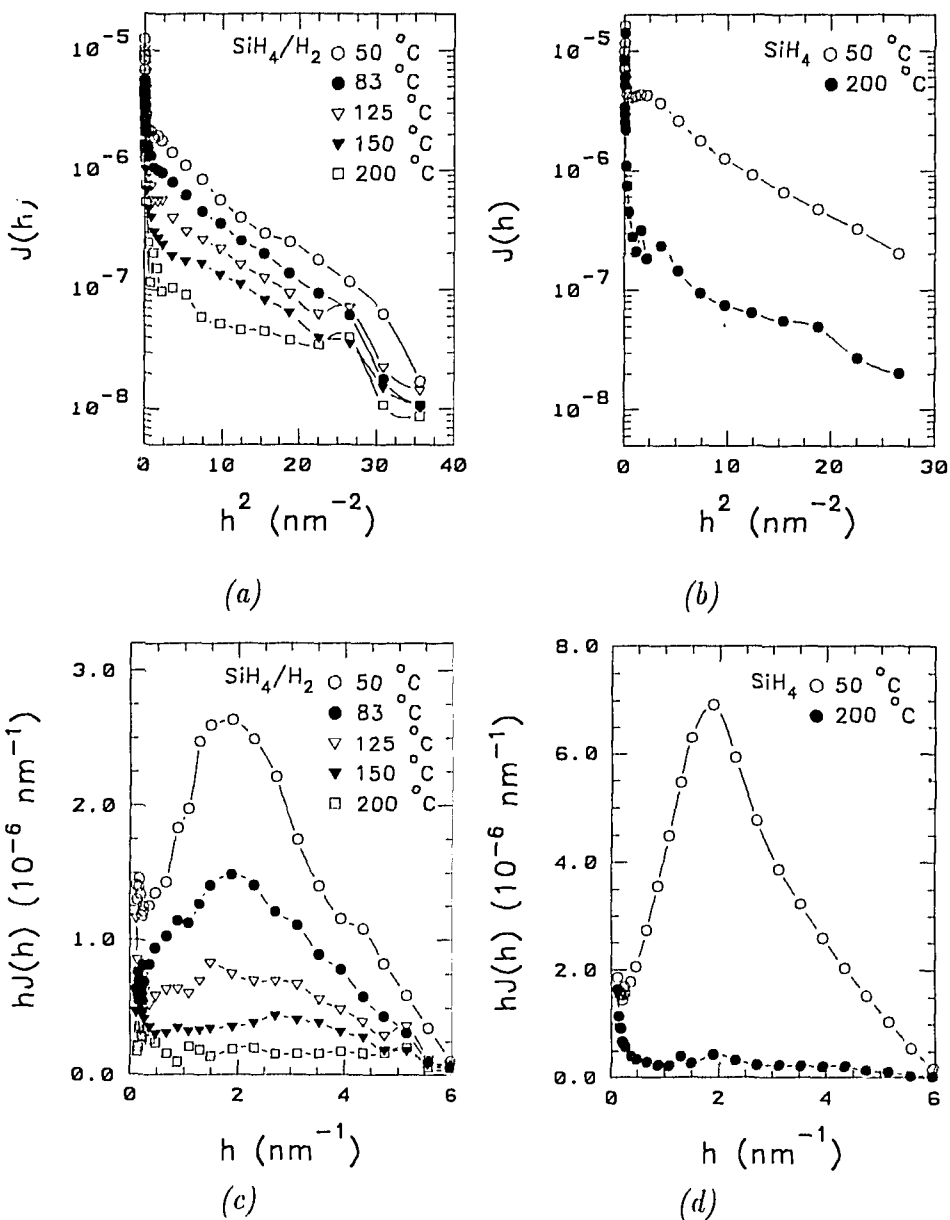


Figure 7.7: SAXS data for the  $\alpha$ -Si:H samples deposited at the indicated temperatures either from a 1:1  $\text{SiH}_4/\text{H}_2$  mixture (left) or from undiluted  $\text{SiH}_4$  (right). a. and b. are Guinier plots, c. and d. plots of  $hJ(h)$  versus  $h$ .

standard deviation of 25 %, the average  $R_g$  is  $\sim 25$  % smaller than estimated by equation (3.5) (Gerritsen and Robertus, 1990).

For the calculation of the void fraction in the a-Si:H layers [equation (3.3)], the contributions by hydrogen in the bulk to the scattering and absorption of X-rays are negligible to those of silicon. Therefore, we have assumed, for the calculation of  $v_f$ , that the bulk consists only of silicon. The void fractions in table 7.2 are calculated with a value for the mass absorption coefficient for  $\text{CuK}\alpha$  radiation,  $\mu_m$ , of  $61.1 \text{ cm}^2\text{g}^{-1}$ , and for the difference between the electron density in the bulk and that in the void,  $\Delta\rho$ , a value of  $7 \times 10^{23} \text{ cm}^{-3}$  (i.e.  $14$  [electrons per silicon atom]  $\times 4.9 \times 10^{22} \text{ cm}^{-3}$  [density of silicon atoms]).

## 7.4 Discussion

### 7.4.1 Krypton-sputtered amorphous silicon

The higher the krypton concentration in the amorphous-silicon films, the lower the  $S$ -parameter and the shorter the diffusion lengths. Apparently, the number of positron traps increases (shorter diffusion length), although their character changes (lower  $S$ -value).

These results can be explained in the following way. Sputtered amorphous-silicon films contain, just like ion-beam amorphized silicon, built-in vacancy-type defects, i.e. positron traps leading to higher  $S$ -values. From the low value of the  $S$ -parameter ( $\sim 1.02$ ) it can be concluded that these vacancy complexes are only very small, i.e. their sizes correspond to mono- or divacancies in crystalline silicon, since divacancies in c-Si have an  $S$ -value of  $\sim 1.035$  (Simpson *et al.*, 1990). During the sputtering process, the 50 eV krypton creates silicon self-interstitials, which fill these grown-in vacancy-type defects, thereby reducing their size. Meanwhile, the electrically inactive krypton atoms themselves fill the positron traps. Both effects result in a denser amorphous-silicon film for higher krypton concentrations, corresponding to a steady lowering of the  $S$ -parameter. Interestingly, the decrease of the diffusion length evidences more positron traps in the cases of high krypton concentrations. Although the krypton atoms

and the silicon self-interstitials have completely occupied the vacancies in the material, the oversized krypton atoms probably induce the creation of smaller positron traps due to the straining of the lattice (compare the results on helium-implanted silicon in section 5.4).

This explanation is consistent with the Raman measurements, which show that the *hwhm* of the TO-peak increases from  $38.5 \text{ cm}^{-1}$  for *a*-Si with 0.55 % Kr to  $43.5 \text{ cm}^{-1}$  for *a*-Si with 4.8 % Kr. It follows from equation (3.2) on page 65 that the rms bond-angle deviation  $\Delta\theta_b$  changes from  $10.3^\circ$  (0.55 % Kr) to  $12.0^\circ$  (4.8 % Kr). This shows that an increase in the krypton concentration corresponds to a decrease in the short-range order. As a reference, MBE-system grown amorphous silicon has a TO-peak width of  $37.2 \text{ cm}^{-1}$  (corresponding to an rms bond-angle distortion of  $9.9^\circ$ ), while it contains large voids. We conclude that the krypton incorporation in the lattice leads to large local strains, which induce both a large bond-angle distortion (accounting for the Raman data) and a decrease in the short-range order. The latter may imply more (small) positron traps and therefore explains the shortening of the positron diffusion length.

The agreement between the value of the TO-peak width for Kr-sputtered *a*-Si films extrapolated to 0 % krypton and ion-beam amorphized silicon, both relaxed at  $310^\circ\text{C}$ , and the similar agreement after relaxation at  $480^\circ\text{C}$  (see figure 7.5), suggest that the structures of *a*-Si made by ion-assisted deposition and by ion implantation are very similar when compared at the same temperature (Greuter *et al.*, 1992). The absence of such a correlation for the *S*-parameter values (ion-beam amorphous silicon has *S*-values of 1.0379 and 1.0257 in its *as-deposited* state and after a  $500^\circ\text{C}$  anneal [see table 6.1]) is easily explained: Raman spectroscopy is used to detect lattice vibrations but positrons probe open-volume defects. Due to the extreme sensitivity of the positron-annihilation peak width to the annihilation site, the difference between small vacancy-type defects filled with krypton atoms (in case of *a*-Si:Kr) and empty vacancy-type defects may lead to *S*-values that differ considerably, while the TO-peak width in the Raman spectrum is unaltered.

Following the procedure outlined in section 6.4.2 it is possible to estimate the concentration of positron traps. Assuming the divacancy trapping rate  $\nu_t = 3 \times 10^{14} \text{ s}^{-1}$  to be a typical trapping rate

for damaged silicon, equation (4.7) [see page 85] yields  $5 \times 10^{-3}$ , and  $1.5 \times 10^{-2}$  as fractional defect concentrations for krypton-sputtered a-Si with  $5.5 \times 10^{-3}$  and  $4.8 \times 10^{-2}$  at.fr. krypton, respectively. Clearly, for a higher krypton concentration not every krypton atom serves as a positron trap. Due to the high concentration it is reasonable to assume that the krypton atoms are clustered, each cluster acting as one trap. For lower concentrations probably every single incorporated krypton atom is related to a positron trap.

### 7.4.2 MBE-system grown amorphous silicon

The high measured  $S$ -parameter of MBE-system deposited amorphous silicon (1.145) is in accordance with the value of 1.15 that Simpson *et al.* (1990) found for MBE silicon, grown on Si(100) at a temperature just below 260°C. They interpreted the high  $S$ -parameter by trapping in large voids so that the narrow lineshapes are due to either positronium formation inside these voids, or positron trapping in a positronium-like state on their inner surfaces. TEM micrographs revealed voids of 3 to 6 nm diameter in the silicon epilayer. Further TEM work showed linear arrays of these spherical defects aligned parallel to the [100] growth direction. These arrays extended from the epitaxial film into the amorphous region (Perovic *et al.*, 1991; Jackman *et al.*, 1992). It was concluded that the measured high  $S$ -parameter originated from positron trapping in the microvoids. It is known that positrons are indeed very sensitive to open-volume defects in silicon (Schut *et al.*, 1991).

However, slow-positron lifetime measurements on these samples showed that the intensity of the void-related component was too low to account for the saturation trapping in the Doppler-broadening experiments (Britton *et al.*, 1992). On the other hand, there was evidence of a bulk-like trapped positron state of unknown origin (possibly related to oxygen complexes) in the MBE layer. In order to get the high  $S$ -parameter with non-saturated positron trapping in the voids, the authors concluded that the annihilation lineshape of positrons trapped in voids is extremely narrow, and the momentum of the annihilating pair negligible.

Gossmann *et al.* (1992) have examined silicon epilayers grown

by MBE at several temperatures. Rapid thermal anneals (RTA) at 450°C or a higher temperature led to a decrease of the defect concentration in their layers deposited at 220°C. The high  $S$ -parameter ( $> 1.07$  after RTA at 450°C) was reduced by an RTA at 600°C to below 1.01. The authors noted that the quality of the grown layers heavily depends on the substrate-cleaning technique before growth (compare also Asoka-Kumar *et al.*, 1993)..

In our opinion, the only adequate explanation of the  $S$ -value of our MBE-system grown amorphous silicon (1.145) involves positronium formation in the microvoids. Britton *et al.* (1992) have shown that even in the case of saturated trapping not all positrons annihilate in the microvoid. Therefore, the measured high  $S$ -parameter must be due to (almost) zero-momentum annihilations. The only possibility is  $p$ -Ps annihilation from a positronium bound state, either free or localized at the inner surface of the void. Britton *et al.* (1992) have measured a lifetime related to the annihilation in the voids of 500 ps, which is too short for free positronium annihilation but long enough for annihilation from a positronium-like state (Dupasquier, 1983; Hasegawa *et al.*, 1989). This topic will be discussed further in section 7.4.3.

The diffusion length in the MBE-grown a-Si film is rather small (5.4 nm), indicating poor-quality material, although it is not so small as in some of the PECVD a-Si layers. The rather small bond-angle distortion derived from the Raman measurements (9.9°) contrasts with the higher values for krypton-sputtered a-Si. The lower value may be due to the absence of foreign atoms straining the lattice.

### 7.4.3 Hydrogenated amorphous silicon

#### Positronium formation in voids

The  $S$ -parameter measured for the hydrogenated amorphous-silicon films decreases with increasing deposition temperature (see figure 7.6). Especially the samples grown at 50°C show a relatively high  $S$ -parameter of  $\sim 1.065$ . Since  $S$ -values for small vacancy-type defects in silicon lie in the range from 1.03 to 1.04 (compare table 7.3), we are inclined to explain the high  $S$ -parameter by positronium formation

Table 7.3:  $S$ -parameters derived from literature for open-volume defects in silicon. The values are normalized according to equation (2.16). The mentioned defect types refer to the positron traps to which the authors ascribe the observed value of the  $S$ -parameter. Most (but not all)  $S$ -values have either been extracted from saturated positron trapping data or from fitting the  $S$ -parameter.

sample material	defect-type	$S$	reference
c-Si	vacancy-type defects	1.035	Simpson <i>et al.</i> , 1990
c-Si	vacancy-type defects	1.042	Mitchell <i>et al.</i> , 1990
c-Si	divacancies	1.034	Keinonen <i>et al.</i> , 1988
c-Si	divacancies	1.038	J. Mäkinen <i>et al.</i> , 1990a
n-Si on Si	mono- or divacancies	1.030	Jackman <i>et al.</i> , 1989
MBE Si	voids	1.15	Simpson <i>et al.</i> , 1990
evaporated a-Si	amorphous layer	1.020	Leo <i>et al.</i> , 1981
a-Si	amorphous layer	1.04	Simpson <i>et al.</i> , 1990
a-Si:H	amorphous layer	1.007	Leo <i>et al.</i> , 1981
a-Si:H (30 °C)	amorphous layer	1.056	Nasu <i>et al.</i> , 1987
a-Si:H (250 °C)	amorphous layer	1.043	Nasu <i>et al.</i> , 1987
B-implanted c-Si	vacancy clusters	1.047	Uedono <i>et al.</i> , 1991b
As-implanted c-Si	vacancy clusters	1.048	Uedono <i>et al.</i> , 1991b
P-implanted c-Si	amorphous layer	1.021	Hautojärvi <i>et al.</i> , 1988
P-implanted c-Si	vacancy clusters	1.061	Uedono <i>et al.</i> , 1991b
As-doped Si	As-vacancy complexes or small As clusters	1.00	Jackman <i>et al.</i> , 1989
Cz Si	oxygen-vacancy complexes	0.978	Dannefaer and Kerr, 1986
Si on c-Si	oxygen-related defects	0.93	Schultz <i>et al.</i> , 1988a; Tandberg <i>et al.</i> , 1989
$p^+$ -Si on Cz Si	$\text{SiO}_{1.75}$ precipitates	0.90	Coleman <i>et al.</i> , 1990

and annihilation (see section 1.2.3). In section 7.4.4 a model for positronium in cavities will be presented which might support the experimental results found for both the micro-cavities in the hydrogenated amorphous silicon of this chapter and the cavities produced by helium irradiation and thermal helium release of chapter 5.

In our opinion, the  $S$ -values exceeding 1.06 can only be explained by assuming zero-momentum annihilation of para-positronium ( $p$ -Ps) in (large) voids. The energy distribution of the  $\gamma$ -photons created during the decay of  $p$ -Ps is so narrow that the width of their contribution

is determined solely by the detector resolution. The resolution ( $fwhm$ ) of the germanium solid-state detector used for these experiments is 1.2 keV at 511 keV, corresponding to a normalized  $S$ -parameter of  $\sim 1.55$ . The  $S$ -parameter for  $o$ -Ps annihilations will be approximately equal to the one for normal positron annihilations in the same trap (in matter  $o$ -Ps annihilates predominantly via electron *pick-off* [spin-exchange] reactions), for which we take the divacancy  $S$ -parameter of 1.035 as a representative value. The effective  $S$ -parameter for positronium decay (only in matter!),  $S_{Ps}$ , is now the weighed average of the values for  $o$ -Ps and  $p$ -Ps, 1.035 and 1.55 respectively. Since 25 % of the positronium is formed as  $p$ -Ps, we find  $S_{Ps} \approx 1.16$ . Energetically, positronium formation is possible at a silicon surface, since the positronium workfunction  $\phi_{Ps}$  [see equation (2.12) on page 39] lies around -2 eV (Schultz and Lynn, 1988).

There is evidence for positronium formation in the voids in  $a$ -Si:H in literature. 2D-ACAR experiments revealed positronium formation in rf-sputter-deposited  $a$ -Si:H (He *et al.*, 1986), while it has been observed in PECVD  $a$ -Si:H via both 2D-ACAR and lifetime measurements (Bhide *et al.*, 1987; Suzuki *et al.*, 1991). Schaefer *et al.* (1986) have attributed a lifetime of 402 ps in their experiments to positron annihilation in voids containing 10–15 vacancies, whereas a lifetime of 1.8 ns was associated with  $o$ -Ps decay in even larger voids, which SAXS results suggest exist in material deposited at a low temperature (Mahan *et al.*, 1991). It should be noted that the long lifetime in lifetime measurements stems from  $o$ -Ps while the high  $S$ -parameter in Doppler experiments comes from  $p$ -Ps. However, the formation probabilities of the two types of positronium are related as 3:1 on quantum mechanical grounds. Since  $o$ -Ps annihilates predominantly after an electron *pick-off* reaction, the measured lifetime associated with positronium annihilation in voids may therefore be only slightly longer than the lifetime of trapped positrons, i.e. a lifetime of 500 ps suffices for positronium annihilation.

Finally, we have to address the question whether positronium formation is the only adequate explanation for the observed high  $S$ -parameter. Is it possible that the annihilation of unbound positrons yields such a high  $S$ -value? Annihilation from vacancies and small vacancy clusters can be excluded since the associated  $S$ -parameters

are much too low (see table 7.3). In principle it is also possible, especially for larger voids, that positrons annihilate from surface states at the inner surfaces of the voids. For silicon surfaces terminated with hydrogen, the  $S$ -parameter for surface annihilations is the same as the  $S$ -parameter for (bulk) silicon (compare Gossmann *et al.*, 1992). However, in this case there will be positronium formation too, since branching occurs at such surfaces (see Schut, 1990). The number of positronium atoms formed depends on the condition of the inner surfaces, but it is improbable that surface-state annihilations completely preclude positronium formation. Approximately 50 % of the positrons arriving at a clean silicon surface form positronium (Schultz and Lynn, 1988). The effective  $S$ -parameter will be the average of the surface and positronium  $S$ -parameters [compare equation (2.17) on page 43]. Therefore, we conclude that the high  $S$ -parameter cannot be solely explained by surface-state annihilations.

The influence of atoms other than silicon on the  $S$ -parameter is as follows: Oxygen can be ruled out since it reduces the normalized  $S$ -parameter to a value lower than 1 (see table 7.3). In almost all cases, a gas filling of the voids also leads to a reduction of the  $S$ -parameter. The  $S$ -parameter related to the annihilations in voids decreases with increasing gas pressure, reaching the bulk value for pressures of the order of a few 100 kbar (compare the positron data for  $\alpha$ -Si:Kr [see section 7.4.1] and the measurements presented in chapter 5). This is in agreement with the measurements on MBE-system grown amorphous silicon. That type of amorphous silicon also has large voids, but the  $S$ -parameter is much higher than that of  $\alpha$ -Si:H grown at 50 °C. The sizes of the voids may be comparable but, probably due to the hydrogen filling of the voids and the Si-H bonds at the inner surface, the  $S$ -parameter is lower in the latter case. Therefore, it is improbable that foreign atoms cause the high  $S$ -parameter.

In conclusion, the only adequate explanation for the high  $S$ -parameter of the  $\alpha$ -Si:H samples seems to be to assume the formation of positronium in large voids that are present in the amorphous layer. However, since the  $S$ -parameter does not rise to the theoretical value of 1.16 for 100 % positronium formation, we conclude that there must also be considerable surface-state trapping with an  $S$ -parameter of, say, 1.035. The measured effective  $S$ -parameter of  $\sim 1.065$  for hydro-

generated amorphous silicon deposited at 50°C thus originates from a branching into positronium of

$$\frac{S_{\text{measured}} - S_{\text{surface}}}{S_{\text{Ps}} - S_{\text{surface}}} = \frac{1.065 - 1.035}{1.16 - 1.035} \approx 25 \%$$

and  $\sim 75 \%$  into surface-state traps. For reference, the extremely high  $S$ -value of MBE-system grown amorphous silicon (1.145) corresponds to a branching of  $\sim 90 \%$  into positronium. The fact that there is positronium formation in the a-Si:H films deposited at 50°C now sets a lower limit of  $\sim 25$  vacancies to the volume of voids in poor-quality amorphous silicon. This result may be compared with the work of Nasu *et al.* (1987) and He *et al.* (1986), who have estimated the mean void radius in the sample for which they observed positronium formation to be as high as  $\sim 2$  nm.

In our opinion, even the high  $S$ -parameters measured for large voids in metals (compare chapter 4) can also only be due to positronium formation. Evidence for the positron trapped in a metal void, existing at the void surface in a physisorbed positronium-like state under fast electron-spin conversion is summarized in Trumpy (1989). The positron in this positronium-like state is weakly localized near the metal surface (Van der Waals bond of a few tenths of an eV), but is in contact with the Fermi-sea electrons of the metal. Taken over a period of the order of 100 ps the positronium exists as a statistical average of  $o$ -Ps and  $p$ -Ps due to fast ortho-para conversion, while the average lifetime will be close to 500 ps (Platzman and Tzoar, 1986; Trumpy, 1989). The  $S$ -parameter related to voids in metals may be even higher than the one for voids in semiconductors, since, in comparison with silicon, there is a higher density of low-momentum electrons in the cavities due to the extension of the conduction-electron wave functions into the voids. Therefore even  $o$ -Ps annihilations may result in  $S$ -parameters higher than the value of 1.035 assumed above.

### Influence of growth conditions on the layer quality

From the SAXS data estimates for the void radius (actually the radius of gyration,  $R_g$ ) and the void fraction,  $v_f$ , can be derived (see

table 7.2). SAXS is able to detect microscopic structural inhomogeneities with an electron density  $\rho_i$  that differs from the electron density in the surrounding bulk. For the interpretation of SAXS spectra of hydrogenated amorphous silicon it is generally assumed that these inhomogeneities are voids and that  $\rho_i$  is close to zero. If this assumption is incorrect the void fraction  $v_f$  can be significantly underestimated. The possibility that the X-ray scattering of hydrogenated amorphous-silicon films is caused by microscopic regions with a low but nonzero electron density cannot be ruled out on the basis of SAXS spectra only. Infrared-absorption spectrometry does not provide decisive information either, since the vibrational mode observed in infrared spectra around  $2100\text{ cm}^{-1}$  may either be caused by SiH or SiH<sub>2</sub> bonds near silicon vacancies in the amorphous network or by larger cavities (Cardona, 1983; Wagner and Beyer, 1983; Chabal, 1991). However, the present positron-annihilation data rule out the former possibility, since positronium is only formed in large cavities with a negligible electron density.

When the deposition temperature increases from  $50^\circ\text{C}$  to  $200^\circ\text{C}$ , the  $S$ -parameter decreases to 1.0273 in case of deposition from a SiH<sub>4</sub>/H<sub>2</sub> mixture and to 1.0327 in case of deposition from undiluted SiH<sub>4</sub>. The simultaneous increase of the diffusion length (see table 7.2) shows that the total number of positron trapping sites decreases. Evidently, the number of voids or the size of the voids is reduced, or both. This is consistent with the observed strong dependence of the SAXS intensity on the deposition temperature (see figure 7.7). The SAXS data show that deposition at a higher temperature leads to a reduction of both the void fraction and the radius of gyration (see table 7.2). The scattering experiments also show that deposition from undiluted SiH<sub>4</sub> leads to *a*-Si:H films of poorer quality than films grown from SiH<sub>4</sub>/H<sub>2</sub>, which is also in accordance with the positron measurements that show slightly higher  $S$ -values in the former case. The decreasing void sizes lead to a decrease of the positronium formation probability and thus to a decrease of the  $S$ -parameter. For *a*-Si:H deposited at  $200^\circ\text{C}$  from a SiH<sub>4</sub>/H<sub>2</sub> gas mixture the  $S$ -parameter is even lower than 1.034, the  $S$ -value for divacancies in crystalline silicon (compare table 7.3). This effect is known to be caused by the presence of hydrogen close to the annihilation sites. Since such a low  $S$ -value is

only observed in good-quality films, it is probably indicative of the passivation of dangling bonds by hydrogen (compare chapter 6 and Leo *et al.*, 1981).

We conclude that the microscopic inhomogeneities in the a-Si:H samples deposited at low deposition temperatures ( $T_s = 50\text{--}100^\circ\text{C}$ ) are voids. For  $T_s = 150\text{--}200^\circ\text{C}$  the values of the  $S$ -parameter indicate that positron annihilation mainly occurs at vacancies containing hydrogen.

#### 7.4.4 A simple model for positronium in empty and gas-filled cavities

A simple model for positronium in a microcavity of radius  $r$  can be obtained under the assumption that the interaction of the positronium with its surroundings is described as a quantum mechanical particle in a three-dimensional rectangular potential well (compare Ferrell, 1957). Since positronium cannot exist in the bulk of metals and silicon (the binding energy equals zero), the potential well has a depth  $V_0$  which is larger than the positronium workfunction, i.e. for silicon:

$$V_0 \gg |\phi_{Ps}| \approx 2 \text{ eV} \quad (7.1)$$

(see Schultz and Lynn, 1988). Thus, as has been indicated in the insert of figure 7.8, positronium will dissociate and be absorbed as a separate bulk positron and valence electron when the energy of the positronium exceeds  $\phi_{Ps}$ . In our model we treat para-positronium and ortho-positronium similarly, since the energy difference between both states of positronium is very small ( $\Delta E = 8.3 \times 10^{-4} \text{ eV}$ ).

Solutions for wave functions and energy levels for a particle of mass  $m = 2m_e$  and radius zero in a square potential well of radius  $r$  are given in many textbooks on quantum mechanics, e.g., the textbook by Merzbacher (1970). An estimate of the interaction radius  $r'_{Ps}$  of positronium with the wall of the cavity is 0.1 nm, i.e. twice the radius of the positronium atom.

For the ground state ( $\ell = 0$ ) of the particle the energy  $E_n$  is found from:

$$\xi \cot \xi = -\eta, \quad (7.2)$$

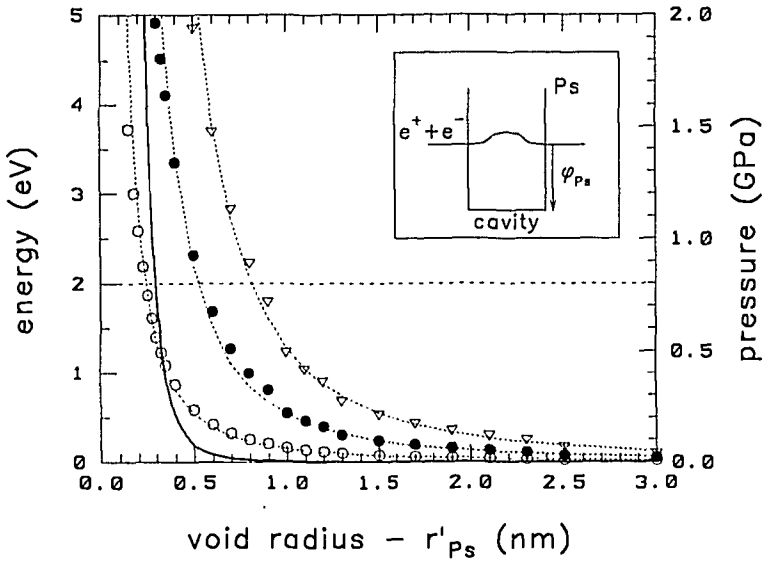


Figure 7.8: Energy levels of positronium with respect to the bottom of a three-dimensional rectangular potential well (see the insert) as a function of the cavity radius minus the radius of the positronium ( $r - r'_{Ps}$ ). The ground state level ( $n = 0$ :  $\circ$ ) and the levels of two excited states ( $n = 1$ :  $\bullet$ ;  $n = 2$ :  $\nabla$ ) are plotted. The pressure which the positronium atom exerts on its surroundings is plotted for the ground state only (solid line).

$$\xi^2 + \eta^2 = 2m V_0 r^2 / \hbar^2, \quad (7.3)$$

with  $\xi = r [2m(V_0 - E_n)]^{1/2} / \hbar$  and  $\eta = r (2m E_n)^{1/2} / \hbar$ . The energy levels with respect to the bottom of the potential well for the ground state ( $n = 0$ ) and the excited states ( $n = 1$  and  $n = 2$ ) are plotted versus the cavity radius minus the radius of the positronium atom ( $r - r'_{Ps}$ ) in figure 7.8. The energy levels have been calculated for  $V_0 = 5$  eV but the energies appear to be rather insensitive to changes to higher or lower potential well depths (Stewart *et al.*, 1990).

It appears from figure 7.8 that positronium in the ground state has no binding to cavities with a radius smaller than 0.35 nm (the binding energy becomes negative), which corresponds to voids consisting of at most nine vacancies in silicon. Excited positronium with  $n = 1$  has no binding to cavities with a radius  $< 0.65$  nm, while for the  $n = 2$  state the minimum radius amounts to 0.95 nm. Taking into

account thermally activated dissociation of positronium during its lifetime the radii of the cavities in which positronium can survive are even somewhat larger.

When placed in a gaseous surrounding which exerts a hydrostatic pressure  $P$  on the particle, positronium will counterbalance this pressure by adopting its volume  $V_{Ps}$  to a value given by:

$$P = -\frac{dE_n}{dV_{Ps}} = -4\pi r^2 \frac{dE_n}{dr}. \quad (7.4)$$

In equation (7.4) the effect of the surface tension has been neglected, since this value is small (see Stewart *et al.*, 1990). The curve for positronium in the ground state ( $n=0$ ) is shown in figure 7.8, from which can be derived that positronium will not exist in a gas bubble at pressures beyond 1 GPa. Taking into account thermally activated detrapping, stable energy levels will be 0.3 eV lower than  $\phi_{Ps}$  and thus the pressure will also be lower, i.e.  $\sim 0.7$  GPa.

This simple calculation explains rather well the results obtained for the gas decoration of the cavities in the implantation experiments of chapter 5. The cavities releasing helium at 800 °C have a radius clearly larger than 1 nm (Van Veen, 1991). When the cavities are devoid of helium or hydrogen gas, bound positronium may easily exist in the open volume. However, when the same amount of gas as used for the creation of the voids is re-implanted, the cavities will be pressurized again to a level equal to or higher than it has been during creation. The reason is that no annealing takes place during the re-implantation experiment and therefore all the helium is available for decoration of the cavities.

In silicon, bubbles hardly get to a state where the gas pressure is in equilibrium with the surface tension  $\gamma$  of the cavity, i.e. the equilibrium pressure  $P_{eq}$ :

$$P_{eq} = \frac{2\gamma}{r}. \quad (7.5)$$

At temperatures well below 1000 °C self-diffusion is still so slow that the cavity cannot expand quickly enough to arrive at the equilibrium size. Thus at moderate temperatures where helium does not permeate through the silicon, pressures higher than  $P_{eq}$  ( $\approx 1$  GPa for  $r = 2$  nm) may be attained by helium decoration. The same argument applies

for hydrogen at  $T < 600^\circ\text{C}$ . This may explain the reduction of the observed positronium fraction to nearly zero after decoration with the high doses hydrogen and helium in chapter 5. At low doses positronium appeared to be still present, indicating that the pressure had been in the range up to 0.7 GPa.

## 7.5 Conclusions

In this chapter we have described positron-annihilation measurements which improve our understanding of the defects in amorphous silicon, especially of the defects containing one or more vacancies.

The  $S$ -parameter for krypton-sputtered amorphous-silicon films, the first type of amorphous silicon examined, depends on the krypton concentration in the amorphous film. It decreases for higher concentrations of incorporated krypton. On the one hand the 50 eV krypton creates silicon self-interstitials, thereby reducing the number of vacancy-type defects, on the other hand the electrically inactive krypton atoms fill the positron traps. The material gets denser for higher krypton concentrations, in accordance with Raman results.

The second type of silicon was amorphous silicon grown in an MBE-system at a low deposition temperature. Positron measurements on this material yielded the very high  $S$ -parameter of 1.145, which is probably due to positronium formation in the large voids that are present in amorphous silicon.

The third species of silicon was hydrogenated amorphous silicon deposited in a PECVD process. The film quality improved at higher deposition temperatures, while deposition from undiluted  $\text{SiH}_4$  led to a deterioration of the  $a\text{-Si:H}$  with respect to deposition from a 1:1  $\text{SiH}_4/\text{H}_2$  mixture. The high  $S$ -parameter for the low-temperature deposited films was attributed to positronium formation in microcavities. However, the presence of hydrogen atoms in the voids apparently (partly) inhibited positronium formation leading to a decrease of the  $S$ -parameter (passivation of the traps). This explains why the  $S$ -parameter is not as high as that of MBE-system grown amorphous silicon.

NEXT PAGE(S) left BLANK.

# Chapter 8

## Epitaxial cobalt disilicide on silicon

### 8.1 Introduction

Metal-silicide films grown on silicon substrates are commonly used in the semiconductor industry as ohmic or Schottky-barrier contacts (Poate *et al.*, 1978). As device dimensions decrease, improvements in metal contacts are demanded. Epitaxial silicides offer a possible solution to this requirement because they surpass polycrystalline silicides in conductivity, thermal stability and reproducibility of interface properties (Murarka, 1980; Hsia *et al.*, 1992). Cobalt disilicide ( $\text{CoSi}_2$ ; Gurf *et al.*, 1978; Lau *et al.*, 1978) is a particularly attractive candidate because of its similar lattice structure ( $\text{CaF}_2$ ) and small lattice misfit to silicon ( $-1.2\%$  at room temperature). From a positron-oriented point of view silicon-silicide structures are also interesting for developing field-assisted positron moderators (Beling *et al.*, 1987).

Growth of epitaxial  $\text{CoSi}_2$  on Si(111) has been demonstrated by reacting pure cobalt with silicon using ultra-high vacuum (UHV) and molecular-beam epitaxy techniques (Tung *et al.*, 1982a and 1982b; Von Känel *et al.*, 1987 and 1990; Henz *et al.*, 1989; Chen and Chen, 1992). However, for implementation in modern integrated circuit (IC) production, it is required that the epitaxial silicide can be formed on Si(100). Van Ommen *et al.* (1988a) have shown that  $\text{CoSi}_2$  films

formed by the solid-state reaction of cobalt with Si(100) develop a strong (110) texture. Recently, epitaxial growth of a mixture of (100) and (110) oriented  $\text{CoSi}_2$  grains on Si(100) using the template method has been reported (Yalisove *et al.*, 1989). Another way of forming epitaxial cobalt-disilicide films in Si(100) is by very high dose implantation of cobalt into silicon (White *et al.*, 1987; Van Ommen *et al.*, 1988b and 1989; Maex *et al.*, 1990; Van den Berg *et al.*, 1990; Wu *et al.*, 1990). The implantations are generally carried out at elevated temperatures, in order to dynamically anneal the damage generated in the collision cascades of the impinging ions. An attractive process to grow epitaxial  $\text{CoSi}_2$  on Si(100) is to use sequentially evaporated TiCo bimetallic source material (Dass *et al.*, 1991; Hsia *et al.*, 1991 and 1992; Lawrence *et al.*, 1991). The reaction was performed at high temperature (10 s at 900 °C in  $\text{N}_2$ ) and these films show an excellent resistivity and thermal stability (Hsia *et al.*, 1992).

A new process for the production of (100) epitaxial cobalt disilicide on Si(100) substrates is employing the solid-state reaction between an amorphous binary metal alloy ( $\text{Co}_{60}\text{W}_{40}$ ) and Si (Reader *et al.*, 1991). These Co-W thin films were deposited, annealed and analysed in an UHV system. The same results can be achieved using the solid-state reaction between an amorphous  $\text{Co}_{75}\text{W}_{25}$  sputtered layer (deposited in a high-vacuum system) and Si(100) (La Via *et al.*, 1992). The latter authors have shown that the epitaxial silicide has a high residual resistivity ( $\rho = 22.7 \mu\Omega\text{cm}$ ) and a low carrier mobility after cobalt outdiffusion from the amorphous alloy. Furthermore, the  $\text{CoSi}_2$  minimum yield, defined as the ratio between the area of the cobalt peak in the channelled and random spectrum of Rutherford Backscattering Spectrometry (RBS), is about 70 % and a further anneal at 750 °C is needed to decrease the residual resistivity to  $2.6 \mu\Omega\text{cm}$  and the minimum yield to 20 %.

This chapter describes positron depth-profiling experiments on cobalt-disilicide films formed by the outdiffusion of cobalt from a sputtered  $\text{Co}_{75}\text{W}_{25}$  film, both after the first and the second anneal. With this process it is possible to obtain an epitaxial disilicide layer with the same characteristics as the best films obtained by ion implantation and MBE.

## 8.2 Sample preparation

Thin, 140 nm, layers of  $\text{Co}_{75}\text{W}_{25}$  have been magnetron sputtered from a compound target onto a freshly 1 % HF dipped low-ohmic Si(100) wafer (B-dope,  $0.01 \Omega\text{cm}$ ). The base pressure of the sputtering system, which does not contain a load-lock, was  $5 \times 10^{-7}$  Torr. No sputter etch was applied to the substrate. Pre-sputtering of the target was done for 15 min. During sputtering the argon pressure was  $5 \times 10^{-3}$  Torr and the deposition rate 0.84 nm/s. The atomic composition of the film, measured by 2 MeV  $\text{He}^+$  RBS, was  $\text{Co}_{75}\text{W}_{25}$ . The oxygen content of the as-deposited films was monitored with Auger Electron Spectroscopy (AES) and was found to be below the detection limit of this technique ( $\sim 0.1\%$ ). The thickness of the as-deposited layers was measured by a Taylor-Hobson Talystep. The resistivity of the as-deposited layer was about  $130 \mu\Omega\text{cm}$ .

The first-anneal was carried out in a vacuum furnace with a pressure better than  $8 \times 10^{-7}$  Torr at a temperature of  $550^\circ\text{C}$  for 8 hours in order to let the cobalt diffuse into the silicon. The annealed samples were then etched for 2 min. in a 1:1 mixture of  $\text{H}_2\text{O}_2$  (30 %)/ $\text{NH}_4\text{OH}$  (20 %) at room temperature to selectively remove the binary alloy. Any formed  $\text{CoSi}_2$  is not etched by this solution. The etch leaves a thin W-Si-O layer on the surface of the silicide which was removed by subsequent alternate etching in HF (2 %, 1 min.) and  $\text{H}_2\text{O}_2\text{:NH}_4\text{OH}$  (10 min.). The first cobalt-disilicide sample for positron annihilation was prepared in this way. It is labelled '*as-deposited*'.

Plan-view TEM shows that the majority of the  $\text{CoSi}_2$  film is epitaxial with the following orientation relationships (type A):

$$\begin{aligned} (001)_{\text{CoSi}_2} &\parallel (001)_{\text{Si}} \\ [100]_{\text{CoSi}_2} &\parallel [100]_{\text{Si}} \end{aligned}$$

However, in the  $\text{CoSi}_2$  about 32 % of the grains are twinned: these twinned grains are rotated by  $180^\circ$  around the  $\langle 111 \rangle$  axis (type-B material). The average dimension of the type-A grains is 73 nm, while the dimension of type-B grains is 47 nm. The grains twinned around the  $\langle 111 \rangle$  axis are randomly distributed in the film.

After the etch one sample was subjected to a second anneal at  $750^\circ\text{C}$  for 1 hour to improve the quality of the  $\text{CoSi}_2$  layer. After this

Table 8.1: Fit results for the positron-annihilation measurements of the three CoSi<sub>2</sub> samples. Only the  $S$ -parameters and diffusion lengths ( $L$ ) of the cobalt-disilicide layers are given.

sample	$S$	$L$
<i>as-deposited</i> CoSi <sub>2</sub>	1.0632 (8)	33 $\pm$ 3 nm
<i>annealed</i> CoSi <sub>2</sub>	1.0681 (15)	96 $\pm$ 10 nm
<i>crystalline</i> CoSi <sub>2</sub>	0.9036 (10)	126 $\pm$ 12 nm

anneal the total concentration of type-B grains reduced to  $\sim 16\%$  with an average dimension of the grains of 76 nm. Dark-field TEM revealed small dislocation loops, of which the total projected length has been estimated from the dechannelled fraction (in RBS) to be about  $1.7 \times 10^6$  cm/cm<sup>2</sup>. This second sample for positron annihilation is labelled '*annealed*'.

A reference sample, labelled '*crystalline*', consisted of 120 nm CoSi<sub>2</sub> prepared by cobalt implantation in Si(001), followed by an anneal at 1000 °C for 30 min. and a subsequent anneal at 800 °C for 8 hours in order to remove any quenched-in thermal vacancies. The substrate of the implanted silicide was  $n$ -type Si of 1000  $\Omega$ cm. Therefore a Schottky barrier (of 0.65 eV) will be present at the CoSi<sub>2</sub>/Si interface with a depletion layer of  $\sim 5$   $\mu$ m in the silicon.

### 8.3 Results

The results of the positron-annihilation measurements are shown in figure 8.1.

The positron data have been analysed with the program VEPFIT. The data points obtained from the *as-deposited* and *annealed* samples were fitted with a 3 layer model. The first layer ( $\rho = 9.86$  g/cm<sup>3</sup>) represents the WO<sub>2</sub> overlayer with a high concentration of silicon (*as-deposited* sample) or a pure WSi<sub>2</sub> layer (*annealed* sample). The second layer consists of CoSi<sub>2</sub> ( $\rho = 7.77$  g/cm<sup>3</sup>) while the silicon substrate forms the third layer ( $\rho = 2.33$  g/cm<sup>3</sup>). The fitted  $S$ -parameters and diffusion lengths for the CoSi<sub>2</sub> layer are given in table 8.1.

The measured data points from the *crystalline* CoSi<sub>2</sub> sample were

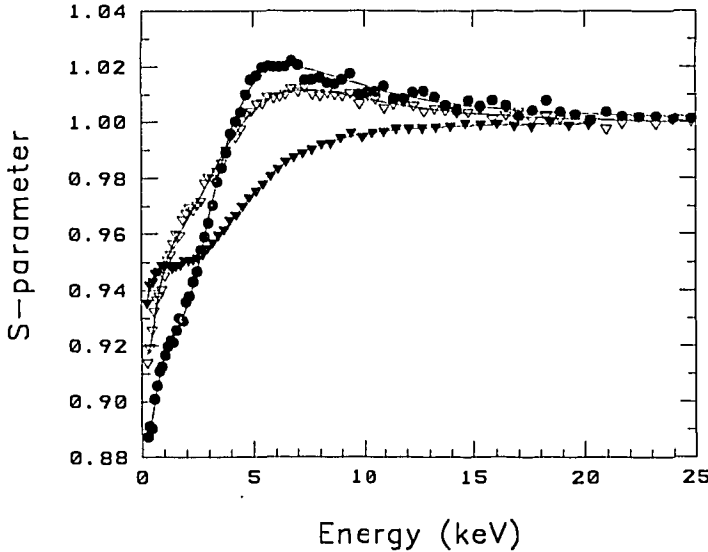


Figure 8.1: Positron-annihilation measurements on the three cobalt-disilicide samples, *as-deposited* CoSi<sub>2</sub> (●), *annealed* CoSi<sub>2</sub> (▽), and *crystalline* CoSi<sub>2</sub> (▼). The *S*-parameter is normalized to the *S*-value of c-Si.

analysed under the assumption of a 5 layer model: layers #1 and #2 represent the CoSi<sub>2</sub> ( $\rho = 7.77 \text{ g/cm}^3$ ; the top layer being of poorer quality than the second one); layer #3 is a 1 nm interface layer ( $\rho = 5 \text{ g/cm}^3$ ), while layers #4 and #5 describe the silicon substrate (layer #4 covers the first 5  $\mu\text{m}$  of the silicon).

CoSi<sub>2</sub> has a (negative!) positron workfunction  $\phi_+$  of -0.46 eV and an electron workfunction  $\phi_-$  of 4.62 eV (Gullikson *et al.*, 1988b). From these data the positron affinity  $\chi_+$  of CoSi<sub>2</sub> can be derived [compare equations (2.11) and (2.13)]:

$$\chi_+ = \mu_+ + \mu_- = -[\phi_+ + \phi_-] = -4.16 \text{ eV},$$

On the other hand, silicon has a positron affinity of  $\sim -4.8 \text{ eV}$  (Boev *et al.*, 1987; Schultz and Lynn, 1988). This means there is a potential step  $\Delta E_+$  of 0.64 eV at the interface [compare equation (2.14)] keeping the positrons, which are implanted in the silicon, from backdiffusing into the CoSi<sub>2</sub>. Additionally, the Schottky barrier provides another field in the silicon. The combined effects of the difference in positron affinity between cobalt disilicide and silicon and the Schottky barrier

were modelled by assuming a potential well of depth  $-0.65$  eV at the interface between layers #3 and #4, the interface therefore actually forming a positron 'sink'. This potential well yields electric fields in layers #3 and #4 of  $6.5 \times 10^6$  V/cm and  $-1.3 \times 10^3$  V/cm respectively. The fitted  $S$ -parameter and diffusion length for the *crystalline* CoSi<sub>2</sub> layer are also given in table 8.1.

In case of the *as-deposited* and *annealed* samples, fitting with a built-in electric field due to the difference in positron affinity did not lead to  $S$ -parameters and diffusion lengths considerably different from the values obtained from fitting without fields. Therefore, in those samples this effect has been neglected.

## 8.4 Discussion

The measured  $S$ -parameter for the *crystalline* CoSi<sub>2</sub> sample (0.9036) agrees remarkably well with the one found by Balogh *et al.* (1986) who found a value of 0.9035. On the other hand, it is much lower than the value reported by Frost *et al.* (1990) (they found 0.939), but this can be explained by the high concentration of positron trapping centres in their samples, which is evident from the absence of any positron diffusion.

The  $S$ -values obtained from both the *as-deposited* and the *annealed* CoSi<sub>2</sub> samples are more than 17 % higher than the  $S$ -value of the *crystalline* CoSi<sub>2</sub> sample. This relative shift in the  $S$ -parameter can be explained in just one way: The respective cobalt-disilicide films contain rather large vacancy-type defects, although the defect concentration is not very high (see below). Since all samples have been annealed at high temperatures, it is unlikely that the defects are point defects. Clusters of point defects are a more probable explanation.

Estimates for the defect concentration can be deduced from the values of the diffusion lengths on the assumption that there is only one type of defect present [see equation (4.7) on page 85]. For the diffusion length in defect-free CoSi<sub>2</sub> we take the value for *crystalline* CoSi<sub>2</sub> (126 nm). For the positron annihilation rate, the inverse of the positron lifetime [see equation (1.6) on page 26], we take the value of Garreau *et al.* (1991). They reported a lifetime of  $155 \pm 3$  ps,

which is lower than the value of Balogh *et al.* (1986), who found  $185 \pm 1$  ps, and is therefore more likely to be correct for defect-free  $\text{CoSi}_2$ . Assuming a typical specific trapping rate of  $2.6 \times 10^{14} \text{ s}^{-1}$  (Nieminen and Manninen, 1979), equation (4.7) now gives for the defect concentration in the *as-deposited* cobalt disilicide  $3.4 \times 10^{-4}$  (i.e.  $\sim 2.6 \times 10^{19} \text{ cm}^{-3}$ ), while the estimated defect concentration for the *annealed* cobalt disilicide amounts to  $1.5 \times 10^{-5}$  (i.e.  $\sim 1.1 \times 10^{18} \text{ cm}^{-3}$ ). These concentrations of open-volume defects will go unnoticed by defect-detection techniques like RBS.

The absence of a large change in the  $S$ -parameter after the second anneal indicates that the dominant type of defects seems to be the same in both outdiffused samples (*as-deposited* and *annealed*  $\text{CoSi}_2$ ), but the concentration of these defects is reduced upon annealing.

La Via *et al.* (1992) have derived the Debye temperature of  $\text{CoSi}_2$  in both its *as-deposited* (382 K) and *annealed* state (412 K) from electrical measurements. These values are lower than the value that Hensel *et al.* (1984) have found (450 K) for UHV deposited and reacted material on Si(111). The low Debye temperature observed in the *as-deposited* material is most likely due to the high density of vacancy clusters that leads to a less rigid lattice. After the second anneal, the number of vacancy-type defects decreases considerably, improving the rigidity of the cobalt-disilicide lattice and increasing the value of the Debye temperature. The value measured for *annealed*  $\text{CoSi}_2$  is not equal to the one measured by Hensel *et al.* (1984) probably because of the higher vacancy density present in our material.

The reduction of the concentration of vacancy-type defects after the second anneal is also the principal reason of the observed decrease in the residual resistivity and increase in the carrier mobility after the second anneal (La Via *et al.*, 1992). A further reduction of the lattice defects and of the cobalt-disilicide resistivity could not be obtained using high-temperature anneals because of the poorer thermal stability of the surface films when compared with the buried layers obtained by ion-implantation.

## 8.5 Conclusions

It has been shown that predominantly epitaxial cobalt-disilicide films on Si(100) can be prepared by cobalt outdiffusion from a sputtered  $\text{Co}_{75}\text{W}_{25}$  layer. However, positron-annihilation measurements indicate that a significant number of vacancy-type defects are present in the film ( $2.6 \times 10^{19} \text{ cm}^{-3}$ ). This rather high density of point-defect clusters is probably the reason for the high value of the residual resistivity of the  $\text{CoSi}_2$  layer after cobalt outdiffusion.

After a second anneal at a higher temperature ( $750^\circ\text{C}$ ) the structural and electrical properties of the cobalt disilicide improve considerably (La Via *et al.*, 1992). The number of vacancy-type defects decreases to  $1.1 \times 10^{18} \text{ cm}^{-3}$ . This reduction results in a decrease in the residual resistivity to  $2.6 \mu\Omega\text{cm}$  and an increase in the carrier mobility.

# Chapter 9

## Chemical-vapour deposited silicon-nitride films

### 9.1 Introduction

The characterization of defects in amorphous films of chemical-vapour deposited (CVD) silicon nitride ( $\text{Si}_3\text{N}_4$ ) has been the subject of several recently published papers (Fujita and Sasaki, 1985; Krick *et al.*, 1988; Jousse *et al.*, 1989; Kamigaki *et al.*, 1990). This interest stems from the application of silicon-nitride films in metal-nitride-oxide-silicon (MNOS) nonvolatile-memory structures and in hydrogenated amorphous-silicon based thin-film transistors. The various authors agree that the electrically active defects in the CVD nitrides are related to silicon dangling bonds. However, the specific nature of the active defects is still a matter of discussion (Jousse *et al.*, 1989; Kamigaki *et al.*, 1990).

In equilibrium, the bulk of as-deposited low-pressure CVD-nitride films appears to be charge free, whereas positive charge is observed at the interface with the silicon (Remmerie *et al.*, 1987; Heyns *et al.*, 1991). Annealing of the nitride/silicon layer structure in nitrogen ( $\text{N}_2$ ) at  $1000^\circ\text{C}$  causes negative charge to appear (Heyns *et al.*, 1991). Another observable effect of the anneal is the outdiffusion of hydrogen which was mainly present in  $=\text{N}-\text{H}$  groups before annealing up to concentrations of a few atomic percent (Arnold Bik *et al.*, 1990).

Subsequent annealing in hydrogen ( $H_2$ ) at  $1000^\circ C$  causes the negative charge to disappear. At the same time a part of the hydrogen is reintroduced through restoration of  $=N-H$  bonds (Oude Elferink *et al.*, 1987; Heyns *et al.*, 1991). Thus, a model has been developed in which nitrogen-related dangling-bond states are responsible for the negative charge (Habraken *et al.*, 1991). This model is based on the assumption that in the annealed nitrides the concentration of nitrogen dangling-bond states is larger than that of silicon dangling-bond states whereas the calculated position of the nitrogen states is low in the nitride energy gap (Robertson and Powell, 1984; Habraken *et al.*, 1991). Within this model two types of defects exist in silicon nitride, and the sign and magnitude of the equilibrium charge in the material depends on their relative concentrations. In most cases the low-lying states are all negatively charged and diamagnetic and are therefore invisible in Electron Spin Resonance (ESR) measurements.

## 9.2 Sample preparation

The sample structures consisted of 200 nm silicon-nitride ( $Si_3N_4$ ) films on silicon, deposited in a Low-Pressure Chemical-Vapour Deposition (LPCVD) process. The reactant gases were  $SiH_2Cl_2$  and  $NH_3$  with an input flow ratio  $NH_3/SiH_2Cl_2$  of 4. The deposition temperature was  $800^\circ C$ . In this process near-stoichiometric silicon-nitride films are grown (Habraken *et al.*, 1982) in which about 3 at.% of hydrogen is incorporated, mainly in  $=N-H$  bonding configurations (Habraken *et al.*, 1986). Both between the nitride and the silicon substrate and on top of the nitride layer, oxide layers of a few Å are present (Habraken *et al.*, 1982). Therefore, the sample in fact consisted of four distinct layers, including the substrate.

To study the effect of the outdiffusion of hydrogen a number of silicon-nitride samples were annealed in flowing argon at  $1000^\circ C$  for times ranging from 10 minutes to 1 hour. Furthermore, the sample annealed for 1 hour was annealed again in an  $N_2/D_2$  atmosphere [ $D_2/(N_2+D_2) = 4\%$ ; 5 min. at  $900^\circ C$ ] in order to reintroduce some of the hydrogen (actually the hydrogen-isotope deuterium) (Habraken *et al.*, 1986; Marée *et al.*, 1991; Arnold Bik *et al.*, 1993).

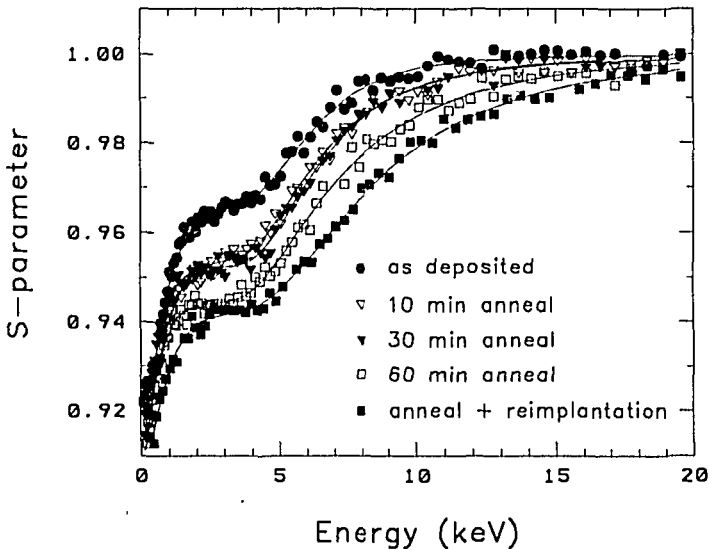


Figure 9.1: Measured  $S$ -parameter versus incident positron energy (keV) of the five silicon-nitride samples. The lines represent the VEPFIT fits of the data. The  $S$ -parameters are scaled to their fitted silicon values (1.000).

Positron-annihilation  $S$ -parameter measurements have been performed on these five samples.

## 9.3 Results

Figure 9.1 shows the results of the Doppler  $S$ -parameter measurements. The data have been analysed with the program VEPFIT assuming that four layers in the sample contribute to the  $S$ -parameter, viz. the silicon-nitride layer, the silicon substrate, and two additional layers consisting of  $\text{SiO}_2$ , one at the interface between the silicon and the silicon nitride, the other at the outer surface of the sample. There was a considerable time interval between the measurements of the first four samples and the last ( $\text{D}_2$ -annealed) one. Owing to several changes of the configuration of the beamline, the absolute values of the  $S$ -parameter had shifted by about 0.025 by the time the last sample was investigated. In order to be able to compare the results, all  $S$ -values have been scaled to the fitted silicon value according

Table 9.1: Results of the fits for the silicon-nitride layers of the five samples examined.

post-growth sample treatment	$S$ (scaled)	diffusion length
<i>as-deposited</i>	0.9673	10.8 nm
10 min. anneal at 1000 °C	0.9550	10.4 nm
30 min. anneal at 1000 °C	0.9527	5.3 nm
60 min. anneal at 1000 °C	0.9449	5.7 nm
60 min. anneal at 1000 °C and reintroduction of D <sub>2</sub>	0.9428	9.4 nm

to equation (2.16). The error in this scaled  $S$ -parameter amounts to approximately 0.005, except for the sample with the 30 minutes anneal, where it is about 0.010 as a result of the lack of data for higher positron incident energies and, consequently, the bad fit of the silicon  $S$ -value. The errors in the values of the diffusion length may be as large as 10 % of the fitted value. The results of the fits for the silicon-nitride layer are given in table 9.1.

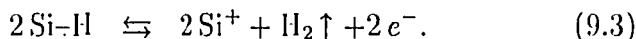
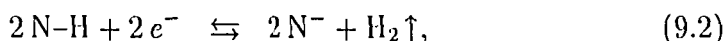
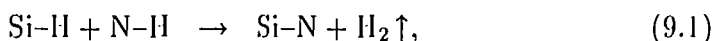
Prolonged heating causes the  $S$ -parameter of the silicon-nitride layer to decrease from 0.967 (the *as-deposited* sample) to about 0.945 after a 60 minutes anneal at 1000 °C. The diffusion length is also influenced by the anneal, since it shows a decrease from about 10 nm to 5 nm. The reintroduction of D<sub>2</sub> reestablishes this parameter to a value close to the original 10 nm, but the  $S$ -parameter remains low. Apparently, the defect structure of the *as-deposited* sample was not retrieved by the reintroduction of hydrogen. Within the experimental resolution the  $S$ -parameter appears to be constant over the depth of the film.

## 9.4 Discussion

The decreasing values of the  $S$ -parameters from table 9.1 indicate a decreasing defect density for longer annealing times. On the other hand, the decreasing diffusion-length data show a higher trapping rate for longer annealing times and therefore indicate that the defect

concentration rises (assuming constant specific trapping rates).

This inconsistency can be resolved by assuming an  $S$ -parameter for the defects present in the layer which is lower than that for defect-free silicon nitride itself. Suppose the *as-deposited*  $\text{Si}_3\text{N}_4$  sample contains a certain concentration of defects, both  $\text{N}^-$  and  $\text{Si}^+$  defects in equal quantity, consistent with the model for the electrical properties of Habraken *et al.* (1991). Through the anneal in nitrogen at  $1000^\circ\text{C}$  both the  $\text{N-H}$  and the  $\text{Si-H}$  bonds (of the hydrogen incorporated in the silicon-nitride lattice) are broken, according to the processes:



The total number of defects increases, which corresponds to the decreasing diffusion length. However, far more  $\text{N-H}$  bonds than  $\text{Si-H}$  bonds are broken (Habraken *et al.*, 1986 and 1991). Therefore, the concentration of  $\text{N}^-$  defects increases (much) faster than the one of  $\text{Si}^+$  defects, leading to an overall negative charge. Relatively more positrons will annihilate with electrons of the  $\text{N}^-$  defects than with electrons of the  $\text{Si}^+$  defects, first because the concentration is higher, and secondly because the positron trapping rate for positively charged silicon defects is very small (Puska *et al.*, 1990). Due to the negative charge of the  $\text{N}^-$  defects the overlap of the positron wave function with the  $\text{N}^-$  core electrons is greater than that with silicon atoms, resulting in a relatively larger annihilation rate with core electrons. This might result in an  $S$ -parameter lower than the one of defect-free silicon nitride. This interpretation is consistent with the lower  $S$ -parameters of electronegative ions as, e.g., oxygen in  $\text{SiO}_2$  (Coleman *et al.*, 1990),  $\text{Ga}_2\text{O}_3$ , or  $\text{As}_2\text{O}_3$  (Lee *et al.*, 1991).

After the  $900^\circ\text{C}$  anneal in the  $\text{D}_2/\text{N}_2$  mixture the number of defects decreases again through defect passivation of the  $\text{N}^-$  and  $\text{Si}^+$  trapping centres [the reverse of equations (9.2) and (9.3)]. Nevertheless, many more  $\text{N}^-$  than  $\text{Si}^+$  defects remain. This accounts for the increase of the positron diffusion length to a value above 9 nm, while the  $S$ -value remains rather constant (see table 9.1). This treatment does not reintroduce all hydrogen into the sample (Habraken *et al.*,

1986; Marée *et al.*, 1991). Detailed VEPFIT analysis shows a small gradient in the diffusion length in the 200 nm silicon-nitride layer. Positrons stopped in the upper 100 nm have a diffusion length of approximately 10.0 nm, those stopped in the lower 100 nm one of 8.7 nm. Hence, in the toplayer more hydrogen has been reintroduced than in the deeper regions of the sample.

## 9.5 Conclusions

In conclusion, this study has shown that positron-beam measurements of low-pressure CVD silicon-nitride layers are able to detect the formation and passivation of some defects, which may principally be associated with  $N^-$  ions. Annealing of the samples at 1000 °C for times up to 1 hour resulted in a decrease of both the  $S$ -parameter and the positron diffusion length of the silicon nitride, which has been attributed to the faster increase of the concentration of nitrogen-related defects than of silicon-related defects. After re-introduction of deuterium the diffusion length recovers but the  $S$ -parameter remains low, which can be explained by the passivation of some of the  $N^-$  and  $Si^+$  trapping centres while the concentration of  $N^-$  defects remains higher than the concentration of  $Si^+$  defects. This interpretation is consistent with a model that is applied to understand some electrical properties of the LPCVD silicon nitride.

# Summary

In this thesis some contributions of the positron-depth profiling technique to materials science have been described. A review of this technique was presented in chapters 1 and 2, while chapter 3 dealt with the Delft Variable Energy Positron Beam and some techniques employed for acquiring additional information on the materials examined. *Following studies are carried out:*

Positron-annihilation measurements on neon-implanted steel have been reported in chapter 4. Damage up to depths of 10 times the mean implantation range was observed and has been attributed to the channelling of neon atoms to greater depth during implantation, leading to the formation of small  $\text{NeV}_m$  complexes, of which the excess vacancies dissociate at  $250^\circ\text{C}$ . Neon bubble growth, starting at  $600^\circ\text{C}$ , was evident from the drastic increase of the  $S$ -parameter at this temperature.

Chapter-5-reported Void creation in silicon by helium implantation. Voids created during a low-dose implantation could be removed by a high-temperature anneal, but a high-dose implantation led to voids that were still stable at  $800^\circ\text{C}$ . The high  $S$ -parameter observed for annihilations in voids has been ascribed to positronium formation and annihilation in the micro-cavities. Filling the voids with helium or hydrogen reduced the positronium formation probability and indeed led to lower  $S$ -parameters.

By positron measurements the density of vacancy-type defects present in amorphous silicon prepared by ion implantation has been estimated at 1.2 at.%, as described in chapter 6. Relaxation at  $500^\circ\text{C}$  lowers this value to 0.4 at.%. From a comparison of positron data with the results of free-carrier lifetime measurements, it has been

concluded that the band-gap states acting as recombination centers for free carriers are associated with vacancy-type defects.

(5) Chapter-7-reported-on measurements of other types of amorphous silicon. Silicon grown by krypton sputter-deposition appeared to have only a limited number of vacancy-type defects. During deposition krypton atoms and silicon self-interstitials filled the traps. On the other hand, large cavities were detected in amorphous silicon grown in an MBE-system. The quality of hydrogenated silicon deposited in a PECVD process appeared to depend heavily on growth conditions like the deposition temperature. The presence of hydrogen in the voids (partly) inhibited positronium formation, so that annihilations in the large cavities did not yield high  $S$ -values. A simple model is given for the relation between positronium formation in voids and gas-filled micro-cavities.

(6) Epitaxial cobalt disilicide prepared by cobalt outdiffusion has been studied in chapter 8. A high concentration of vacancy-type defects was present in the film, which decreased however after an anneal at 750 °C, thereby improving the electrical properties.

(7) Finally, chapter-9-reported-on positron-annihilation experiments on low-pressure CVD silicon-nitride films. The formation and passivation of some defects, which were principally associated with negatively charged nitrogen ions, have been followed after various anneals and after re-introduction of deuterium.

In conclusion, the positron depth-profiling technique is able to give valuable information on specific problems in materials science. Although the data has to be subjected to a careful analysis, the outcome may prove to give unique insight in some of the physical processes that play a role on a microscopic scale in our macroscopic world.

(a-g. Van)

# Samenvatting

In dit proefschrift werd verslag gedaan van enkele bijdragen van de positron diepte-profileringstechniek aan de materiaalkunde. In de hoofdstukken 1 en 2 is een overzicht van de meetmethode gegeven, terwijl in hoofdstuk 3 de Delftse Variabele Energie Positron-bundel werd beschreven, evenals een aantal technieken die aanvullende informatie konden geven over de onderzochte materialen.

Positron-annihilatie metingen aan neon-geïmplantiseerd staal zijn in hoofdstuk 4 weergegeven. In het materiaal werd schade geconstateerd tot op een diepte van 10 maal de gemiddelde implantatiediepte van het neon. Dit werd verklaard door het naar grote diepte channelen van neon-atomen tijdens de implantatie. Dit leidde vervolgens tot de vorming van kleine  $\text{NeV}_m$ -complexen, waarvan de overvloedige vacatures bij  $250^\circ\text{C}$  dissociëren. Neon-bellen beginnen bij  $600^\circ\text{C}$  te groeien, wat uit de grote toename van de  $S$ -parameter bij deze temperatuur blijkt.

Hoofdstuk 5 beschreef het creëren van holten in silicium door middel van het implanteren van helium. De holten die door een lage-dosis implantatie waren gemaakt, konden weer worden verwijderd door een verhitting op hoge temperatuur. Een hoge dosis helium leidde daarentegen tot de vorming van holten die tenminste tot  $800^\circ\text{C}$  stabiel bleven. De hoge  $S$ -parameter die voor annihilatie in holten wordt waargenomen, werd toegeschreven aan de vorming en annihilatie van positronium in deze holten. De vormingswaarschijnlijkheid van positronium kon worden verlaagd door de lege ruimte met helium of waterstof te vullen, wat inderdaad uit de verlaging van de gemeten  $S$ -parameter bleek.

Positron-metingen leverden een schatting van 1.2 atoomprocent op

voor de dichtheid van vacature-achtige defecten in amorf silicium dat door middel van ionen-implantatie vervaardigd was. Dit onderzoek is beschreven in hoofdstuk 6. Na het materiaal bij 500 °C te laten relaxeren daalde deze waarde tot 0.4 atoomprocent. Uit een vergelijking van de uitkomsten van de positron-annihilatie metingen met de resultaten van levensduurmetingen van de vrije ladingsdragers, werd geconcludeerd dat de toestanden in de band-gap, die als recombinatiecentra dienen, geassocieerd zijn met vacature-achtige defecten.

Hoofdstuk 7 bevatte de resultaten van positron-metingen aan enkele andere soorten amorf silicium. Silicium dat via krypton sputterdepositie was gegroeid, bleek slechts een gering aantal vacature-achtige defecten te bevatten. Tijdens de depositie werden de mogelijke positron-traps gevuld door krypton-atomen en silicium zelf-interstitiëlen. In amorf silicium dat in een MBE-opstelling vervaardigd was, werden daarentegen grote holten ontdekt. De kwaliteit van gehydrogeneerd amorf silicium, afkomstig uit een PECVD proces, bleek sterk af te hangen van de groeicondities zoals de substraattemperatuur. De aanwezigheid van waterstof in de holten verlaagde de vormingswaarschijnlijkheid van positronium, zodat annihilaties in de holten niet tot erg hoge *S*-waarden leidde.

Epitaxiaal cobalt-disilicide, dat door de uitdiffusie van cobalt in silicium gemaakt was, werd in hoofdstuk 8 onderzocht. In de laag was een hoge concentratie aan vacature-achtige defecten aanwezig, die echter afnam na verhitting tot 750 °C, waardoor ook de elektrische eigenschappen verbeterden.

Tenslotte beschreef hoofdstuk 9 positron-annihilatie metingen aan LPCVD silicium-nitride lagen. De vorming en passivering van enkele defecten, die voornamelijk met de negatief geladen stikstof-ionen geassocieerd zijn, werden gevolgd tijdens de verschillende verhittingen en na herintroductie van deuterium.

Samenvattend kan gesteld worden dat de positron-annihilatie diepte-profilerings techniek waardevolle informatie kan geven over specifieke problemen in de materiaalkunde. Hoewel de meetgegevens nauwkeurig geanalyseerd moeten worden, kunnen de uitkomsten een uniek inzicht verschaffen in enkele fysische processen die op een microscopische schaal een rol spelen in onze macroscopische wereld.

# Bibliography

- Alatalo, M., M.J. Puska, and R.M. Nieminen, *Phys. Rev. B*, **46**, 1992, 12806.
- Alvager, T., and N.J. Hansen, *Rev. Sci. Instr.*, **33**, 1962, 567.
- Amarendra, G., B. Viswanathan, and K.P. Gopinathan, *Rad. Effects*, **118**, 1991, 357.
- Anderson, C.D., *Phys. Rev.*, **41**, 1932, 405.
- Anderson, C.D., *Phys. Rev.*, **43**, 1933a, 491.
- Anderson, C.D., *Phys. Rev.*, **44**, 1933b, 406.
- Aourag, H., B. Khelifa, A. Belaidi, and Z. Belarbi, *Phys. Status Solidi B*, **160**, 1990, 201.
- Aourag, H., and B. Khelifa, *Mater. Chem. and Phys.*, **27**, 1991, 61.
- Arnold Bik, W.M., R.N.H. Linssen, F.H.P.M. Habraken, W.F. van der Weg, and A.E.T. Kuiper, *Appl. Phys. Lett.*, **56**, 1990, 2530.
- Arnold Bik, W.M., C.H.M. Marée, A.J.H. Maas, M.J. van den Boogaard, F.H.P.M. Habraken, and A.E.T. Kuiper, *Phys. Rev. B*, **48**, 1993, 5444.
- Aruga, T., S. Takamura, M. Hirose, and Y. Itoh, *Phys. Rev. B*, **46**, 1992, 14411.
- Ashley, J.C., *J. Electron Spectrosc. Relat. Phenom.*, **50**, 1990, 323.
- Asoka-Kumar, P., and K.G. Lynn, *Appl. Phys. Lett.*, **57**, 1990, 1634.
- Asoka-Kumar, P., H.J. Gossmann, F.C. Unterwald, L.C. Feldman, T.C. Leung, H.L. Au, V. Talyanski, Bent Nielsen, and K.G. Lynn, *Phys. Rev. B*, **48**, 1993, 5345.
- Baker, J.A., N.B. Chilton, K.O. Jensen, A.B. Walker, and P.G. Coleman, *J. Phys.: Condens. Matter*, **3**, 1991, 4109.
- Balogh, A.G., L. Bottyán, G. Brauer, I. Dézsi, and B. Molnár, *J. Phys. F: Met. Phys.*, **16**, 1986, 1725.
- Barbiellini, B., P. Genoud, and T. Jarlborg, *J. Phys.: Condens. Matter*, **3**, 1991, 7631.
- Bean, J.C., and J.M. Poate, *Appl. Phys. Lett.*, **36**, 1980, 59.
- Beasley, P., R.N. West, and A. Alam, *Mater. Sci. Forum*, **15-18**, 1987, 175.
- Beeman, D., T. Tsu, and M.F. Thorpe, *Phys. Rev. B*, **32**, 1985, 874.
- Beling, C.D., R.I. Simpson, M. Charlton, F.M. Jacobson, T.C. Griffith, P. Moriarty, and S. Fung, *Appl. Phys. A*, **42**, 1987, 111.
- Belotti, E., M. Corti, E. Fiorini, C. Liguori, A. Pullia, A. Sarracino, P. Sverzellati, and L. Zanotti, *Phys. Lett. B*, **124**, 1983, 435.

- Berg, J.M. van den, A.E. White, R. Hull, K.T. Short, and S.M. Yalisove, *J. Appl. Phys.*, **67**, 1990, 787.
- Bergman, K., M. Stavola, S.J. Pearton, and J. Lopata, *Phys. Rev. B*, **37**, 1988, 2770.
- Beurs, H. de, *Wear Behaviour of Laser-Melted and Ion-Implanted Materials, thesis*, Groningen University, Groningen, 1988.
- Beurs, H. de, and J.Th.M. de Hosson, *Appl. Phys. Lett.*, **53**, 1988, 663.
- Beyer, W., *Physica B*, **170**, 1991, 105.
- Bhide, V.G., R.O. Dusane, S.V. Rajarshi, A.D. Shaligram, and S.K. David, *J. Appl. Phys.*, **62**, 1987, 108.
- Boev, O.V., M.J. Puska, and R.M. Nieminen, *Phys. Rev. B*, **36**, 1987, 7786.
- Bolse, W., Proc. Workshop on Applications of High Resolution Gamma Spectroscopy in Studies of Atomic Collisions and Nuclear Lifetimes, October 5-7, 1992, Grenoble.
- Boogaard, M.J. van den, *Microvoids and Hydrogen Diffusion in Hydrogenated Amorphous Silicon, thesis*, Utrecht University, Utrecht, 1992.
- Boogaard, M.J. van den, S.J. Jones, Y. Chen, D.L. Williamson, R.A. Hakvoort, A. van Veen, A.C. van der Steege, W.M. Arnold Bik, W.G.J.H.M. van Sark, and W.F. van der Weg, *Mater. Res. Soc. Symp. Proc.*, **258**, 1992, 407.
- Boronski, E., *Mater. Sci. Forum*, **105-110**, 1992, 181.
- Boyce, J.B., N.M. Johnson, S.E. Ready, J. Walker, and G.B. Anderson, *Mater. Res. Soc. Symp. Proc.*, **262**, 1992, 401.
- Brandes, G.R., A.P. Mills jr., S.S. Voris jr., and D.M. Zuckerman, *Mater. Sci. Forum*, **105-110**, 1992a, 1359.
- Brandes, G.R., A.P. Mills jr., and D.M. Zuckerman, *Mater. Sci. Forum*, **105-110**, 1992b, 1363.
- Brandt, W., and A. Dupasquier, *Positron Solid-State Physics*, Proc. of the Int. School of Phys. "Enrico Fermi", North-Holland, Amsterdam, 1983.
- Britton, D.T., P.C. Rice-Evans, and J.H. Evans, *Phil. Mag. Lett.*, **57**, 1988, 165.
- Britton, D.T., P.A. Huttunen, J. Mäkinen, E. Soininen, and A. Vehanen, *Phys. Rev. Lett.*, **62**, 1989, 2413.
- Britton, D.T., P. Willutzki, T.E. Jackman, and P. Mascher, *J. Phys.: Condens. Matter*, **4**, 1992, 8511.
- Brodsky, M.H., R.S. Title, K. Weiser, and G.D. Petit, *Phys. Rev. B*, **1**, 1970, 2632.
- Brower, K., *Appl. Phys. Lett.*, **53**, 1988, 508.
- Brusa, R.S., A. Dupasquier, R. Grisenti, S. Liu, S. Oss, and A. Zecca, *J. Phys.: Condens. Matter*, **1**, 1989, 5411.
- Brusa, R.S., M. Duarte Naia, A. Dupasquier, G. Ottaviani, R. Tonini, and A. Zecca, *Mater. Sci. Forum*, **105-110**, 1992, 1367.
- Buda, F., G.L. Chiarotti, R. Car, and M. Parrinello, *Phys. Rev. Lett.*, **63**, 1989, 294.
- Byakov, V.M., V.I. Goldanskii, and V.P. Shantarovich, *Dokl. Akad. Nauk SSSR*, **219**, 1974, 633.

- Cachard, A., and J.P. Thomas, in: *Material Characterization Using Ion Beams*, NATO Advanced Study Inst. Series, **B28**, eds. J.P. Thomas and A. Cachard, Plenum Press, New York, 1978.
- Car, R., and M. Parrinello, *Phys. Rev. Lett.*, **60**, 1988, 204.
- Carbotte, J.P., and H.L. Arora, *Can. J. of Phys.*, **45**, 1967, 387.
- Cardona, M., *Phys. Status Solidi B*, **118**, 1983, 463.
- Cerofolini, G.F., L. Meda, C. Volpones, G. Ottaviani, J. Defayette, R. Dierckx, D. Donelli, M. Orlandini, M. Anderle, R. Canteri, C. Clayes, and J. Vanhellemont, *Phys. Rev. B*, **41**, 1990, 12607.
- Chabal, Y.J., *Physica B*, **170**, 1991, 447.
- Chapman, B.N., *Glow Discharge Processes: Sputtering and Plasma Etching*, John Wiley, New York, 1980.
- Chen, D.M., K.G. Lynn, R. Pareja, and Bent Nielsen, *Phys. Rev. B*, **31**, 1985, 4123.
- Chen, B.S., and M.C. Chen, *J. Appl. Phys.*, **72**, 1992, 4619.
- Cheng, K.L., Y.C. Jean, and X.H. Luo, *Crit. Rev. in Analyt. Chem.*, **21**, 1989, 209.
- Chilton, N.B., J.A. Baker, and P.G. Coleman, in: *Positron Beams for Solids and Surfaces*, *AIP Conf. Proc.*, **218**, eds. P.J. Schultz, G.R. Massoumi, and P.J. Simpson, AIP, New York, 1990.
- Coffa, S., and J.M. Poate, *Appl. Phys. Lett.*, **59**, 1991, 2296.
- Coffa, S., J.M. Poate, D.C. Jacobson, and A. Polman, *Appl. Phys. Lett.*, **58**, 1991, 2916.
- Coleman, P.G., N.B. Chilton, and J.A. Baker, *J. Phys.: Condens. Matter*, **2**, 1990, 9355.
- Coleman, P.G., L. Albrecht, K.O. Jensen, and A.B. Walker, *J. Phys.: Condens. Matter*, **4**, 1992a, 10311.
- Coleman, P.G., J.A. Baker, and N.B. Chilton, *Mater. Sci. Forum*, **105-110**, 1992b, 213.
- Corbett, J.W., J.K. Karius, and T.Y. Tan, *Nucl. Instr. and Meth.*, **182-183**, 1981, 457.
- Corbett, J.W., S.N. Sahu, T.S. Shi, and L.C. Snyder, *Phys. Lett.*, **93A**, 1983, 303.
- Custer, J.S., M.O. Thompson, D.C. Jacobson, J.M. Poate, S. Roorda, W.C. Sinke, and F. Spaepen, *Mater. Res. Soc. Symp. Proc.*, **157**, 1990, 689.
- Dannefaer, S., G.W. Dean, D.P. Kerr, and B.G. Hogg, *Phys. Rev. B*, **14**, 1976, 2709.
- Dannefaer, S., D. Kerr, and B.G. Hogg, *J. Appl. Phys.*, **54**, 1983, 155.
- Dannefaer, S., and D. Kerr, *J. Appl. Phys.*, **60**, 1986, 1313.
- Dannefaer, S., P. Mascher, and D. Kerr, *Phys. Rev. Lett.*, **56**, 1986, 2195.
- Dannefaer, S., *Phys. Status Solidi A*, **102**, 1987, 481.
- Dass, M.L.A., D.B. Fraser, and C.S. Wei, *Appl. Phys. Lett.*, **58**, 1991, 1308.
- Dearnaley, G., and N.E.W. Hartley, *Thin Solid Films*, **54**, 1978, 215.
- Dearnaley, G., *Nucl. Instr. and Meth. B*, **50**, 1990, 358.

- DeBenetti, S., C.E. Cowan, and W.R. Konneker, *Phys. Rev.*, **76**, 1949, 440.
- DeLeo, G.G., W.B. Fowler, and G.D. Watkins, *Phys. Rev. B*, **29**, 1984, 1819.
- Deutsch, M., *Phys. Rev.*, **82**, 1951a, 455.
- Deutsch, M., *Phys. Rev.*, **83**, 1951b, 866.
- Deutsch, M., and E. Dulet, *Phys. Rev.*, **84**, 1951, 601.
- Dirac, P.A.M., *Proc. Cambridge Philos. Soc.*, **26**, 1930, 361.
- Dlubek, G., O. Brümmer, N. Meyendorf, P. Hautojärvi, A. Vehanen, and J. Yli-Kauppila, *J. Phys. F: Met. Phys.*, **9**, 1979, 1961.
- Dlubek, G., and R. Krause, *Phys. Status Solidi A*, **102**, 1987, 443.
- Doany, F.E., D. Grischkowsky, and D.C. Chi, *Appl. Phys. Lett.*, **50**, 1987, 460.
- Downer, M.C., and C.V. Shank, *Phys. Rev. Lett.*, **56**, 1986, 761.
- Dupasquier, A., in: *Positron Solid-State Physics*, Proc. of the Int. School of Phys. "Enrico Fermi", eds. W. Brandt and A. Dupasquier, North-Holland, Amsterdam, 1983.
- Eaglesham, D.J., H.J. Gossman, and M. Cerullo, *Phys. Rev. Lett.*, **65**, 1990, 1227.
- Eldrup, M., in: *Positron Annihilation*, Proc. ICPA-6, eds. P.C. Coleman, S.C. Sharma, and L.M. Diana, North-Holland, Amsterdam, 1982.
- Eldrup, M., in: *Positron Solid-State Physics*, Proc. of the Int. School of Phys. "Enrico Fermi", eds. W. Brandt and A. Dupasquier, North-Holland, Amsterdam, 1983.
- Eldrup, M., *Mater. Sci. Forum*, **105-110**, 1992, 229.
- Elliman, R.G., J. Linnros, and W.L. Brown, *Mater. Res. Soc. Symp. Proc.*, **100**, 1988, 363.
- Esser, A., K. Seibert, H. Kurz, G.N. Parsons, C. Wang, B.N. Davidson, G. Lucovsky, and R.J. Nemanich, *Phys. Rev. B*, **41**, 1990, 2879.
- Estreicher, S.K., L. Throckmorton, and D.S. Marynick, *Phys. Rev. B*, **39**, 1989, 13241.
- Evans, J.H., A. van Veen, and C.C. Griffioen, *Nucl. Instr. and Meth. B*, **28**, 1987, 360.
- Feldman, L.C., and J.W. Mayer, *Fundamentals of Surface and Thin Film Analysis*, North-Holland, Amsterdam, 1986.
- Ferrell, R.A., *Phys. Rev.*, **108**, 1957, 167.
- Fink, D., L. Wang, and J. Martan, in: *Fundamental Aspects of Inert Gases in Solids*, NATO ASI Series B, **279**, eds. S.E. Donnelly, and J.H. Evans, Plenum Press, New York, 1991.
- Fork, R.L., B.I. Greene, and C.V. Shank, *Appl. Phys. Lett.*, **38**, 1981, 671.
- Frost, R.L., A.B. DeWald, M. Zaluzec, J.M. Rigsbee, Bent Nielsen, and K.G. Lynn, *J. Vac. Sci. Technol. A*, **8**, 1990, 3210.
- Fujita, S., and A. Sasaki, *J. Electrochem. Soc.*, **132**, 1985, 398.
- Garreau, Y., P. Lerch, T. Jarlborg, E. Walker, P. Genoud, A.A. Manuel, and M. Peter, *Phys. Rev. B*, **43**, 1991, 14532.
- Gemmel, D., *Rev. Mod. Phys.*, **46**, 1974, 1.

- Gerold, V., in: *Small Angle X-Ray Scattering*, ed. H. Brumberger, Gordon and Breach, New York, 1967.
- Gerritsen, E., H.A.A. Keetels, and H.J. Ligthart, *Nucl. Instr. and Meth. B*, **39**, 1989, 614.
- Gerritsen, E., *Surface Modification of Metals by Ion Implantation*, thesis, Groningen University, Groningen, 1990.
- Gerritsen, H.C., and C. Robertus, in: *Applications of Synchrotron Radiation*, eds. C.R.A. Catlow, and G.N. Greaves, Blackie, Glasgow, 1990.
- Ghosh, V.J., D.O. Welch, and K.G. Lynn, to be published in: *Proc. SLOPOS5*, August 6–10, 1992, Jackson WY.
- Gnaser, H., H.L. Bay, and W.O. Hofer, *Nucl. Instr. and Meth. B*, **15**, 1986, 49.
- Goldanskii, V.I., *At. Energy Rev.*, **6**, 1986, 3.
- Gossmann, H.J., P. Asoka-Kumar, T.C. Leung, Bent Nielsen, K.G. Lynn, F.C. Unterwald, and L.C. Feldman, *Appl. Phys. Lett.*, **61**, 1992, 540.
- Green, J., and J. Lee, *Positronium Chemistry*, Academic, New York, 1964.
- Greenwood, G.W., and A. Boltax, *J. Nucl. Mater.*, **5**, 1962, 234.
- Greuter, M.J.W., G.L. Zhang, L. Niesen, F.J.M. Buters, and A. van Veen, in: *Fundamental Aspects of Inert Gases in Solids*, NATO ASI Series B, **279**, eds. S.E. Donnelly, and J.H. Evans, Plenum Press, New York, 1991.
- Greuter, M.J.W., L. Niesen, R.A. Hakvoort, J. de Roode, A. van Veen, A.J.M. Berntsen, and W.G. Sloof, to be published in: *Proc. 9th Int. Conf. on Hyperfine Interactions*, August 17–21, 1992, Osaka, Japan.
- Greuter, M.J.W., *Inert Gases in Metals and Semiconductors*, thesis, Groningen University, Groningen, 1993.
- Greuter, M.J.W., L. Niesen, A. van Veen, M. Verwerft, and J.Th.M. de Hosson, *Proc. E-MRS Spring Meeting*, Straatsburg, May 4–7, 1993.
- Griffioen, G.C., J.H. Evans, P.C. de Jong, and A. van Veen, *Nucl. Instr. and Meth. B*, **27**, 1987, 417.
- Guinier, A., *Ann. Phys. (Paris)*, **12**, 1939, 161.
- Gullikson, E.M., and A.P. Mills jr., *Phys. Rev. Lett.*, **57**, 1986, 376.
- Gullikson, E.M., and A.P. Mills jr., *Phys. Rev. B*, **36**, 1987, 8777.
- Gullikson, E.M., A.P. Mills jr., and C.A. Murray, *Phys. Rev. B*, **38**, 1988a, 1705.
- Gullikson, E.M., A.P. Mills jr., and J.M. Phillips, *Surf. Sci.*, **195**, 1988b, L150.
- Gurp, G.J., W.F. van der Weg, and D. Sigurd, *J. Appl. Phys.*, **49**, 1978, 4011.
- Habraken, F.H.P.M., A.E.T. Kuiper, A. van Oostrom, Y. Tamminga, and J.B. Theeten, *J. Appl. Phys.*, **53**, 1982, 404.
- Habraken, F.H.P.M., R.H.G. Tijhaar, W.F. van der Weg, A.E.T. Kuiper, and M.F.C. Willemsen, *J. Appl. Phys.*, **59**, 1986, 447.
- Habraken, F.H.P.M., M. Heyns, H.E. Macs, R. de Keersmaecker, A.E.T. Kuiper, and W.F. van der Weg, in: *Low Pressure Chemical Vapor Deposited Silicon Oxynitride Films, Material and Applications*, ed. F.H.P.M. Habraken, Research Reports ESPRIT, Springer, Heidelberg, 1991.
- Häkkinen, H., S. Mäkinen, and M. Manninen, *Phys. Rev. B*, **41**, 1990, 12441.

- Hakvoort, R.A., H. Schut, A. van Veen, W.M. Arnold Bik, and F.H.P.M. Habraken, *Appl. Phys. Lett.*, **59**, 1991, 1687.
- Hakvoort, R.A., S. Roorda, A. van Veen, M.J. van den Boogaard, F.J.M. Buters, and H. Schut, *Mater. Sci. Forum*, **105–110**, 1992a, 1391.
- Hakvoort, R.A., A. van Veen, H. Schut, M.J. van den Boogaard, A.J.M. Berntsen, S. Roorda, P.A. Stolk, and A.H. Reader, to be published in: *Proc. SLOPOS5*, August 6–10, 1992b, Jackson WY.
- Hansen, H.E., H. Rajainmäki, R. Talja, M.D. Bentzon, R.M. Nieminen, and K. Petersen, *J. Phys. F: Met. Phys.*, **15**, 1985, 1.
- Hartley, N.E.W., in: *Ion Implantation, Treatise on Materials Science and Technology*, **18**, ed. J.K. Hirvonen, Academic, New York, 1980.
- Hasegawa, M., S. Berko, and E. Kuramoto, in: *Positron Annihilation*, Proc. ICPA-8, eds. L. Dorikens-Vanpraet, M. Dorikens, and D. Segers, World Scientific, Singapore, 1989.
- Hashimoto, E., and T. Kino, *J. Phys. Soc. Japan*, **60**, 1991, 3167.
- Hautojärvi, P., *Positrons in Solids*, Springer-Verlag, Berlin, 1979.
- Hautojärvi, P., P. Huttunen, J. Mäkinen, E. Punkka, and A. Vehanen, *Mater. Res. Soc. Symp. Proc.*, **104**, 1988, 105.
- He, Y.H., M. Hasegawa, R. Lee, S. Berko, D. Adler, and A.L. Jung, *Phys. Rev. B*, **33**, 1986, 5924.
- Heidemann, K.F., M. Grüner, and E. te Kaat, *Radiat. Eff.*, **82**, 1984, 103.
- Hensel, J.C., R.T. Tung, J.M. Poate, and F.C. Unterwald, *Appl. Phys. Lett.*, **44**, 1984, 913.
- Henz, J., M. Ospelt, and H. von Känel, *Surf. Sci.*, **211–212**, 1989, 716.
- Heyns, M., J. Remmerie, E. Dooms, H. Maes, and R. de Keersmaecker, in: *Low Pressure Chemical Vapor Deposited Silicon Oxynitride Films, Material and Applications*, ed. F.H.P.M. Habraken, Research Reports ESPRIT, Springer, Heidelberg, 1991.
- Hirvonen, J.K., *J. Vac. Sci. Technol.*, **15**, 1978, 1662.
- Hodges, C.H., *Phys. Rev. Lett.*, **25**, 1970, 284.
- Hoheneinzer, C., A.R. Arends, H. de Waard, H.G. Devare, F. Pleiter, and S.A. Drentje, *Hyperfine Interactions*, **3**, 1977, 297.
- Hoven, G.N. van den, Z.N. Liang, L. Niesen, and J.S. Custer, *Phys. Rev. Lett.*, **68**, 1992, 3714.
- Howell, R., I.J. Rosenberg, and M.J. Fluss, *Phys. Rev. B*, **34**, 1986, 3069.
- Hsia, S.L., T.Y. Tan, P. Smith, and G.E. McGuire, *J. Appl. Phys.*, **70**, 1991, 7579.
- Hsia, S.L., T.Y. Tan, P. Smith, and G.E. McGuire, *J. Appl. Phys.*, **72**, 1992, 1864.
- Huang, L.J., W.M. Lau, P.J. Simpson, and P.J. Schultz, *Phys. Rev. B*, **46**, 1992, 4086.
- Huomo, H., A. Vehanen, M.D. Bentzon, and P. Hautojärvi, *Phys. Rev. B*, **35**, 1987, 8252.
- Huomo, H., E. Soininen, and A. Vehanen, *Appl. Phys. A*, **49**, 1989, 647.

- Huttunen, P.A., J. Mäkinen, and A. Vehanen, *Phys. Rev. B*, **41**, 1990a, 8062.
- Huttunen, P.A., J. Mäkinen, D.T. Britton, E. Soininen, and A. Vehanen, *Phys. Rev. B*, **42**, 1990b, 1560.
- Iverson, R.B., and R. Reif, *J. Appl. Phys.*, **62**, 1987, 1675.
- Jackman, T.E., G.C. Aers, M.W. Denhoff, and P.J. Schultz, *Appl. Phys. A*, **49**, 1989, 335.
- Jackman, T.E., G.C. Aers, J.P. McCaffrey, D.T. Britton, P. Willutzki, P.J. Simpson, P.J. Schultz, and P. Mascher, *Mater. Sci. Forum*, **105–110**, 1992, 301.
- Jacobson, F.M., M. Charlton, J. Chevallier, B.I. Deutch, G. Laricchia, and M.R. Poulsen, *J. Appl. Phys.*, **67**, 1990, 575.
- Jean, Y.C., *Microchem. J.*, **42**, 1990, 72.
- Jensen, K.O., and R.M. Nieminen, *Phys. Rev. B*, **36**, 1987, 8219.
- Jensen, K.O., M. Eldrup, B.N. Singh, and M. Victoria, *J. Phys. F: Met. Phys.*, **18**, 1988a, 1069.
- Jensen, K.O., M. Eldrup, N.J. Pedersen, and J.H. Evans, *J. Phys. F: Met. Phys.*, **18**, 1988b, 1703.
- Jensen, K.O., M. Eldrup, S. Linderoth, and J.H. Evans, *J. Phys.: Condens. Matter*, **2**, 1990, 2081.
- Jensen, K.O., and A.B. Walker, *J. Phys.: Condens. Matter*, **2**, 1990, 9757.
- Jensen, K.O., A.B. Walker, and N. Bouarissa, in: *Positron Beams for Solids and Surfaces*, *AIP Conf. Proc.*, **218**, eds. P.J. Schultz, G.R. Massoumi, and P.J. Simpson, AIP, New York, 1990.
- Jibaly, M., E.C. Kellogg, A. Weiss, A.R. Koymen, D. Mehl, and L. Stiborek, *Mater. Sci. Forum*, **105–110**, 1992, 1399.
- Johnson, N.M., C. Herring, and D.J. Chadi, *Phys. Rev. Lett.*, **56**, 1986, 769.
- Johnson, N.M., F.A. Ponce, R.A. Street, and R.J. Nemanich, *Phys. Rev. B*, **35**, 1987, 4166.
- Johnson, N.M., C. Doland, F. Ponce, J. Walker, and G. Anderson, *Physica B*, **170**, 1991, 3.
- Jones, R., *Physica B*, **170**, 1991, 181.
- Jork, H., H. Kibbel, F. Schäffler, and H.J. Herzog, *Thin Solid Films*, **183**, 1989, 307.
- Jousse, D., J. Kanicki, and J.H. Stathis, *Appl. Surf. Sci.*, **39**, 1989, 412.
- Kakalios, J., R.A. Street, and W.B. Jackson, *Phys. Rev. Lett.*, **59**, 1987, 1037.
- Kamigaki, Y., S. Minami, and H. Kato, *J. Appl. Phys.*, **68**, 1990, 2211.
- Känel, H. von, J. Henz, M. Ospelt, and P. Wachter, *Physica Scripta*, **T19A**, 1987, 158.
- Känel, H. von, J. Henz, M. Ospelt, J. Hugi, E. Müller, N. Onda, and A. Grhule, *Thin Solid Films*, **184**, 1990, 295.
- Karavaev, V.V., N.V. Kuznetsov, and V.N. Filatov, *Sov. Phys. Semicond.*, **24**, 1990, 778.
- Keinonen, J., M. Hautala, E. Rauhala, M. Erola, J. Lahtinen, H. Huomo, A. Vehanen, and P. Hautojärvi, *Phys. Rev. B*, **36**, 1987, 1344.

- Keinonen, J., M. Hautala, E. Rauhala, V. Karttunen, A. Kuronen, J. Räisänen, J. Lahtinen, A. Vehanen, E. Punkka, and P. Hautojärvi, *Phys. Rev. B*, **37**, 1988, 8269.
- Kong, Y., and K.G. Lynn, *Phys. Rev. B*, **41**, 1990a, 6179.
- Kong, Y., and K.G. Lynn, *Phys. Rev. B*, **41**, 1990b, 6185.
- Kratky, O., in: *Small Angle X-Ray Scattering*, eds. O. Glatter and O. Kratky, Academic, London, 1982.
- Krick, D.T., P.M. Lenahan, and J. Kanicki, *Phys. Rev. B*, **38**, 1988, 8226.
- Lahtinen, J., and A. Vehanen, *Catalysis Lett.*, **8**, 1991, 67.
- Lannin, J.S., in: *Semiconductors and Semimetals*, **21**, *Hydrogenated Amorphous Silicon*, part B, Academic, London, 1984.
- Lau, S.S., J.W. Mayer, and K.N. Tu, *J. Appl. Phys.*, **49**, 1978, 4005.
- La Via, F., A.H. Reader, J.P.W.B. Duchateau, E.P. Naburgh, D.J. Oostra, and A.J. Kinneging, *J. Vac. Sci. Technol. B*, **10**, 1992, 2284.
- La Via, F., C. Spinella, A.H. Reader, J.P.W.B. Duchateau, R.A. Hakvoort, and A. van Veen, to be published in: *J. Vac. Sci. Technol. B*.
- La Via, F., C. Spinella, A.H. Reader, J.P.W.B. Duchateau, R.A. Hakvoort, and A. van Veen, to be published in: *Appl. Surf. Sci.*
- Lawrence, M., A. Dass, D.B. Fraser, and C.S. Wei, *Appl. Phys. Lett.*, **58**, 1991, 1308.
- Lee, J.L., L. Wei, S. Tanigawa, H. Oigawa, and Y. Nannichi, *Jpn. J. Appl. Phys.*, **30**, 1991, L138.
- Leo, P.H., K.D. Moore, P.L. Jones, and F.H. Cocks, *Phys. Status Solidi B*, **108**, 1981, K145.
- Linnros, J., W.L. Brown, and R.G. Elliman, *Mater. Res. Soc. Symp. Proc.*, **100**, 1988, 369.
- Logan, L.R., P.J. Schultz, J.A. Davies, and T.E. Jackman, *Nucl. Instr. and Meth. B*, **33**, 1988, 58.
- Lopes Gil, C., M.F. Ferreira Margues, A.P. de Lima, R. Villar, A.M. de Deus, G. Kögel, and W. Triftshäuser, *Mater. Sci. Forum*, **105–110**, 1992, 1141.
- Lynn, K.G., *Phys. Rev. Lett.*, **43**, 1979, 391.
- Lynn, K.G., T. McKay, and Bent Nielsen, *Phys. Rev. B*, **36**, 1987, 7107.
- Lynn, K.G., Bent Nielsen, and D.O. Welch, *Can. J. Phys.*, **67**, 1989, 818.
- Lyons, W., A.S.T. James, R.K. MacCrone, H. Bakhru, S. Sen, W. Gibson, C. Bur, A.J. Kurnick, and G.E. Welch, *Thin Solid Films*, **84**, 1982, 347.
- MacKenzie, I.K., J.A. Eady, and R.R. Gingerich, *Phys. Lett. A*, **33**, 1970, 279.
- Maex, K., A.E. White, K.T. Short, Y.F. Hsieh, and R. Hull, *J. Appl. Phys.*, **68**, 1990, 5641.
- Mahan, A.H., Y. Chen, D.L. Williamson, and G.D. Mooney, *J. Non-Cryst. Solids*, **137–138**, 1991, 65.
- Mäkinen, J., E. Punkka, A. Vehanen, P. Hautojärvi, J. Keinonen, M. Hautala, and E. Rauhala, *J. Appl. Phys.*, **67**, 1990a, 990.
- Mäkinen, J., C. Corbel, P. Hautojärvi, A. Vehanen, and D. Mathiot, *Phys. Rev. B*, **42**, 1990b, 1750.

- Mäkinen, J., C. Corbel, P. Hautojärvi, and D. Mathiot, *Phys. Rev. B*, **43**, 1991, 12114.
- Mäkinen, S., H. Rajainmäki, and S. Linderoth, *Phys. Rev. B*, **42**, 1990, 11166.
- Mäkinen, S., H. Rajainmäki, and S. Linderoth, *Phys. Rev. B*, **40**, 1991, 5510.
- Maréc, C.H.M., W.M. Arnold Bik, A.E.T. Kuiper, and F.H.P.M. Habraken, *Proc. Insulating Films on Semiconductors*, 1991.
- Markworth, A.J., *Metallurgical Trans.*, **4**, 1973, 2651.
- Mascher, P., S. Dannefaer, and D. Kerr, *Phys. Rev. B*, **40**, 1989, 11764.
- Massoumi, G.R., N. Hozhabri, W.N. Lennard, P.J. Schultz, S.F. Baert, H.H. Jorch, and A.H. Weiss, *Rev. Sci. Instrum.*, **62**, 1991, 1460.
- Massoumi, G.R., N. Hozhabri, K.O. Jensen, W.N. Lennard, M.S. Lorenzo, P.J. Schultz, and A.B. Walker, *Phys. Rev. Lett.*, **68**, 1992, 3873.
- Mayer, W., D. Grasse, and J. Peisl, *Radiat. Eff.*, **84**, 1985, 107.
- McMullen, T., in: *Positron Annihilation*, eds. P.C. Jain, R.M. Singru, and K.P. Gopinathan, World Scientific Publ. Co., Singapore, 1985.
- Merrison, J.P., M. Charlton, B.I. Deutch, and L.V. Jørgensen, *J. Phys.: Condens. Matter*, **4**, 1992, L207.
- Merzbacher, E., *Quantum Mechanics*, John Wiley, New York, 1970.
- Meyer, M.A., and J.J.A. Smit, *Nucl. Phys. A*, **205**, 1973, 177.
- Mikkola, D.E., and J.B. Cohen, in: *Local Atomic Arrangements studied by X-Ray Diffraction*, eds. J.B. Cohen and J.E. Illiardi, *Metall. Soc. Conf.*, **36**, Gordon and Breach, New York, 1966.
- Mills, A.P., jr., *Phys. Rev. Lett.*, **41**, 1978, 1828.
- Mills, A.P., jr., *Hyperfine Interactions*, **44**, 1988, 107.
- Mills, A.P., jr., *Mater. Sci. Forum*, **105-110**, 1992, 101.
- Mitchell, I.V., P.J. Simpson, P.J. Schultz, M. Vos, U. Akano, and C. Wu, in: *Positron Beams for Solids and Surfaces*, *AIP Conf. Proc.*, **218**, eds. P.J. Schultz, G.R. Massoumi, and P.J. Simpson, AIP, New York, 1990.
- Mitra, S., X.L. Wu, R. Shinar, and J. Shinar, *Mater. Res. Soc. Symp. Proc.*, **149**, 1989, 595.
- Mitra, S., R. Shinar, and J. Shinar, *Phys. Rev. B*, **42**, 1990, 6746.
- Mogensen, O.E., *J. Chem. Phys.*, **60**, 1974, 998.
- Motoko-Kwete, D. Segers, M. Dorikens, L. Dorikens-Vanpraet, P. Clauws, and I. Lemahieu, in: *Positron Annihilation*, Proc. ICPA-8, eds. L. Dorikens-Vanpraet, M. Dorikens, and D. Segers, World Scientific, Singapore, 1989.
- Motoko-Kwete, D. Segers, M. Dorikens, L. Dorikens-Vanpraet, P. Clauws, and D. Geshef, *Phys. Lett. A*, **150**, 1990, 413.
- Müller, G., and S. Kalbitzer, *Phil. Mag.*, **41**, 1980, 307.
- Müller, G., *Appl. Phys. A*, **45**, 1988, 41.
- Murarka, S.P., *J. Vac. Sci. Technol.*, **17**, 1980, 775.
- Myers, S.M., D.M. Follstaedt, H.J. Stein, and W.R. Wampler, *Phys. Rev. B*, **45**, 1992a, 3914.
- Myers, S.M., D.M. Follstaedt, H.J. Stein, and W.R. Wampler, *Mater. Sci. Forum*, **83-87**, 1992b, 81

- Nasu, H., M. Watanabe, K. Shizuma, T. Imura, Y. Osaka, and H. Hasai, *Yogyo-Kyokai-Shi*, **95**, 1987, 5.
- Nielsen, Bent, K.G. Lynn, A. Vehanen, and P.J. Schultz, *Phys. Rev. B*, **32**, 1985a, 2296.
- Nielsen, Bent, A. van Veen, and K.G. Lynn, in: *Positron Annihilation*, eds. P.C. Jain, R.M. Singru, and K.P. Gopinathan, World Scientific Publ. Co., Singapore, 1985b.
- Nielsen, Bent, K.G. Lynn, and Y.C. Chen, *Phys. Rev. Lett.*, **57**, 1986, 1789.
- Nielsen, Bent, K.G. Lynn, T.C. Leung, D.O. Welch, and G. Rubloff, *Phys. Rev. B*, **40**, 1989, 1434.
- Nielsen, Bent, presented at Ion-Beam Modification of Materials, Knoxville TN, 1990 (*unpublished*).
- Nielsen, Bent, K.G. Lynn, T.C. Leung, G.J. van der Kolk, and L.J. van IJzen-doorn, *Appl. Phys. Lett.*, **56**, 1990, 728.
- Nieminen, R.M., and J. Laakkonen, *Appl. Phys.*, **20**, 1979, 181.
- Nieminen, R.M., and M.J. Manninen, in: *Positrons in Solids*, ed. P. Hautojärvi, Springer-Verlag, Berlin, 1979.
- Nieminen, R.M., and J. Oliva, *Phys. Rev. B*, **22**, 1980, 2226.
- Noordhuis, J., *Laser Treatment of Metals*, thesis, Groningen University, Groningen, 1993.
- Ohmi, T., K. Hashimoto, M. Morita, and T. Shibata, *J. Appl. Phys.*, **69**, 1991, 2062.
- Olson, G.L., and J.A. Roth, *Mater. Sci. Rep.*, **3**, 1988, 1.
- Ommen, A.H. van, C.W.T. Bulle-Lieuwma, and C. Langereis, *J. Appl. Phys.*, **64**, 1988a, 2706.
- Ommen, A.H. van, J.J. Ottenheim, A.M.L. Theunissen, and G. Mouwen, *Appl. Phys. Lett.*, **53**, 1988b, 669.
- Ommen, A.H. van, J.J. Ottenheim, C.W.T. Bulle-Lieuwma, and A.M.L. Theunissen, *Appl. Surf. Sci.*, **38**, 1989, 197.
- Oude Elferink, J.B., U.A. van der Heide, W.M. Arnold Bik, F.H.P.M. Habraken, and W.F. van der Weg, *Appl. Surf. Sci.*, **30**, 1987, 197.
- Palathingal, J.C., P. Asoka-Kumar, K.G. Lynn, Y. Posada, and X.Y. Wu, *Phys. Rev. Lett.*, **67**, 1991, 3491.
- Pankove, J.I., D.E. Carlson, D.E. Berkeyheiser, and R.O. Wance, *Phys. Rev. Lett.*, **51**, 1983, 2224.
- Pankove, J.I., *Mater. Res. Soc. Symp. Proc.*, **262**, 1992, 357.
- Pantelides, S.T., *Phys. Rev. Lett.*, **57**, 1986, 2979.
- Pantelides, S.T., *Appl. Phys. Lett.*, **50**, 1987, 995.
- Park, Y.K., J.T. Waber, M. Meshii, C.L. Snead, and C.G. Park, *Phys. Rev. B*, **34**, 1986, 823.
- Pearton, S.J., *Mater. Res. Soc. Symp. Proc.*, **59**, 1986, 457.
- Pearton, S.J., J.W. Corbett, and T.S. Shi, *Appl. Phys. A*, **43**, 1987, 153.
- Perkins, A., and J.P. Carbotte, *Phys. Rev. B*, **1**, 1970, 101.

- Perovic, D.D., G.C. Weatherly, P.J. Simpson, P.J. Schultz, T.E. Jackman, G.C. Aers, J.P. Noël, and D.C. Houghton, *Phys. Rev. B*, **43**, 1991, 14257.
- Phillips, J.C., *Phys. Rev. Lett.*, **58**, 1987, 2824.
- Platzman, P.M., and N. Tzoar, *Phys. Rev. B*, **33**, 1986, 5900.
- Poate, J.M., K.N. Tu, and J.W. Mayer, *Thin Films, Interdiffusion and Reactions*, John Wiley, New York, 1978.
- Polman, A., D.C. Jacobson, S. Coffa, J.M. Poate, S. Roorda, and W.C. Sinke, *Appl. Phys. Lett.*, **57**, 1990, 1230.
- Porter, D.A., and K.E. Easterling, *Phase Transformations in Metals and Alloys*, Van Nostrand Reinhold Co., New York, 1981.
- Press, W.H., B.P. Flannery, S.A. Teukolsky and W.T. Vetterling, *Numerical Recipes, the Art of Scientific Computing*, Cambridge University Press, Cambridge, 1986.
- Puska, M.J., and R.M. Nieminen, *J. Phys. F*, **13**, 1983, 333.
- Puska, M.J., P. Lanki, and R.M. Nieminen, *J. Phys.: Condens. Matter*, **1**, 1989, 6081.
- Puska, M.J., C. Corbel, and R.M. Nieminen, *Phys. Rev. B*, **41**, 1990, 9980.
- Puska, M.J., *J. Phys.: Condens. Matter*, **3**, 1991, 3455.
- Rai, A.K., J. Baker, and D.C. Ingram, *Appl. Phys. Lett.*, **51**, 1987, 172.
- Rajainmäki, H., S. Linderöth, H.E. Hansen, R.M. Nieminen, and M.D. Bentzon, *Phys. Rev. B*, **38**, 1988, 1087.
- Reader, A.H., J.P.W.B. Duchateau, J.E. Crombeen, E.P. Naburgh, and M.A.J. Somers, *Appl. Surf. Sci.*, **53**, 1991, 92.
- Rehm, W., and R. Fischer, *Phys. Status Solidi B*, **94**, 1979, 595.
- Reinmiller, J., H.E. Maes, M. Heyns, R. de Keersmaecker, F.H.P.M. Habraken, J.B. Oude Elferink, W.F. van der Weg, and A.E.T. Kuiper, in: *Silicon Nitride and Silicon Dioxide Thin Insulating Films*, Proc. **87-10**, eds. V.J. Kapoor and K.T. Hankins, The Electrochem. Soc., Pennington NJ, 1987.
- Robertson, J., and M.J. Powell, *Appl. Phys. Lett.*, **44**, 1984, 415.
- Roorda, S., *Relaxation and Crystallization of Amorphous Silicon*, thesis, Utrecht University, Utrecht, 1990.
- Roorda, S., J.M. Poate, D.C. Jacobson, D.J. Eaglesham, B.S. Dennis, S. Dierker, W.C. Sinke, and F. Spaepen, *Solid State Commun.*, **75**, 1990a, 197.
- Roorda, S., J.M. Poate, D.C. Jacobson, B.S. Dennis, S. Dierker, and W.C. Sinke, *Appl. Phys. Lett.*, **56**, 1990b, 2097.
- Roorda, S., W.C. Sinke, J.M. Poate, D.C. Jacobson, S. Dierker, B.S. Dennis, D.J. Eaglesham, F. Spaepen, and P. Fuoss, *Phys. Rev. B*, **44**, 1991, 3702.
- Roorda, S., P.A. Stolck, R.A. Hakvoort, and A. van Veen, *Mater. Res. Soc. Symp. Proc.*, **235**, 1992a, 39.
- Roorda, S., R.A. Hakvoort, A. van Veen, P.A. Stolck, and F.W. Saris, *J. Appl. Phys.*, **72**, 1992b, 5145.
- Rothaut, J., H. Schroeder, and H. Ullmaier, *Phil. Mag. A*, **47**, 1983, 781.
- Roziing, G.J., A.W. Weeber, P.E. Mijnders, A. van Veen, J. de Vries, and H. Schut, *Mater. Sci. Forum*, **105-110**, 1992, 1205.

- Ruault, M.O., J. Chaumont, and H. Bernas, *Nucl. Instr. and Meth.*, **209/210**, 1983, 351.
- Rubaszek, A., *Phys. Rev. B*, **44**, 1991, 10857.
- Rubloff, G.W., Bent Nielsen, K.G. Lynn, D.O. Welch, and T.C. Leung, *Vacuum*, **41**, 1990, 790.
- Sah, C.T., J.Y.C. Sun, and J.J.T. Tzou, *Appl. Phys. Lett.*, **43**, 1983, 204.
- Saitoh, S., T. Sugii, H. Ishiware, and S. Furukawa, *Jpn. J. Appl. Phys.*, **20**, 1981, L130.
- Schaefer, H.E., R. Würschum, R. Schwarz, D. Slobodin, and S. Wagner, *Appl. Phys. A*, **40**, 1986, 145.
- Schaffer, J.P., A.J. Perry, and J. Brunner, *J. Vac. Sci. Technol. A*, **10**, 1992, 193.
- Scher, H., and E.W. Montroll, *Phys. Rev. B*, **12**, 1975, 2455.
- Schultz, P.J., K.G. Lynn, and H.H. Jorch, in: *Proc. Int. Workshop 'Slow Positrons in Surface Science'*, ed. A. Vehanen, report 135, Helsinki University of Technology, Espoo, 1984.
- Schultz, P.J., and J.L. Campbell, *Phys. Lett. A*, **112**, 1985, 316.
- Schultz, P.J., and K.G. Lynn, *Rev. Mod. Phys.*, **60**, 1988, 701.
- Schultz, P.J., E. Tandberg, Bent Nielsen, T.E. Jackman, M.W. Denhoff, and G.C. Aers, *Phys. Rev. Lett.*, **61**, 1988a, 187.
- Schultz, P.J., L.R. Logan, T.E. Jackman, and J.A. Davies, *Phys. Rev. B*, **38**, 1988b, 6369.
- Schultz, P.J., and C.L. Snead, *Metallurgical Trans. A*, **21A**, 1990, 1121.
- Schut, H., *A Variable Energy Positron Beam Facility with Applications in Materials Science*, thesis, Delft University of Technology, Delft, 1990.
- Schut, H., A. van Veen, G.F.A. van de Walle, and A.A. van Gorkum, *J. Appl. Phys.*, **70**, 1991, 3003.
- Schut, H., A. van Veen, R.A. Hakvoort, M.J.W. Greuter, and L. Niesen, to be published in: *Proc. SLOPOS5*, August 6-10, 1992, Jackson WY.
- Seager, C.H., and R.A. Anderson, *Appl. Phys. Lett.*, **53**, 1988, 1181.
- Seeger, A., F. Banhart, and W. Bauer, in: *Positron Annihilation*, Proc. ICPA-8, eds. L. Dorikens-Vanpraet, M. Dorikens, and D. Segers, World Scientific, Singapore, 1989.
- Seeger, A., and F. Banhart, *Helvetica Physica Acta*, **63**, 1990, 403.
- Shi, T.S., S.N. Sahu, J.W. Corbett, and L.C. Snyder, *Scientia Sinica*, **27**, 1984, 98.
- Shimotamai, M., Y. Ohgino, H. Fukushima, Y. Nagayasu, T. Mihara, K. Inoue, and M. Doyama, *Inst. Phys. Conf. Ser.*, **59**, 1981, 241.
- Shinar, J., R. Shinar, S. Mitra, and J.Y. Kim, *Phys. Rev. Lett.*, **62**, 1989, 2001.
- Simpson, P.J., P.J. Schultz, T.E. Jackman, G.C. Aers, J.P. Noël, D.C. Houghton, D.D. Perovic, and G.C. Weatherly, in: *Positron Beams for Solids and Surfaces*, *AIP Conf. Proc.*, **218**, eds. P.J. Schultz, G.R. Massoumi, and P.J. Simpson, AIP, New York, 1990.
- Simpson, P.J., M. Vos, I.V. Mitchell, C. Wu, and P.J. Schultz, *Phys. Rev. B*, **44**, 1991, 12180.

- Simpson, P.J., M. Vos, I.V. Mitchell, C. Wu, and P.J. Schultz, *Mater. Sci. Forum*, **105–110**, 1992, 1439.
- Sinke, W.C., T. Warabisako, M. Miyao, T. Tokuyama, S. Roorda, and F.W. Saris, *J. Non-Cryst. Solids*, **99**, 1988, 308.
- Smith, D.L., P.C. Rice-Evans, D.T. Britton, J.H. Evans, and A. Allen, *Phil. Mag. A*, **61**, 1990a, 839.
- Smith, D.L., C. Smith, H.E. Evans, P.C. Rice-Evans, and J.H. Evans, in: *Positron Beams for Solids and Surfaces*, *AIP Conf. Proc.*, **218**, eds. P.J. Schultz, G.R. Massoumi, and P.J. Simpson, AIP, New York, 1990b.
- Smith, D.L., H. Evans, C. Smith, P.C. Rice-Evans, and J.H. Evans, *Mater. Sci. Forum*, **105–110**, 1992, 1447.
- Snead, C.L., A.N. Goland, and F.W. Wiffen, *J. Nucl. Mater.*, **64**, 1977, 195.
- Soininen, E., H. Huomo, P.A. Huttunen, J. Mäkinen, A. Vehanen, and P. Hautojärvi, *Phys. Rev. B*, **41**, 1990, 6227.
- Soininen, E., J. Mäkinen, D. Beyer, and P. Hautojärvi, *Phys. Rev. B*, **46**, 1992, 13104.
- Spear, W.E., and P.G. Lecomber, *Solid State Commun.*, **17**, 1975, 1193.
- Steindl, R., G. Kögel, P. Sperr, P. Willutzki, D.T. Britton, and W. Triftshäuser, *Mater. Sci. Forum*, **105–110**, 1992, 1455.
- Stevens, J.R., *Methods Exper. Phys.*, **16A**, 1980, 371.
- Stewart, A.T., C.V. Briscoe, and J.J. Steinbacher, *Can. J. Phys.*, **68**, 1990, 1362.
- Stolk, P.A., L. Calcagnile, S. Roorda, W.C. Sinke, A.J.M. Berntsen, and W.F. van der Weg, *Appl. Phys. Lett.*, **60**, 1992a, 1688.
- Stolk, P.A., S. Roorda, L. Calcagnile, W.C. Sinke, H.B. van Linden van den Heuvell, and F.W. Saris, *Mater. Res. Soc. Symp. Proc.*, **205**, 1992b, 15.
- Stolk, P.A., L. Calcagnile, S. Roorda, H.B. van Linden van den Heuvell, and F.W. Saris, *Mater. Res. Soc. Symp. Proc.*, **235**, 1992c, 15.
- Stolk, P.A., *Optical Probing of Defects in Amorphous Silicon*, thesis, Utrecht University, Utrecht, 1993.
- Street, R.A., *Hydrogenated Amorphous Silicon*, Cambridge University Press, Cambridge, 1991a.
- Street, R.A., *Physica B*, **170**, 1991b, 69.
- Suzuki, R., Y. Kobayashi, T. Mikado, A. Matsuda, P.J. McElheny, S. Mashima, H. Ohgaki, M. Chiwaki, T. Yamazaki, and T. Tomimasu, *Jpn. J. Appl. Phys.*, **30**, 1991, 2438.
- Tabuki, Y., L. Wei, S. Tanigawa, R. Nagai, and E. Takeda, *Mater. Sci. Forum*, **105–110**, 1992, 1467.
- Tamura, M., and T. Suzuki, *Nucl. Instr. and Meth. B*, **39**, 1989, 318.
- Tandberg, E., P.J. Schultz, G.C. Aers, and T.E. Jackman, *Can. J. Phys.*, **67**, 1989, 275.
- Tao, S.J., *J. Chem. Phys.*, **56**, 1972, 5499.
- Thomas, P.A., M.H. Brodsky, D. Kaplan, and D. Lepine, *Phys. Rev. B*, **18**, 1978, 3059.
- Tong, B.Y., *Phys. Rev. B*, **5**, 1972, 1436.

- Trumpy, G., in: *Positron Annihilation*, Proc. ICPA-8, eds. L. Dorikens-Vanpraet, M. Dorikens, and D. Segers, World Scientific, Singapore, 1989.
- Tsai, C.J., H.A. Atwater, and T. Vreeland, *Appl. Phys. Lett.*, **57**, 1990, 2305.
- Tung, R.T., J.M. Poate, J.C. Bean, J.M. Gibbison, and D.C. Jacobson, *Thin Solid Films*, **93**, 1982a, 77.
- Tung, R.T., J.C. Bean, J.M. Gibbison, J.M. Poate, and D.C. Jacobson, *Appl. Phys. Lett.*, **40**, 1982b, 684.
- Turnbull, D., *Mater. Res. Soc. Symp. Proc.*, **51**, 1986, 71.
- Uedono, A., S. Tanigawa, and H. Sakairi, *J. Nucl. Mater.*, **173**, 1990, 307.
- Uedono, A., S. Tanigawa, and H. Sakairi, *J. Nucl. Mater.*, **184**, 1991a, 191.
- Uedono, A., L. Wei, C. Doshio, H. Kondo, S. Tanigawa, and M. Tamura, *Jpn. J. Appl. Phys.*, **30**, 1991b, 1597.
- Uedono, A., L. Wei, S. Tanigawa, J. Sugiura, M. Ogasawara, and M. Tamura, *Rad. Effects*, **124**, 1992, 31.
- Valkealahti, S., and R.M. Nieminen, *Appl. Phys. A*, **32**, 1983, 95.
- Valkealahti, S., and R.M. Nieminen, *Appl. Phys. A*, **35**, 1984, 51.
- Veen, A. van, A. Warnaar, and L.M. Caspers, *Vacuum*, **30**, 1980, 109.
- Veen, A. van, W.Th.M. Buters, G.J. van der Kolk, L.M. Caspers, and T.M. Armstrong, *Nucl. Instr. and Meth.*, **194**, 1982, 485.
- Veen, A. van, in: *Erosion and Growth of Solids Stimulated by Atom and Ion Beams*, NATO ASI series E, **112**, eds. G. Kiriakidis, G. Carter, and J.L. Whittton, M. Nijhoff Publ., Dordrecht, 1986.
- Veen, A. van, P.C. de Jong, K.R. Bijkerk, H.A. Filius, and J.H. Evans, *Mater. Res. Soc. Symp. Proc.*, **100**, 1988, 231.
- Veen, A. van, *J. Trace and Microprobe Techniques*, **8**, 1990, 1.
- Veen, A. van, H. Schut, J. de Vries, R.A. Hakvoort, and M.R. Ijpma, in: *Positron Beams for Solids and Surfaces*, AIP Conf. Proc., **218**, eds. P.J. Schultz, G.R. Massouini, and P.J. Simpson, AIP, New York, 1990.
- Veen, A. van, in: *Fundamental Aspects of Inert Gases in Solids*, NATO ASI Series B, **279**, eds. S.E. Donnelly, and J.H. Evans, Plenum Press, New York, 1991.
- Veen, A. van, M.J.W. Greuter, L. Niesen, Bent Nielsen, and K.G. Lynn, *Mater. Res. Soc. Symp. Proc.*, **262**, 1992, 181.
- Vehanen, A., P. Hautojärvi, J. Johansson, and J. Yli-Kaupilla, *Phys. Rev. B*, **25**, 1982, 762.
- Vehanen, A., K. Saarinen, P. Hautojärvi, and H. Huomo, *Phys. Rev. B*, **35**, 1987, 4606.
- Volkert, C.A., and A. Polman, *Mater. Res. Soc. Symp. Proc.*, **235**, 1992, 3.
- Vries, J. de, *Positron Lifetime Technique with Applications in Materials Science*, *thesis*, Delft University of Technology, Delft, 1987.
- Waard, H. de, F. Pleiter, L. Niesen, and D.W. Hafemeister, *Hyperfine Interactions*, **10**, 1981, 643.
- Wagner, H., and W. Beyer, *Solid State Commun.*, **48**, 1983, 585.

- Walker, A.B., and K.O. Jensen, in: *Positron Beams for Solids and Surfaces*, AIP Conf. Proc., **218**, eds. P.J. Schultz, G.R. Massoumi, and P.J. Simpson, AIP, New York, 1990.
- Walker, A.B., K.O. Jensen, J. Szymański, and D. Neilson, *Phys. Rev. B*, **46**, 1992, 1687.
- Washburn, J., C.S. Murty, D. Sadana, P. Byrne, R. Gronsky, N. Cheung, and R. Kilaas, *Nucl. Instr. and Meth.*, **209/210**, 1983, 345.
- Watkins, G.D., and J.W. Corbett, *Phys. Rev.*, **138A**, 1965, A543.
- West, R.N., in: *Positron Studies in Condensed Matter*, Monographs in Physics, eds. B.R. Coles and N. Mott, Taylor & Francis, London, 1974.
- Westbrook, C.I., D.W. Gidley, R.S. Conti, and A. Rich, *Phys. Rev. A*, **40**, 1989, 5489.
- White, A.E., K.T. Short, R.C. Dynes, J.P. Garno, and J.M. Gibbson, *Appl. Phys. Lett.*, **50**, 1987, 95.
- Wieringen, A. van, and N. Warmoltz, *Physica*, **22**, 1956, 849.
- Williamson, D.L., A.H. Mahan, B.P. Nelson, and R.S. Crandall, *Appl. Phys. Lett.*, **55**, 1989, 783.
- Williamson, G.K., and R.E. Smallman, *Phil. Mag.*, **1**, 1956, 34.
- Winer, K., *Annu. Rev. Mater. Sci.*, **21**, 1991, 1.
- Wu, M.F., A. van Tomme, H. Pattyn, G. Langouche, K. Maex, J. van Hellemont, J. Vanacken, H. Vloeberghs, and Y. Bruynseraede, *Nucl. Instr. and Meth. B*, **45**, 1990, 658.
- Würschum, E., W. Bauer, K. Maier, J. Major, A. Seeger, H. Stoll, H.D. Carstanjen, W. Decker, J. Diehl, and H.E. Schaefer, in: *Positron Annihilation*, Proc. ICPA-8, eds. L. Dorikens-Vanpraet, M. Dorikens, and D. Segers, World Scientific, Singapore, 1989.
- Yalisove, S.M., R.T. Tung, and D. Loretto, *J. Vac. Sci. Technol. A*, **7**, 1989, 1472.
- Zhang, Z., and Y. Ito, *J. Chem. Phys.*, **93**, 1990, 1021.
- Ziegler, J.F., J.P. Biersack, and U. Littmark, *The Stopping and Range of Ions in Solids* (TRIM), Pergamon, New York, 1985.

NEXT PAGE(S) left BLANK.

# Acknowledgements

Many people have collaborated on the work described in this thesis. It is a pleasure to acknowledge their contributions.

I am grateful to Tom van Veen and Hugo van Dam, who enabled me to carry out the research reported in this thesis. The intensive discussions with Tom were especially instructive and mostly very helpful. When the experimental data were seemingly inconsistent, Tom would come with some plausible interpretation, which not only accounted for my own data but was also consistent with research carried out by other groups.

The technical assistance by Karl Roos cannot easily be overrated. He has played a key role in the design and construction of the equipment for improving the beam. He is also responsible for the beautiful drawings of the VEP presented in chapter 3. Hours of intensive collaboration, enlivened by discussions on all possible topics, were alternated with times spent on solving his computer problems. In autumn, when the spring blossom has given place to fruit, the harvest of the diverse crops of our small garden often yielded many invigorating beverages.

At this point I would also like to mention Henk Schut. As my predecessor in working with the VEP, even after four years his knowledge of the pumps and valves mounted on the beam still surpasses my own. Especially his help with the use of his computer code for running automatic measurements was indispensable.

I am also indebted to many others in the group. Dick de Haas, Bob Heijenga, Ronald Otte, Jan de Roode, Kees Westerduin, and Maurits Ypma were at my beck and call. Discussions with my colleagues Harry Eleveld, Hans Filius, Tom Piters, and Leon Seijbel are gratefully

remembered. They could often make me see the funny side of my experimental problems. Peter Mijnaerends showed his erudition by his comments on positron physics as well as on English grammar, while I succeeded in convincing him of the advantages of  $\text{\LaTeX}$  above other text processors.

The research described in chapter 4 has been carried out in collaboration with the University of Groningen, The Netherlands. Especially Joeke Noordhuis exerted himself to bring the experiments off well. Many times we were close to an explanation that accounted for all our data, but then the next experiment, of course intended to confirm our hypothesis, invariably resulted in something breaking through our theory. At these times discussions with Jeff de Hosson always proved to be illuminating. The NRA measurements were carried out by Joeke in co-operation with Dik Boerma and Peter Smulders.

Chapter 6 contains the fruitful results of my collaboration with people of the FOM-Institute for Atomic and Molecular Physics (Amsterdam, The Netherlands). The many bright ideas of Sjoerd Roorda for verifying his theory of ‘defects’ in amorphous silicon proved to be really rewarding. It is a pity that he is currently employed at the University of Montréal, since his move to Canada put an end to our regular meetings. The little I know of Free-Carrier Lifetime measurements I learned from Peter Stolk. It was interesting to complement our positive defect probes with his negative electrons.

The samples of which the positron measurements are described in chapter 7, were obtained from several groups. The Kr-sputtered *a*-Si films were deposited at the Interfaculty Reactor Institute by Frans-Jan Buters and Jan de Roode. X-ray analysis and Mössbauer spectroscopy measurements were done by Marcel Greuter, while the beautiful TEM micrograph of the cross-section of these samples (figure 7.1) was made by Marc Verwerft of the University of Groningen, The Netherlands.

The hydrogenated *a*-Si samples were deposited by Wilfried van Sark at the University of Utrecht, The Netherlands. Martin van den Boogaard was a patient tutor when he taught me the basics of amorphous silicon technology. The SAXS work presented in chapter 7 was done by Martin in collaboration with Scott Jones, Yan Chen,

Luigi Greco, David Mooney, and Don Williamson of the Colorado School of Mines (Golden, Colorado, U.S.A.) and Amy Swartzlander-Franz of the National Renewable Energy Laboratory (ibid.). Martin has also checked parts of the manuscript, while I have borrowed some nice plots from his thesis [figures 2.5 and 2.6 in Van den Boogaard (1992) show up in my thesis as figures 1.1 and 2.3]. Arjan Berntsen proved to be a real expert in Raman spectroscopy, which is evident from the spectra presented in chapter 7 and his help in interpreting the data.

The sample labelled 'MBE-system grown a-Si' (which really isn't epitaxial), was prepared at the Philips Research Laboratories (Eindhoven, The Netherlands) by Alec Reader, who is also responsible for the CoSi<sub>2</sub> films of chapter 8. Especially our pleasant collaboration in the metal-silicide research was an enjoyable experience. Indeed, it is difficult not to be impressed by Alec's kindly interest and never-ceasing smile. Francesco La Via (I regret that I never met him personally) also did a good job in the CoSi<sub>2</sub> work, for which I am really grateful.

Chapter 9 reports my first positron research that was published in a journal. Although the experimental work was performed more than three years ago, the months of collaboration with Wim Arnold Bik and Frans Habraken still come to my mind as an interesting time.

I am sure I have forgotten to mention some others who have played a role in the realization of this thesis. Besides, there are so many people who have sympathized with me the last few years... To all of them I would like to say: Thank you very much! Of course, first among these are my parents, to whom this thesis is gratefully dedicated. They made it possible for me to pass through university and often gave me good advice. My wife Anja also deserves praise. Her love has been a precious treasure to me at the moments I needed a friend to talk to.

Last but not least, I would like to express my sincere gratitude toward God, Whom I serve, Who has shown His love by sending His Son, Jesus Christ, and Who has given me strength and wisdom for completing this thesis. "For the LORD gives wisdom, and from His mouth come knowledge and understanding" (Proverbs 2:6, NIV). *Soli Deo gloria!*

# Curriculum Vitae

The author of this thesis was born in Delft on June 26, 1966, The Netherlands, where he went through secondary school at the Christelijk Lyceum Delft between 1978 and 1984. Subsequently, he commenced his studies at the Delft University of Technology. His first research project concerned the study of two epitaxial systems, viz. the determination of the misorientation of a Nb/V alloy on sapphire(012) and the analysis of GaAs growth on Si(001). Upon the completion of this experimental work, the equivalent of the M.Sc. degree in technical physics was awarded him on February 28, 1989.

From May 16, 1989 to June 30, 1993 the author was employed in the Radiation Damage group of the Reactor Physics department of the Interfaculty Reactor Institute, Delft. The results of his investigations into the application of positron beams for materials research, which were performed in this group, are the subject of the present Ph.D. thesis.

## Stellingen

behorende bij het proefschrift:

### Applications of Positron Depth Profiling

1. Als het door Crone en Sher beschreven apocalyptische scenario betreffende een toekomstige fase-overgang van het heelal, waarbij het foton massa verkrijgt als gevolg van de breking van de iksymmetrie van de quantum-electrodynamica, werkelijkheid zou worden, dan zijn positron diepte-profileringsmetingen in hun huidige vorm niet langer mogelijk.

*M.M. Crone and M. Sher, Am. J. Phys., 59, 1991, 25.*

2. Aangezien de grootte van de positron-werkfunctie afhankelijk is van de vlakrichting, bevinden zich in microscopische holten in materialen elektrische velden met een component evenwijdig aan het holte-oppervlak.
3. Bij toepassing van de positron-levensduurtechniek voor karakterisering van polymeren dient men de ortho-positronium bijdrage niet te beschrijven met slechts één of twee levensduren, zoals tot nu toe gebruikelijk is, maar met een continu spectrum van levensduren.

*L.B. Liu, D. Gidley, and A.F. Yee, J. Polym. Sci., B30, 1992, 231.*

4. De bewering van Tanigawa *et al.* dat vacatures in niobium pas bij 620 K migreren, is onjuist.

*S. Tanigawa, I. Shinta, and H. Iriyama, in: Point Defects and Defect Interactions in Metals, eds. J.I. Takamura, M. Doyama, and M. Kiritani, North Holland, Amsterdam, 1982.*

5. De toenemende lexicale moeilijkheidsgraad van artikelen in populair-wetenschappelijke tijdschriften kan worden beschouwd als één van de oorzaken van de afnemende interesse voor fundamentele wetenschap bij het grote publiek.

*D.P. Hayes, Nature, 356, 1992, 739.*

6. In tegenstelling tot veel moderne bijbelvertalingen dient de Hebreeuwse *nif'al*-vorm נִפְּל in Psalm 76:2 niet passief ('is bekend') maar reflexief ('maakt zich bekend') te worden weergegeven.

*P. Joñon, Grammaire de l'Hébreu Biblique, Rome, 1965, §51c.*

7. De zin: "ἀφρέωνται αἱ ἁμαρτίαι αὐτῶν αἱ πολλαί, ὅτι ἠγάπησεν πολὺ" in Lukas 7:47 wordt slechts dan juist begrepen als ingezien wordt dat beide kernzinnen semantisch in een zogenaamde 'grounds-conclusion' relatie staan.

*K. Barnwell, Introduction to Semantics and Translation, Horsleys Green, 1984.*

8. De weergave van μονογενής in het bekende bijbelvers Johannes 3:16 als 'eniggeboren' (lat.: *unigenitus*) is onjuist. Op grond van zowel exegetische als linguïstische en historische argumenten verdient de vertaling 'enige' (lat.: *unicus*) de voorkeur.

*D. Moody, J. Biblical Literature, 72, 1953, 213.*

9. Aangezien niet-rokende echtgenoten van rokers een verdubbelde kans op het krijgen van longkanker hebben, verdient het aanbeveling de waarschuwing op de verpakking van rookwaren uit te breiden tot: "Roken kan longkanker veroorzaken – ook bij uw partner".

*C.G. Humble, J.M. Samet, and D.R. Pathak, Am. J. Public Health, 77, 1987, 598.*